

Northwestern University
Materials Science and Engineering
2145 Sheridan Rd., Technological Institute
Evanston, IL 60208, USA

Google Scholar: 2uSFOxgAAAAJ
ORCID: 0000-0002-6705-2329
Phone: (224) 382-3294 / 15711001611
Email: ziliang.wang@northwestern.edu

EDUCATION

Materials Science and Engineering, Northwestern University, Evanston, IL, USA

Aug. 2023 – Present

Postdoctoral Fellow in Materials Science | **PI:** Prof. Chris Wolverton

Major research: Data-Driven Search for Novel Li-Rich Layered Oxides (LRLO) Battery Chemistries; Machine Learning (ML)-Based Design and Discovery of Li-ion Battery Materials and Complex Nanoparticles

Materials Science and Engineering, National University of Singapore (NUS), Singapore

Aug. 2019 – Jul. 2023

Ph.D. in Materials Science and Engineering; CAP: 4.75/5.0

Major Project: Optimization and Discovery of Positive Electrode Materials Beyond Lithium-Ion Batteries with First-Principles Multiscale Techniques | **Supervisor:** Asst. Prof. Pieremanuele Canepa

School of Physics, University of Chinese Academy of Sciences (UCAS), Beijing, P. R. China

Sept. 2015 - Jul. 2019

Bachelor of Science in Physics; Overall GPA: 3.75/4.0; Major GPA: 3.8/4.0 (top 5% in the department)

Final Year Project: Mechanics of Growth of Two-Dimensional Au₂Se Atomic Crystal Thin Film Material | **Advisor:** Prof. Xiao Lin & Hongjun Gao

RESEARCH INTERESTS

- Design and simulation for energy storage, and applications, including electrode/electrolyte materials for Na/Li-ion batteries, all-solid-state batteries, thin film materials, nanoparticles, and semiconductors
- Combine high-throughput computations with techniques from statistical mechanics modelling & ML to facilitate investigations of novel energy materials
- Multiscale methods combining theoretical computations and experimental characterizations to understand fundamental physics of properties of materials

RESEARCH EXPERIENCES

Postdoc Fellow, Ford-Northwestern Alliance

Aug. 2023 – Present

PI: Prof. Chris Wolverton

- **Overview:** Combine high-throughput computations and ML models to design novel LRLO (i.e., Li- and Mn-rich (LMR) layered oxides) battery cathode, with improved electrochemical properties and industrial cost; significantly extend current materials database (e.g., to include materials interfacial properties) and develop ML tools for accelerating exploration of new materials.
- **Project 1:** Using multi-compositional substitution strategies to stabilize the structure of LMR (i.e., Li₂MnO₃) at high-voltage region with constrained cation migration and oxygen release, assisted by high-throughput computations || Understand phase behaviours of Li₂MnO₃-LiMO₂ compounds (M = Ni, Mn, Co)¹ || Construct ML-database for key properties of LRLO cathodes (e.g., LiMO₂-Li₂MO₃ composites) in large chemical space, with self-developed models & packages.



- **Project 2:** Data-driven design and discovery of complex nanoparticles with controlled interfacial properties.
- **Project 3:** Computationally-assisted investigations of novel perovskites.

Ph.D. Graduate Research Assistant, NUS**Aug. 2019 – Jul. 2023****Supervisor:** Asst. Prof. Pieremanuele Canepa

- **Overview:** Combined first-principles calculations with statistical mechanics analysis (i.e., cluster expansion, Monte Carlo simulation) and ML tools for multiscale discovery and optimization of electrode/electrolyte materials for Na-ion batteries.
- In cooperation with **TIAMAT Energy** / Laboratoire de Réactivité et de Chimie des Solides (**LRCS**) / Université de Picardie Jules Verne (**UPJV**) / CNRS-UMR / **RS2E** / University of California, San Barbara (**UCSB**) / Indian Institute of Science (**IISc**) / Bar Ilan University (**BIU**) / University of Houston (**UH**)
- **Project 1:** Investigated thermodynamic properties and Na (de)intercalation mechanisms of NaSICON electrodes through a 3d-transition metal based chemical space. (B. Singh, **Z. Wang** et al. *J. Mater. Chem. A*²)
- **Project 2:** Elucidated complex thermodynamics of Na intercalation into NaSICON-based $\text{Na}_x\text{V}_2(\text{PO}_4)_3$ cathode combining first-principles calculations, cluster expansion, and Monte Carlo simulations. Identified a new stable phase of $\text{Na}_2\text{V}_2(\text{PO}_4)_3$ using computations and experiments. (**Z. Wang**, S. Park et al. *J. Mater. Chem. A*³, *Chem. Mater.*⁴ & Patent WO-2023209113-A1)
- **Project 3:** Developed a novel chemical synthesis method to obtain various unconventional stable phases of $\text{Na}_x\text{V}_2(\text{PO}_4)_3$ (e.g., $\text{Na}_{1.75}\text{V}_2(\text{PO}_4)_3$, $\text{Na}_2\text{V}_2(\text{PO}_4)_3$, $\text{Na}_{2.25}\text{V}_2(\text{PO}_4)_3$) and reached $\text{V}_2(\text{PO}_4)_3$ by complete Na-extraction from single-phase $\text{Na}_x\text{V}_2(\text{PO}_4)_3$ cathode. Increased the theoretical energy density to 458 Wh/kg at an average voltage of 3.7 V vs. Na/Na^+ . (S. Park, **Z. Wang** et al. *Nature Materials*⁵)
- **Project 4:** Developed a python-based kinetic Monte Carlo simulation package to capture the effect of local configuration on Na-ion transport in NaSICON electrodes. (**Z. Wang** et al. *ACS Materials Lett.*⁶)
- **Project 5:** Optimized energy density of $\text{Na}_x\text{V}_2(\text{PO}_4)_2\text{F}_3$ electrode by unlocking its inaccessible capacities at high-voltage region through transition metal/anion mixing. (S. C. C. van der Lubbe, **Z. Wang** et al. *Chem. Mater.*⁷, S. Chakrabarty et al.)
- **Project 6:** Developing cluster expansion model for “liquid-like” lattices.

Undergraduate Thesis, UCAS**Nov. 2018 – May 2019****Advisor:** Prof. Xiao Lin & Hongjun Gao

- **Overview:** Utilized chemical vapor deposition for generating two-dimensional Au_2Se crystal thin film material. Unveiled mechanics of growth of the as-synthesized material and investigated its surface topology combining atomic force microscope, X-ray photoelectron spectroscopy and X-ray diffraction.

Undergraduate Research Assistant, UCLA**Jul. 2018 – Aug. 2018****Advisor:** Prof. Gerard C. L. Wong

- **Overview:** Experiments on high-speed “4D” computational microscopy of bacterial surface motility.

Undergraduate Research Assistant, Institute of Physics, CAS**Dec. 2017 – Apr. 2018****Advisor:** Prof. Xiao Lin, Hongliang Lu

- **Overview:** Mechanical exfoliation and surface morphology characterisation of 2D materials.

PUBLICATIONS

Published:

- 1. *Phase Stability of Li-Rich Layered Cathodes: Insight into the Debate over Solid Solutions vs Phase Separation.* Z. Lu, S. Hao, **Z. Wang**, H. Kim, C. Wolverton, *Chem. Mater.* **2024**, acs.chemmater.2c00927.
- 2. *A Chemical Map of NaSICON Electrode Materials for Sodium-Ion Batteries.* B. Singh¶, **Z. Wang¶**, S. Park, G. S. Gautam, J.-N. Chotard, L. Croguennec, D. Carlier, A. K. Cheetham, C. Masquelier, P. Canepa, *J. Mater. Chem. A - Themed Collections: HOT Papers; Energy Frontiers; Battery science and technology* **2021**, 9 (1), 281–292. ¶Equal Contribution
- 3. *Phase Stability and Sodium-Vacancy Orderings in a NaSICON Electrode.* **Z. Wang**, S. Park, Z. Deng, D. Carlier, J.-N. Chotard, L. Croguennec, G. S. Gautam, A. K. Cheetham, C. Masquelier, P. Canepa, *J. Mater. Chem. A - Themed Collection: HOT Papers* **2022**, 10 (1), 209–217.
- 4. *Crystal Structure of $Na_2V_2(PO_4)_3$, an Intriguing Phase Spotted in the $Na_3V_2(PO_4)_3-Na_1V_2(PO_4)_3$ System.* S. Park, **Z. Wang**, Z. Deng, I. Moog, P. Canepa, F. Fauth, D. Carlier, L. Croguennec, C. Masquelier, J.-N. Chotard, *Chem. Mater.* **2022**, 34 (1), 451–462.
- 5. *Obtaining $V_2(PO_4)_3$ by Sodium Extraction from Single-Phase $Na_xV_2(PO_4)_3$ ($1 < x < 3$) Positive Electrode Materials.* S. Park¶, **Z. Wang¶**, K. Choudhary, J.-N. Chotard, D. Carlier, F. Fauth, P. Canepa, L. Croguennec, C. Masquelier, *Nature Materials.* **2025**, 24(2), 234–242 ¶Equal Contribution & Featured in **Science** *More over lithium: Sodium batteries could one day power a green economy.*
- 6. *Kinetic Monte Carlo Simulations of Sodium Ion Transport in NaSICON Electrodes.* **Z. Wang**, T. P. Mishra, W. Xie, Z. Deng, G. S. Gautam, A. K. Cheetham, P. Canepa, *ACS Materials Lett.* **2023**, 5(9), 2499–2507
- 7. *Unlocking the Inaccessible Energy Density of Sodium Vanadium Fluorophosphate Electrode Materials by Transition Metal Mixing.* S. C. C. Van Der Lubbe¶, **Z. Wang¶**, D. K. J. Lee, P. Canepa, *Chem. Mater.* **2023**, 35 (13), 5116–5126. ¶Equal Contribution

In-Progress (Selected):

- *Effect of Nb Substitution on Thermodynamic and Kinetic Properties of $Na_xV_2(PO_4)_3$.* E. G. Correa, **Z. Wang**, F. Zhou, P. Canepa, R. Clément.
- *Impact of Br Substituted $Na_3V_2(PO_4)_2F_{(3-x)}Br_x$ Structure Towards Triggering of 3rd Na During Reversible Na (de)Intercalation for Na Ion Battery.* S. Chakrabarty, A. Mukherjee, **Z. Wang**, S. Taragin, R. Yemini, I. Perelshtain, P. Canepa, M. Noked.
- *Sodium-Vacancy and Vanadium-Manganese Orderings in Mn-Substituted $Na_xV_2(PO_4)_3$ NaSICON Cathode.* **Z. Wang**, M. Bhatt, P. Canepa.
- *Advanced CASM Package with Accuracy in "Liquid-Like" Crystal Lattices.* **Z. Wang**, P. Canepa.
- *A Physics-Informed Machine-Learning Approach for Screening Key Properties of Lithium-Rich Layered Oxides.* **Z. Wang**, C. Wolverton.
- *Optimization of Ion-Exchange Lithium-Rich and Mn-Rich Layered Oxides with Multi-Compositional Defects.* **Z. Wang**, Y. Han, C. Liu, C. Wolverton.
- *Insights into Phase Behaviors of Lithium and Sodium Interchanged Layered Oxides.* Y. Han, **Z. Wang**, W. Xie, C. Liu, C. Wolverton.
- *An Isomeric Homologous Series of Perovskite in Ba-Sb-Te-S Chemical Space.* H. Zhao, **Z. Wang**, S. Shahabfar, S. Hao, C. Wolverton, M. Kanatzidis.
- *Structural Stabilization of A Layered Manganese Oxide with Reversible Oxygen Redox at High Voltage.* Z. Liu, **Z. Wang**, C. Wolverton, Q. Liu, Y. Ren.
- *Correlating Migration of Alkali Metal Ions with Voltage Hysteresis in Layered Oxide Cathodes.* Z. Liu, **Z. Wang**, C. Wolverton, Q. Liu, Y. Ren.

PATENT

- *New Nasicon-Type High Voltage Sodium Vanadium Phosphates Materials For Na-Ion Batteries.* S. Park, J.-N. Chothard, L. Croguennec, D. Carlier-Larregaray, C. Masquelier, **Z. Wang** and P. Canepa, provisional patent WO2023209113A1 (EMO/FSY).

CONFERENCES

- 2021 The Electrochemical Society (ECS) Meeting Abstract. *Crystal Chemistry of $Na_xMM'(PO_4)_3$ Nasicon Electrodes ($M, M' = V, Fe, Mn, Ti, Cr$).*
- 2022 The 2nd International Conference on Materials for Humanity (MRS-MH 22) Poster Presenter. *Sodium-vacancy Orderings and Crystal Structures of $Na_xV_2(PO_4)_3$ NaSICON Electrodes.*
- 2023 The International Conference on Materials for Advanced Technologies (ICMAT) Meeting Abstract. *New Vanadium Phosphates as Positive Electrode Materials for Na-ion and K-ion Batteries.*
- 2024 International Meeting on Lithium Batteries (IMLB) Poster Presenter. *Investigation and Optimization of Li-Rich Layered Oxide Cathodes with High-Throughput Computations and Beyond.*
- 2024 The Solid State Chemistry Gordon Research Conference (GRC) Poster Presenter. *Linking Sodium Solubility to Ion Transport in Natrium Super Ionic CONductors.*
- 2025 The Electrochemical Society (ECS) Meeting Abstract. *Strategies to Increase Sodium Solubility in High-Energy Density Polyanion Electrode Materials.*

TEACHING EXPERIENCES

- **Teaching Assistant:** Module MLE 3101 @ NUS 2020 Semester #2 & 2021 Semester #2
Organized and mentored laboratory-based lectures. Assisted students with hands-on thin-film materials characterization using atomic force microscopy.
- **Research Assistant:** Canepa Research Group @ NUS 2019 - 2023
Assisted with research group activities, including periodical group meeting organizations, compute clusters management, junior students mentorship, and research outreach & collaboration arrangement.

HONORS & AWARDS

- Undergraduate Academic Scholarship | Oct. 2018
- Yuan Hong (Shan Dong) Technical Materials Ltd's Public Scholarship | Apr. 2018
- NUS Research Scholarship | Aug. 2019 – Jul. 2023
- Ford-Northwestern Alliance Postdoctoral Fellowship | Aug. 2023 – Present
- Northwestern the International Institute for Nanotechnology Future Faculty Program 2024 Participant
- Associate Member of the Royal Society of Chemistry | Jan. 2025
- Science News—More over lithium: Sodium batteries could one day power a green economy | 20 Feb. 2025

SKILLS

- **Experimental skills:** Thermal evaporation / Mechanical exfoliation / Atomic Force Microscopy (AFM) / X-ray Diffraction (XRD) / X-ray photoelectron spectroscopy (XPS) / Nuclear magnetic resonance (NMR)
- **Programming skills:** Windows/Linux system, C, C++, Python, ML, Shell
- **Softwares:** Microsoft Office, VASP, CASM, Lobster, ATAT, QuantumEspresso, CASTEP, VESTA



Research Proposal of Ziliang Wang

In the critical area of clean energy technologies, energy storage and conversion materials have attracted considerable attention due to their potential energy density, safety and sustainability. Various energy-storage devices have been invented, ranging from portable electronics (e.g., laptops) to industrial-grade products (e.g., electrical vehicles). Therefore, developing efficient methods to discover and optimize energy materials and interpret physical origins of their novel properties become the key factor in related research field.

Modern computational technique is an important way to understand structure-property relations of energy materials and provide crucial insights into their performance. Building on advanced computing resources, multiscale computational methods—such as combining high-throughput (HT) density functional theory (DFT) with physics-informed machine-learning (ML) techniques—have been well developed and applied to accelerate design of novel energy materials.

My research aims to advance the development of rechargeable alkali-ion batteries and expand the limits of computational theories by developing physics-informed ML techniques. I study the practical performance of battery materials stemming from fundamental thermodynamics, kinetics, electronic structures and phase behaviors, to address the bottlenecks of promising electrodes/electrolytes, such as Sodium (Na) Super Ionic CONductors (NaSICON),^{1–4} Li-Rich Layered Oxides (LRLO).⁵ I also work on using materials informatics to learn patterns from datasets of energy materials and accelerate interpretation of related data and prediction of novel complex materials.⁶

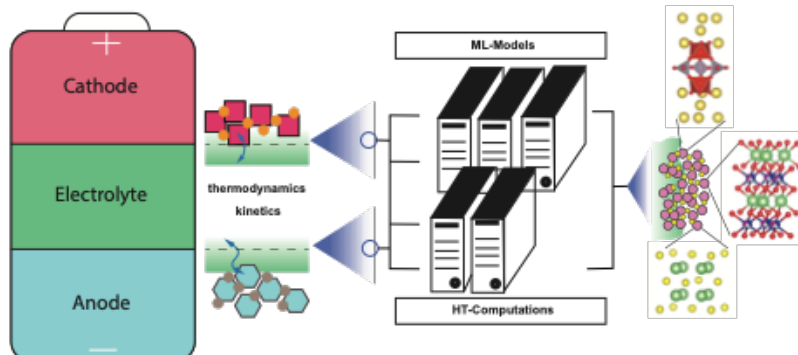


Figure 1. Rational design of energy materials (e.g., battery materials) by data-driven techniques.

The first scope of my research is data-driven search for novel rechargeable alkali-ion batteries for energy storage technology. A large amount of alkali-ion based electrodes and electrolytes have been studied during the past several decades. Basically, cathode materials factor prominently in the overall energy densities stored by batteries, and intercalation compounds are a typical framework of cathodes. Through data-driven approaches, researchers can screen diverse chemistry space and structural prototypes of cathodes, to evaluate multiple properties based on thermodynamic and kinetic theories (Figure 1). However, several crucial problems are in need of further considerations to advance current research of battery cathode materials, such as alkali-ion (de)intercalation mechanisms, phase behaviors and stabilities, as well as practical optimizations for higher energy densities.

Within the energy storage scope of my research, the first focus is combining HT-DFT and ML for accelerated interpretation and design of Li-ion batteries (LIBs), especially for promising electrodes of LIBs.

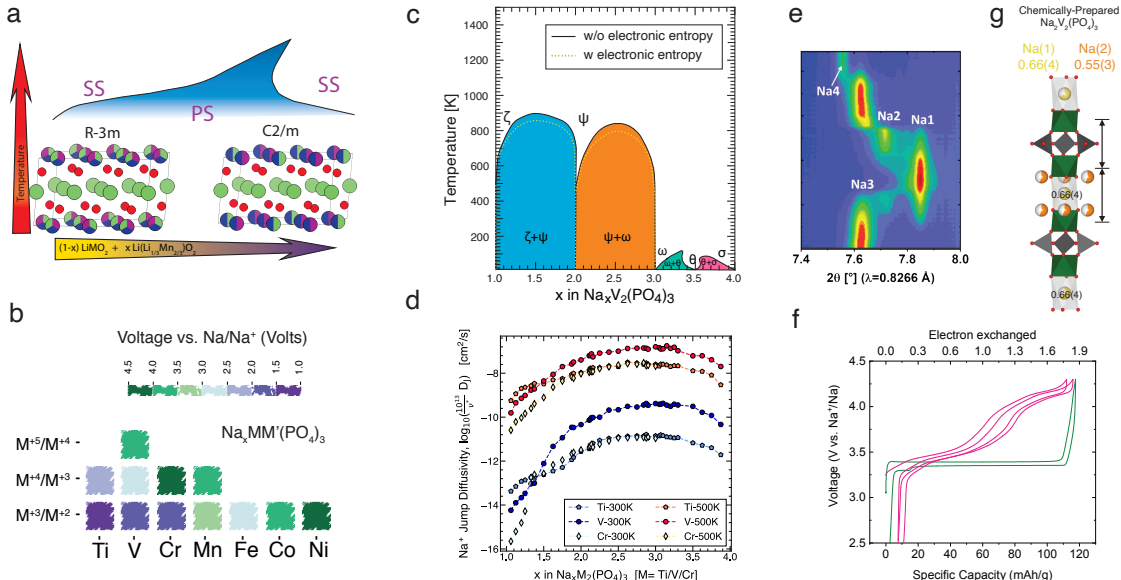


Figure 2. Rechargeable alkali-ion batteries. (a) Phase behaviors of LRLO. (b) Charted chemical space of $\text{Na}_x\text{MM}'(\text{PO}_4)_3$. (c) Computational phase diagram of $\text{Na}_x\text{V}_2(\text{PO}_4)_3$. (d) Kinetic monte carlo simulations of Na^+ diffusivities of NaSICON. (e) Operando X-ray diffraction patterns of $\text{Na}_x\text{V}_2(\text{PO}_4)_3$. (f) Electrochemical cycling profiles of chemically prepared $\text{Na}_2\text{V}_2(\text{PO}_4)_3$. (g) Schematic representations of local structure in $\text{Na}_2\text{V}_2(\text{PO}_4)_3$.

For one of the most applied cathodes of LIBs, namely LRLO (i.e., $\text{Li}_{1+x}\text{M}_{1-x}\text{O}_2$ or $\text{mLi}_2\text{MnO}_3-\text{nLiMO}_2$), we performed HT computations for Ni, Co, and Mn based LRLO in 2 prototypes (i.e., $C2/m$ and $R-3m$ in Figure 2a).⁵ We analyzed phase diagram of LiMO_2 - Li_2MnO_3 pseudo-binary chemical space and identified that phase separation is more thermodynamically favorable than solid solution at low temperature.

I am also working on LRLO with O2 stacking sequence (i.e., in $Cmc2_1$ symmetry) with a capped-honeycomb (CH) structure, which will preserve high-voltage stability.⁷ I have evaluated the defect formation energies of 7 selected transition metals (TM) at Li site and clarified Ti as the most favorable TM within CH-LRLO. Additionally, dilute fluorine (F) dopant at oxygen sites will also improve the cathode performance.^{8,9} Therefore, my short-term goal is to optimize O2-CH-LRLO with capped-Ti_{Li}, Mn/TM mixings as well as O/F mixing for higher energy densities and better cyclability by HT computations. In the interim, I will cooperate with experimental techniques to figure out practical synthesize routes for multi-compositional substituted O2-LRLO. In the long term, I propose to develop ML models (e.g., using ML interatomic potentials, and/or graph-based algorithms) which can incorporate my HT-results of Li-ion cathodes to predict key properties (e.g., synthesizability, defect formation and cation migration energies).

My second focus for battery is post-LIBs, especially Na-ion batteries (NIBs) which are potential for improved energy densities and cost beyond the metrics of commercial LIBs.

We studied polyanionic cathode of NIB in NaSICON framework (i.e., $\text{Na}_x\text{MM}'(\text{PO}_4)_3$) in a wide range of chemical space. We have charted 28 distinct 3d TM-based NaSICONs (Figure 2b) and derived their intercalation thermodynamics, of which only 13 have been experimentally discovered before.¹ These findings provide a complete chemical map of NaSICON cathodes. Moreover, we elucidated —for the first time— Na intercalation mechanisms of $\text{Na}_x\text{V}_2(\text{PO}_4)_3$ (N_xVP) compound with the computational phase diagram of NaSICON cathode (Figure 2c), by a basic ML algorithm using cluster expansion formalism mapped on compositional configurations.² We identified a previously uncharted stable phase of N_2VP and confirmed its existence by *operando* synchrotron measurements (Figure 2e).³ These findings are beneficial for a high-rate performance of N_xVP cathode.

Remarkably, we obtained N_xVP phase by chemical synthesis and improved energy density of N_xVP by 15.5% (Figures 2f and 2g). ⁴ I also developed a kinetic Monte Carlo (kMC) simulation package ⁶ to reveal critical kinetic properties for NaSICON cathodes (Figure 2d).

Based on these efforts and experience, I propose to search for novel monovalent (Na) and multivalent ion (Mg, Ca, and Zn) post-LIBs with data-driven approaches. The essential objective in this regard is HT-screening of representative properties of electrodes (e.g., phase behaviors at various temperatures, redox mechanism, cation diffusivities), and then construct a materials-informatics database for post-LIB cathode materials. I will also extend my database beyond bulk materials to including interfacial properties as well.

My third focus on battery technologies is design of all-solid-state batteries (ASSBs) which will surpass conventional liquid-electrolyte-contained batteries with increased safety and energy densities. ¹⁰ My short-term goal is to focus on discovery and optimization of cathodes that can be applied in ASSBs (e.g., Li-S composite) and searching for compatible solid-state electrolyte candidates with high ionic conductivities. Identifying active ion positions within solid-state electrolyte will also be my focus. In the long term, I will combine DFT and molecular dynamics simulations to provide insights into structural and ion-transport properties of electrode-electrolyte-interface (EEI).

As a future plan for my energy storage scope of research, I propose to construct a ML framework for battery materials with the computational phase diagram, kMC modeling, and materials-informatics database I developed as mentioned above. Such ML framework can accelerate interpretation of battery thermodynamics (e.g., phase behaviors, intercalation energies, interatomic potentials), kinetics (e.g., diffusivities) and interfacial properties (e.g., surface energies and dynamics in EEI), as well as predictions of new promising candidates to LIBs and NIBs (e.g., oxides, sulfides, polyanionic compounds and high-entropy frameworks). To this end, I will start from deriving phase diagrams of main class of cathodes for LIBs and NIBs, and to evaluate their macroscopic diffusion as well as the interatomic potential energies. These efforts will deepen our understandings of battery performance and provide specific physics foundation for my ML-framework. Hierarchically, an automatic physics-informed ML architecture will be constructed which can interactively combine computational outputs with experimental characterizations of energy storage materials.

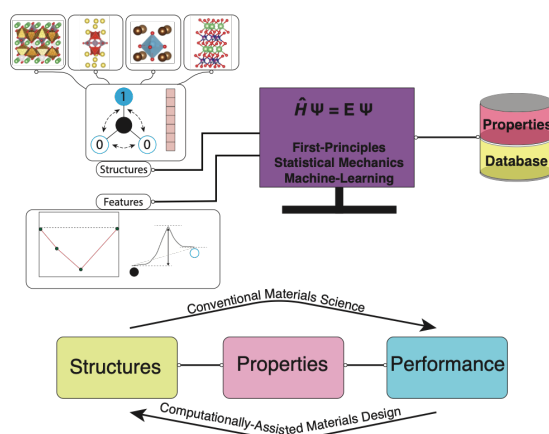


Figure 3. ML development for accelerating materials science research.

The second scope of my research is general data-driven ML development for advanced computational materials science (Figure 3).

We have shown that combining HT-computations and cluster expansion methods – a basic ML framework to predict properties and previously-uncharted compounds without *ab initio* computations or specially-designed experimental routes – the comprehensive phase diagrams and diffusion dynamics across the composition-temperature region can be derived with high accuracy (Figures 1, 2c and 2d).^{2,6} Based on graph networks, several materials informatics packages for ML interatomic potentials have been developed to evaluate novel materials with superior properties.^{11–13} Similar to phase behavior of NaSICON which is affected by several phenomena such as Na-vacancy and charge orderings, ML models for targeted materials properties should be specifically and rigidly related to physics information, rather than universal. I am now working on featurization of a ML model to predict TM migration tendencies in LRLO (i.e., Ni-Mn-Co-based), which requires considering the influence of both full compositional space and local environment on migrating TM ions. Given my focus on ML development, I propose to construct reliable physics-informed ML frameworks that can combine to solve problems for a wide range of complex materials.

My short-term goal is to develop “properties-targeted” ML that aims for interpretation of crystallography and prediction of key properties for materials (with known structures) at large spatial and time scale.

My long-term goal in the regard of ML development is to search for a novel materials design algorithm, i.e., “structure-targeted” ML. Such a ML workflow can learn from current HT studies on basic structural units (e.g., atoms, bonds and polyhedral units), interatomic interactions and the effect of “perturbations” of atomic positions on potential energy/charge density surface, to design new crystal structures with desired elements. Properties of as-generated structures can be interactively evaluated by the “properties-targeted” ML as mentioned above. Notably, these efforts will “close the loop” of materials design logic by a backward process, i.e., properties to structures engineering (Figure 3).

To fulfill my requirements of data-driven investigations, I have sufficient experience in applying for supercomputing resources. For example, Sugon High Performance Computing resources, and buy-in dedicated clusters will be potential candidates to comply with my demands for computing power. Moreover, I have cooperation and relationships with several Hong Kong local capital and technical companies which can be potential funding resources to support my research.

With my experience and proposed focuses in the two major scopes (i.e., rechargeable batteries of energy storage and ML development), I would like to contribute actively to advance the current materials science research in related fields and accelerate all potential applications of sustainable energy storage technologies to fulfil requirements of the society for developing next-generation clean energy economy.

References [(co)first author]

- [1] B. Singh[#], Z. Wang[#], et al., *J. Mater. Chem. A*, 2021, 9, 281–292.
- [2] Z. Wang[#], et al., *J. Mater. Chem. A*, 2022, 10, 209–217.
- [3] S. Park, Z. Wang, et al., *Chem. Mater.*, 2022, 34, 451–462.
- [4] S. Park[#], Z. Wang[#], et al., *Nature Materials*, 2025, 24, 234–242.
- [5] Z. Lu, S. Hao, Z. Wang, et al., *Chem. Mater.*, 2024, 36, 6381–6391.
- [6] Z. Wang[#], et al., *ACS Materials Lett.*, 2023, 5, 2499–2507.
- [7] *Nat. Energy*, 2023, 8, 1078–1087.
- [8] *Adv. Energy Mater.*, 2020, 10, 2001671.
- [9] *RSC Adv.*, 2015, 5, 107326–107332.
- [10] *Nat. Mater.*, 2019, 18, 1278–1291.
- [11] *Nat. Mach. Intell.*, 2023, 5, 1031–1041.
- [12] *Chem. Mater.*, 2019, 31, 3564–3572.
- [13] *Nat. Commun.*, 2022, 13, 2453.

Teaching Statement of Ziliang Wang

In the pivotal domain of developing next generation clean energy technologies, knowledge of current energy storage and conversion in devices as well as the outlook for advanced solutions and approaches are required for researchers and educators. A successful professor should be experienced in both roles as mentioned. As an independent researcher, a professor should propose applicable projects to inform the essential scientific problems that could address challenging bottlenecks. More importantly, as a dedicated educator, a professor should also be capable of cultivating students as critical thinkers, providing them with a solid technical foundation and encouraging their creative and pioneering insights into the discipline instead of memorizing and repeating the conventional methods. These facets summarize my goal in teaching, and I expect my students to be deep thinkers who both have profound understandings of the basic science and have abilities to tackle problems with the knowledge they have mastered.

My teaching philosophy and skills have been developed through teaching, mentoring students, learning from excellent educators in multiple institutes of the University of Chinese Academy of Sciences (UCAS), and more recently, supporting as teaching assistant (TA) and research assistant (RA) at the National University of Singapore (NUS) and Northwestern University (NU).

—Teaching Approach

While studying physics at UCAS, I had the opportunities to take modules given by several renowned educators, for example, from the institute of physics, high energy physics, mathematics, and computing technology. Besides cultivated by their solid and critical knowledge, I also learned from their approaches to developing students' foundations from basic concepts to technical applications. First of all, I should put students and their learning process at the center. Teaching should not be expected to be a simple one-way information communication from the educators, instead, I should act more as a director who give fundamental concepts and theories to students and get their feedbacks while they get familiar with new knowledge. Answering students' questions and modulating my teaching process accordingly are necessary to make sure all students are in proper process to acquire the information. Secondly, "representative instruction" is also important considering the long-term development nature of teaching. I realize that there are numerous applications to a specific concept, and instead of reviewing them thoroughly, I should try to focus on several representative problems and help students to build up a practical framework in applying the concepts. These efforts will get students well instructed for solving a series of problems themselves.

In addition to the teaching skills mentioned above, I also strive to teach with active in-/out-of-class activities based on my TA experience at NUS. I supported as TA for module MLE 3101 for 2 semesters in 2020 and 2021. This is a materials characterization class at NUS that requires students to acquire basic lab-based skills (e.g., atomic force microscopy). The challenge for such module is that students spend more time learning from tutorials than doing hands-on experiments in class, which degrades the benefits of a long-term development for the students. Therefore, I worked with other TAs to split the groups, so that participated students can spend adequate time before each class reviewing tutorials and bringing their questions to class while clarifying during instructed characterizations by groups. Meanwhile, I reached out to solve students' puzzles while they were waiting for their turn to use AFM, and I created communication channels after class for continuing discussion on theoretical and experimental aspects. These in-class and out-of-class activities have provided invaluable improvement to the modules and will be beneficial for my teaching.

Furthermore, I would like to create a supportive and kind environment while teaching. All questions are welcome, and I want my students from diverse background to feel a

welcoming environment to question, or raise a disagreement, which will be constructive to both my teaching and my students' long-term development.

—Teaching Interests

My research scope covers a wide range of disciplines, including computational theory, machine-learning, physics and chemistry properties of materials, thermodynamics and kinetics of materials, and chemical engineering. Given the need, I am eager to teach courses at both undergraduate and graduate level. I am specifically excited to teach atomistic modelling of molecules and materials, thermodynamics and kinetics for rechargeable batteries, and advanced computational methods for materials informatics.

—Mentoring

I have mentored several undergraduate and graduate students as RA at NUS. Damien K. J. Lee, who is now a Ph.D. student at EPFL, was an undergraduate student at NUS. I helped him to get familiar with one of the cathode materials for sodium-ion batteries, which is sodium vanadium fluorophosphate (NVPF). I also assisted him in using basic computational tools to investigate the chemical space of NVPF. Through my instructions, we reported a promising candidate to NVPF by transition metal substitution, which achieved an increase in energy density of NVPF by ~13.9% (*Chem. Mater.* 2023, 35 (13), 5116–5126, DOI: [10.1021/acs.chemmater.3c00745](https://doi.org/10.1021/acs.chemmater.3c00745)). Another graduate student that I feel proud of is Weihang Xie, who is now completing his Ph.D. at NUS. Through my mentoring, Weihang got a good command of local cluster expansion and kinetic Monte Carlo (kMC) simulations. We successfully developed a kMC package that can be applied to various NaSICON cathode for quick evaluations of Na-ion migration kinetics (*ACS Materials Lett.* 2023, 5 (9), 2499–2507, DOI: [10.1021/acsmaterialslett.3c00610](https://doi.org/10.1021/acsmaterialslett.3c00610)). More recently, I continue with the RA support at NU on multiple occasions. All these mentoring experiences will confirm my qualification as a professor to supervise students and collaborate with multinational research teams.

—Perspective

In summary, I am excited about the opportunity to teach, and I regard teaching as an important part of my career plan as a professor. Teaching the next generations, and get them well educated are crucial in cultivating superior researchers and creators for the development of the whole society.

Obtaining $V_2(PO_4)_3$ by sodium extraction from single-phase $Na_xV_2(PO_4)_3$ ($1 < x < 3$) positive electrode materials

Received: 23 July 2023

Accepted: 12 September 2024

Published online: 23 October 2024

Sunkyu Park^{1,2,3,11}, Ziliang Wang^{4,5,11}, Kriti Choudhary¹, Jean-Noël Chotard^{1,6}, Dany Carlier^{1,2,6}, François Fauth^{1,7}, Pieremanuele Canepa^{1,4,8,9}✉, Laurence Croguennec^{1,2,6}✉ & Christian Masquelier^{1,6,10}✉

 Check for updates

We report on single-phase $Na_xV_2(PO_4)_3$ compositions ($1.5 \leq x \leq 2.5$) of the Na super ionic conductor type, obtained from a straightforward synthesis route. Typically, chemically prepared c- $Na_2V_2(PO_4)_3$, obtained by annealing an equimolar mixture of $Na_3V_2(PO_4)_3$ and $NaV_2(PO_4)_3$, exhibits a specific sodium-ion distribution (occupancy of the Na(1) site of only 0.66(4)), whereas that of the electrochemically obtained e- $Na_2V_2(PO_4)_3$ (from $Na_3V_2(PO_4)_3$) is close to 1. Unlike conventional $Na_3V_2(PO_4)_3$, when used as positive electrode materials in Na-ion batteries, the $Na_xV_2(PO_4)_3$ compositions lead to unusual single-phase Na^+ extraction/insertion mechanisms with continuous voltage changes upon Na^+ extraction/insertion. We demonstrate that the average equilibrium operating voltage observed upon Na^+ deintercalation from single-phase $Na_2V_2(PO_4)_3$ is increased up to an average value of ~3.70 V versus Na^+/Na (thanks to the activation of the V^{4+}/V^{5+} redox couple) compared to 3.37 V versus Na^+/Na in conventional $Na_3V_2(PO_4)_3$, thus leading to an increase in the theoretical energy density from 396.3 Wh kg⁻¹ to 458.1 Wh kg⁻¹. Electrochemical and chemical Na^+ deintercalation from c- $Na_2V_2(PO_4)_3$ enables complete Na-ion extraction, increasing energy density.

Lithium-ion batteries are widely used for electric vehicles and portable devices as they provide substantial energy and power densities, but lithium (Li) resources are critical and unevenly distributed worldwide, making it challenging to meet the urgent demand for large-scale energy storage systems^{1,2}. Sodium-ion batteries have received much recent attention due to the more abundant and evenly distributed resources of sodium (Na)^{3,4}. Sodium-containing transition metal layered oxides, Prussian blue analogues and polyanionic compounds are the main categories of positive electrode materials for Na batteries^{5–8}. Phosphates having the Na super ionic conductor (NASICON) structure are potential options as positive electrode materials because of their structural stability, rate performance and long cycle life^{5,9,10}. Among

them, $Na_3V_2(PO_4)_3$ has been extensively studied, delivering a theoretical capacity of 117.6 mAh g⁻¹ using the $V^{4+/3+}$ redox couple (3.37 V versus Na^+/Na), providing a theoretical energy density of ~396 Wh kg⁻¹ (refs. 11–13). As a positive electrode material, two Na^+ ions can be reversibly exchanged through a biphasic mechanism between $Na_3V_2(PO_4)_3$ and $Na_1V_2(PO_4)_3$. However, the third Na^+ cannot be extracted because of the large migration energy of Na^+ from the Na(1) site and high redox potential^{12,14}, which contributes to a weight penalty in addition to moderate operating voltage.

Through simulated phase diagrams from density functional theory (DFT), cluster expansion and Monte Carlo calculations, as well as operando synchrotron X-ray diffraction (SXRD) during Na^+

A full list of affiliations appears at the end of the paper. ✉e-mail: pcanepa@central.uh.edu; laurence.croguennec@icmcb.cnrs.fr; Christian.masquelier@u-picardie.fr

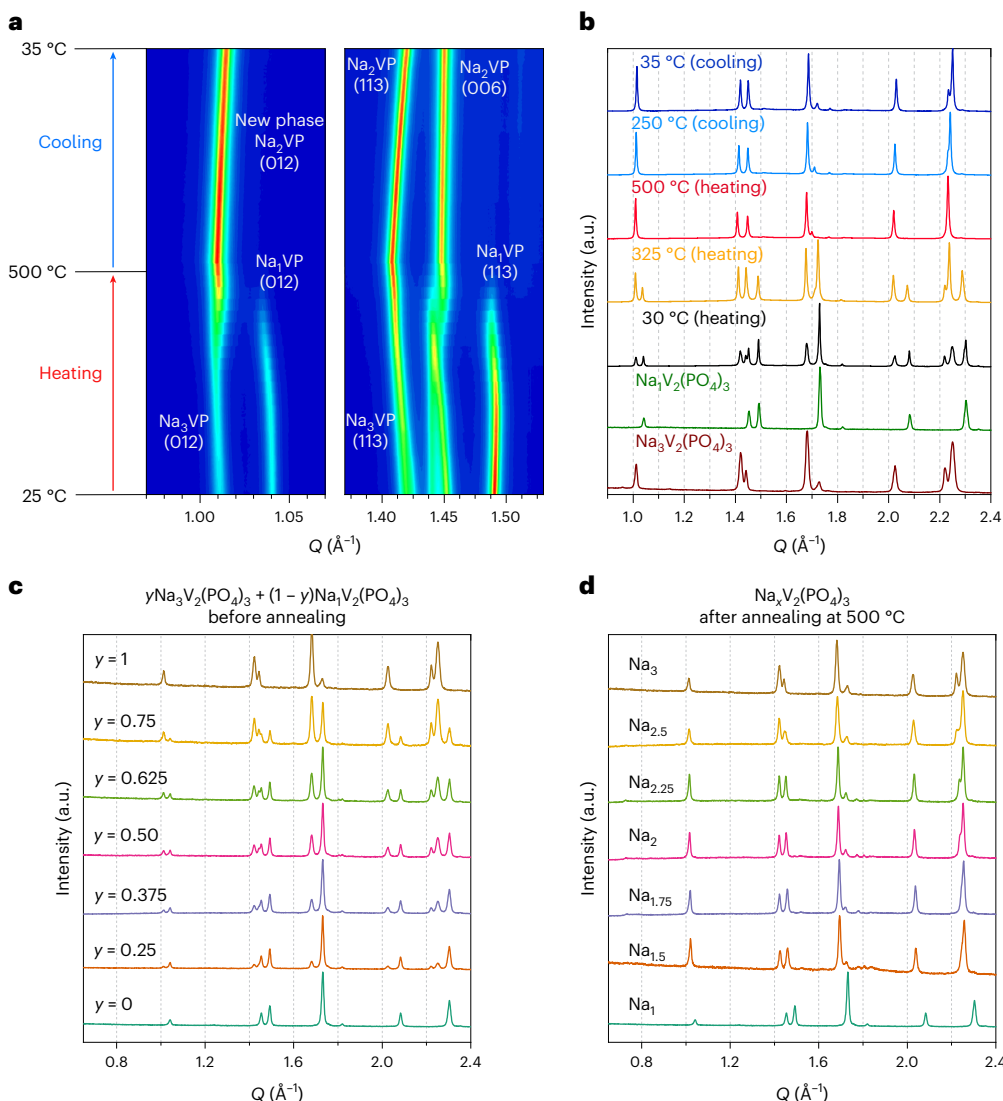


Fig. 1 | Synthesis of c- $\text{Na}_2\text{V}_2(\text{PO}_4)_3$. **a**, In situ temperature-controlled SXRD patterns for a 1:1 $\text{Na}_3\text{V}_2(\text{PO}_4)_3/\text{Na}_1\text{V}_2(\text{PO}_4)_3$ mixture, recorded every 3°C upon heating up to 500°C and then cooling to 35°C . **b**, Comparison of key XRD patterns with those of pristine $\text{Na}_3\text{V}_2(\text{PO}_4)_3$ and $\text{Na}_1\text{V}_2(\text{PO}_4)_3$. **c**, XRD patterns of mixtures of $\text{Na}_3\text{V}_2(\text{PO}_4)_3$ and $\text{Na}_1\text{V}_2(\text{PO}_4)_3$ with different molar ratios before

annealing, collected at 25°C . **d**, XRD patterns of $\text{Na}_x\text{V}_2(\text{PO}_4)_3$ single phases after annealing, collected at 25°C ($x = 2y + 1$). Note that $\text{Na}_x\text{V}_2(\text{PO}_4)_3$ is abbreviated as Na_xVP hereinafter. The complete series of XRD patterns collected with varying temperatures for different values of x are gathered in Supplementary Fig. 1a–e.

extraction/insertion, we have recently identified the existence of an intermediate $\text{Na}_2\text{V}_2(\text{PO}_4)_3$ phase between $\text{Na}_3\text{V}_2(\text{PO}_4)_3$ and $\text{Na}_1\text{V}_2(\text{PO}_4)_3$ (refs. 15,16). We determined the crystal structure of the electrochemically obtained e- $\text{Na}_2\text{V}_2(\text{PO}_4)_3$ and undertook substantial efforts to isolate this composition through various synthesis techniques. In this study we succeeded in chemically obtaining a new c- $\text{Na}_2\text{V}_2(\text{PO}_4)_3$ material that shows unusual and promising properties.

Spotting e- $\text{Na}_2\text{V}_2(\text{PO}_4)_3$ through electrochemistry

Extended Data Fig. 1 shows the SXRD patterns collected using a conventional $\text{Na}_3\text{V}_2(\text{PO}_4)_3$ -containing electrode in an in situ half cell operating between 2.0 and 4.3 V versus Na metal at several charge–discharge rates. As observed in recent studies^{15,17}, an intermediate $\text{Na}_2\text{V}_2(\text{PO}_4)_3$ phase appears upon battery operation in between the phases of compositions $\text{Na}_3\text{V}_2(\text{PO}_4)_3$ and $\text{Na}_1\text{V}_2(\text{PO}_4)_3$. The intermediate, electrochemically obtained phase, (hereafter e- $\text{Na}_2\text{V}_2(\text{PO}_4)_3$) appears more visible at high cycling rates, with an intermediate unit-cell volume that allows mitigating volume changes, strains and a more pronounced phase separation¹⁵, as identified in the LiFePO₄/FePO₄ system by the seminal work of Oriksa et al.¹⁸.

Formation of c- $\text{Na}_x\text{V}_2(\text{PO}_4)_3$: temperature-controlled X-ray diffraction

As we discovered the existence of the e- $\text{Na}_2\text{V}_2(\text{PO}_4)_3$ phase during preliminary operando XRD measurements¹⁵, we then naturally attempted to obtain the chemically prepared $\text{Na}_2\text{V}_2(\text{PO}_4)_3$ (hereafter c- $\text{Na}_2\text{V}_2(\text{PO}_4)_3$) through various synthesis procedures. We could apply a straightforward synthesis route to prepare single-phase c- $\text{Na}_x\text{V}_2(\text{PO}_4)_3$ compositions ($1.5 \leq x \leq 2.5$) by mixing the two end members $\text{Na}_3\text{V}_2(\text{PO}_4)_3$ and $\text{Na}_1\text{V}_2(\text{PO}_4)_3$ in appropriate ratios and annealing at moderate temperatures (500–550 °C). The pristine powders of both $\text{Na}_3\text{V}_2(\text{PO}_4)_3$ and $\text{Na}_1\text{V}_2(\text{PO}_4)_3$ were of high purity, and their unit-cell parameters were in excellent agreement with previously reported data^{15,19}. Here we chose to use the hexagonal unit cell (space group R-3c) to describe the monoclinic structure of $\text{Na}_3\text{V}_2(\text{PO}_4)_3$ (refs. 15,19), for comparison purposes: lattice parameters $a = 8.7179(2)$ Å, $c = 21.8292(14)$ Å and $V/Z = 239.90(2)$ Å³ where V/Z is the unit-cell volume per formula unit. $\text{Na}_2\text{V}_2(\text{PO}_4)_3$ was obtained as a single phase from $\text{Na}_3\text{V}_2(\text{PO}_4)_3$ by chemical oxidation, with the following lattice parameters: $a = 8.4276(2)$ Å, $c = 21.4731(4)$ Å and

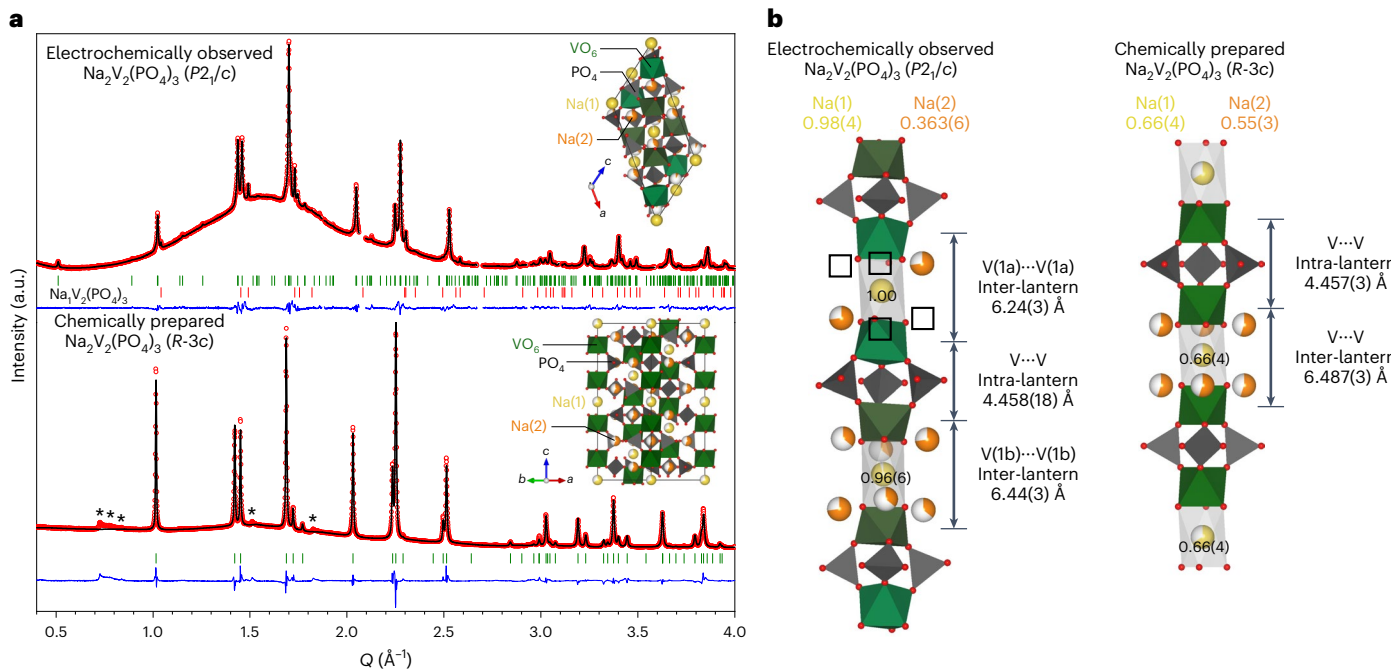


Fig. 2 | Structural variations in c- $\text{Na}_2\text{V}_2(\text{PO}_4)_3$ and e- $\text{Na}_2\text{V}_2(\text{PO}_4)_3$. **a**, SXRD patterns of $\text{Na}_2\text{V}_2(\text{PO}_4)_3$ at 25 °C. The top was collected with an in situ cell during electrochemical operation of a battery using a $\text{Na}_2\text{V}_2(\text{PO}_4)_3$ electrode as pristine material¹⁵. The bottom was chemically prepared c- $\text{Na}_2\text{V}_2(\text{PO}_4)_3$, collected within a capillary. The removed 2θ regions in the upper panel are ascribed to Al foil and Na metal. The asterisks in the bottom panel indicate reflection peaks that could not be indexed using the R-3c space group (details in the main text). The insets show the zoom out of $\text{Na}_2\text{V}_2(\text{PO}_4)_3$ crystal structures. In the SXRD patterns, red data points are observed data, black lines indicate the calculated XRD pattern, green and red vertical ticks indicate Bragg positions and blue lines are the difference between observed and calculated XRD patterns. **b**, Schematic representations of the $\text{V}_2(\text{PO}_4)_3$ lantern units with adjacent Na^{+} ions in the crystal

structures of electrochemically observed e- $\text{Na}_2\text{V}_2(\text{PO}_4)_3$ (left) and chemically prepared c- $\text{Na}_2\text{V}_2(\text{PO}_4)_3$ (right). We found two Wyckoff positions for vanadium in e- $\text{Na}_2\text{V}_2(\text{PO}_4)_3$ (e- Na_2VP), which are V(1a) and V(1b). Triple-dots correspond to the distance between V and V. Two V-V distances are represented: the distance between two vanadium sites belonging to the same lantern unit (intra-lantern) and the distance between two adjacent lantern units along the [001]_{hex} direction (inter-lantern) of the hexagonal representation of the unit cell. Note that the e- Na_2VP displays two possible symmetries (space groups P2₁/c or P2/c; ref. 15). We have demonstrated that P2₁/c is a more suitable symmetry for the description of e- Na_2VP , which exhibits similar Na-vacancy populations with the theoretically predicted, ordered Na_2VP , considering that the temperature and the synthesis conditions can impact the e- Na_2VP structure at room temperature.

$V/Z = 220.129(5)$ Å³. This corresponds to a relative unit-cell volume reduction $\Delta V/V = -8.3\%$ associated with the extraction of two Na^{+} ions (and hence the oxidation of V^{3+} to V^{4+}) from $\text{Na}_3\text{V}_{2+2}(\text{PO}_4)_3$, leading to $\text{Na}_1\text{V}_{4+2}(\text{PO}_4)_3$.

Figure 1a,b illustrates the temperature-dependent transformation of a 1:1 $\text{Na}_3\text{V}_2(\text{PO}_4)_3/\text{Na}_1\text{V}_2(\text{PO}_4)_3$ mixture monitored by in situ SXRD. This leads to the formation of a single phase of composition $\text{Na}_2\text{V}_2(\text{PO}_4)_3$ at 500 °C, maintained as a single phase upon cooling to room temperature. During heating, the SXRD reflection peaks of the two pristine phases shift to lower 2θ angles due to thermal expansion (2θ, the angle between the incident beam and reflected beam). As the temperature was increased above ~300 °C, the two phases started merging concomitantly into c- $\text{Na}_2\text{V}_2(\text{PO}_4)_3$, and the reaction was fully completed at ~500 °C. During cooling, the SXRD reflection peaks of the c- $\text{Na}_2\text{V}_2(\text{PO}_4)_3$ single phase did not change, without phase separation down to 35 °C, with a slight continuous peak shift towards higher angles due to thermal contraction.

Noticeably, using the procedure described above (mixing and then annealing $y\text{Na}_3\text{V}_2(\text{PO}_4)_3 + (1-y)\text{Na}_1\text{V}_2(\text{PO}_4)_3$ powders at 500 °C), various target c- $\text{Na}_x\text{V}_2(\text{PO}_4)_3$ compositions ($x = 1.5, 1.75, 2, 2.25, 2.5$) were prepared. The corresponding SXRD patterns recorded at 25 °C (before and after annealing) are gathered in Fig. 1c,d. Before annealing, the pristine mixtures containing the two phases $\text{Na}_3\text{V}_2(\text{PO}_4)_3$ and $\text{Na}_1\text{V}_2(\text{PO}_4)_3$ can be clearly distinguished, with SXRD peak intensities being directly associated with the molar ratio of each phase (Fig. 1c). After annealing up to 500 °C, the two pristine mixtures of phases transformed into single phases of c- $\text{Na}_x\text{V}_2(\text{PO}_4)_3$ compositions (Fig. 1d). In c- $\text{Na}_x\text{V}_2(\text{PO}_4)_3$, all the main diffraction peaks can be indexed with the

hexagonal cell and space group R-3c, with the peaks shifting towards lower 2θ angles for increasing values of x .

As determined by the Le Bail method and shown in Extended Data Fig. 2, the volume of the unit cell per formula unit (V/Z) decreases gradually when the Na content x varies from 2.5 to 1.5 in c- $\text{Na}_x\text{V}_2(\text{PO}_4)_3$, while the c/a ratio increases. Notably, the V/Z of the intermediate c- $\text{Na}_x\text{V}_2(\text{PO}_4)_3$ phases are found to be larger than those expected from the direct interpolation between the two end members, $\text{Na}_3\text{V}_2(\text{PO}_4)_3$ and $\text{Na}_1\text{V}_2(\text{PO}_4)_3$, probably nested in the partial occupancy of the Na(1) site in the chemically prepared c- $\text{Na}_x\text{V}_2(\text{PO}_4)_3$, while Na(1) is fully occupied in pristine $\text{Na}_3\text{V}_2(\text{PO}_4)_3$ and $\text{Na}_1\text{V}_2(\text{PO}_4)_3$. We report a single-phase composition with continuous unit-cell volume variation as a function of Na^{+} content in $\text{Na}_x\text{V}_2(\text{PO}_4)_3$. Similarly, intermediate Li_xFePO_4 phases ($0 < x < 1$) discovered in 2005 by Delacourt et al.²⁰ were reported to form above 300 °C, prone to phase separation when cooled to room temperature (due to a eutectic point of $\text{Li}_{0.6}\text{FePO}_4$ encountered upon quenching)^{20–25}. Likewise, similar foundational work on the $\text{NaTi}_2(\text{PO}_4)_3-\text{Na}_2\text{Ti}_2(\text{PO}_4)_3$ system was performed in the past through the formation of $\text{Na}_x\text{Ti}_2(\text{PO}_4)_3$ single phases at ~900 °C, not stable at room temperature but disproportionate²⁶. Delmas et al. also demonstrated the chemical short circuit method at the particle level by wetting a mixture of $\text{Li}_3\text{Ti}_2(\text{PO}_4)_3$ and $\text{LiTi}_2(\text{PO}_4)_3$ with an electrolyte to form an intermediate phase of composition $\text{Li}_{1.23}\text{Ti}_2(\text{PO}_4)_3$ (ref. 27). Here we discover that various intermediate single-phase c- $\text{Na}_x\text{V}_2(\text{PO}_4)_3$ compositions ($1.5 \leq x \leq 2.5$), stable at room temperature, can be accessed through an annealing process at moderate temperatures.

As mentioned earlier^{15,16}, an original phase of e- $\text{Na}_2\text{V}_2(\text{PO}_4)_3$ composition had been electrochemically observed during battery operation, and its crystal structure differs substantially from that of the

Table 1 | Computed volumes, relative energies (relative to e-GS), occupation of the Na(1) and Na(2) sites and V–V distances for $\text{Na}_x\text{V}_2(\text{PO}_4)_3$, $\text{Na}_{1.5}\text{V}_2(\text{PO}_4)_3$ and $\text{Na}_2\text{V}_2(\text{PO}_4)_3$

$\text{Na}_x\text{V}_2(\text{PO}_4)_3$	State	Volume (\AA^3 f.u. $^{-1}$)	ΔE (meV per atom)	Na(1)-occ	Na(2)-occ	$d(V-V)$ (\AA)	$D(V-V)$ (\AA)
$x=1$	e-GS	219.499	0	1.00	0	4.543	6.042
	Metastable- α	220.063	10.56	0.75	0.08	4.554	6.083
	Metastable- β	221.168	21.06	0.50	0.17	4.549	6.142
	Metastable- γ	222.716	26.44	0.25	0.25	4.559	6.145
$x=1.5$	e-GS	223.465	0	1.00	0.17	4.531	6.088
	Metastable- α	224.648	5.68	0.75	0.25	4.529	6.166
	Metastable- β	225.000	12.43	0.50	0.33	4.512	6.196
$x=2$	e-GS	227.159	0	1.00	0.33	4.510	6.156
	Metastable- α	228.870	6.00	0.75	0.42	4.547	6.196
	Metastable- β	230.242	10.26	0.50	0.50	4.525	6.294

Metastable refers to the structure with a partially occupied Na(1) site and has the lowest relative energy ΔE among its analogues with the same Na(1)-occ; Na(1)-occ, occupation of Na(1) site; Na(2)-occ, occupation of Na(2) site. Different metastable configurations, as characterized by their unique Na(1) or Na(2) occupation, are indicated as α , β and γ . The $d(V-V)$ is the average distance between two vanadium sites belonging to the same lantern unit; $D(V-V)$ corresponds to the average V–V distance between two adjacent lantern units along the [001]_{hex} direction. Computed density of states for different phases and a schematic of the structural distribution of Na and vacancies are given in the Supplementary Information. Reminder, $\text{Na}(1)+3\text{Na}(2)=x$ in $\text{Na}_x\text{V}_2(\text{PO}_4)_3$.

c- $\text{Na}_2\text{V}_2(\text{PO}_4)_3$, obtained by the chemical reaction of the mixture of the two end members, as discussed now. Figure 2a compares the corresponding SXRD patterns, indexed in the P_{2_1}/c and $R-3c$ space groups, respectively. The reflection peaks observed at Q (with $Q=4\pi\cdot\sin(\theta)/\lambda$ and λ the wavelength of the X-ray radiation) = 0.51, 1.15 and 1.25\AA^{-1} for the e- $\text{Na}_2\text{V}_2(\text{PO}_4)_3$ phase (indexed with a monoclinic cell, P_{2_1}/c) are absent in the c- $\text{Na}_2\text{V}_2(\text{PO}_4)_3$ phase in the rhombohedral space group $R-3c$. For the c- $\text{Na}_2\text{V}_2(\text{PO}_4)_3$ phase, some diffraction peaks are unindexed (marked with asterisks). Using several commonly observed space groups for NASICON compositions, such as $R32$, $P2/m$, $P2/c$, $P2_1/c$ and $P-1$, the monoclinic space group $P2/m$ with lattice parameters $a=14.8094 \text{\AA}$, $b=8.6597 \text{\AA}$, $c=7.4997 \text{\AA}$, the angle $\beta=99.7135^\circ$ and $V/Z=237.00 \text{\AA}^3$ could fully index the experimental XRD pattern of c- $\text{Na}_2\text{V}_2(\text{PO}_4)_3$ (Extended Data Fig. 3). However, some of these diffraction peaks at $0.65-0.9 \text{\AA}^{-1}$ in Q space are asymmetric and ‘diffuse’, which prevented us from finding a full description of the structure. Therefore, an average structure of higher symmetry ($R-3c$) was used in this study to describe c- $\text{Na}_2\text{V}_2(\text{PO}_4)_3$, as this approach had been shown¹⁵ to be highly appropriate for describing the Na distribution in e- $\text{Na}_2\text{V}_2(\text{PO}_4)_3$. Indeed, in both descriptions of e- $\text{Na}_2\text{V}_2(\text{PO}_4)_3$ (using the average ($R-3c$) or more precise ($P2_1/c$) structures), the Na(1) sites (labelled Na(1) in $R-3c$ and Na(1a), Na(1b) in $P2_1/c$) are always fully occupied¹⁵, the monoclinic distortion being nested in the Na(2) ordering. As shown in Extended Data Fig. 4 in the average structure ($R-3c$), some diffraction peak intensities in the simulated XRD patterns are strongly influenced by the respective Na(1) and Na(2) site occupancies, in particular at $Q=1.015 \text{\AA}^{-1}$ (that is, (012) _{$R-3c$}). We find that the Na(1) = 0.66(4) and Na(2) = 0.55(3) distribution is the most adequate.

The cell parameters, the sodium occupancy factors and the V–O distances of both e- $\text{Na}_2\text{V}_2(\text{PO}_4)_3$ and c- $\text{Na}_2\text{V}_2(\text{PO}_4)_3$ were analysed by Rietveld refinements, as summarized in Extended Data Table 1. It appears that both e- $\text{Na}_2\text{V}_2(\text{PO}_4)_3$ and c- $\text{Na}_2\text{V}_2(\text{PO}_4)_3$ are similar in that they have the same NASICON-type framework, but a substantial difference exists in the distribution of sodium ions between the two compounds. In the case of e- $\text{Na}_2\text{V}_2(\text{PO}_4)_3$, the Na(1) site is fully occupied, and one-third of the Na(2) site is filled. Both structural models ($P2_1/c$ and $R-3c$) for e- $\text{Na}_2\text{V}_2(\text{PO}_4)_3$ show excellent correlation between cell volumes, sodium occupancies and V–O distances. By contrast, in the case of c- $\text{Na}_2\text{V}_2(\text{PO}_4)_3$, Na(1) is not fully occupied but two-thirds occupied, and the remaining Na⁺ ions are located at the Na(2) site (0.55(3)). This can be supported by examining the V–V distances in the NASICON structure. On the one hand, both structures (e- $\text{Na}_2\text{V}_2(\text{PO}_4)_3$ and c- $\text{Na}_2\text{V}_2(\text{PO}_4)_3$) have a similar V–V distance within a given lantern unit (intra-lantern),

with values of $4.458(18) \text{\AA}$ and $4.457(3) \text{\AA}$, respectively. On the other hand, the V–V distances along the [001]_{hex} direction between two different lantern units (inter-lantern) are different for e- $\text{Na}_2\text{V}_2(\text{PO}_4)_3$ and c- $\text{Na}_2\text{V}_2(\text{PO}_4)_3$. In e- $\text{Na}_2\text{V}_2(\text{PO}_4)_3$, the inter-lantern V–V distance is $6.24(3) \text{\AA}$, whereas in c- $\text{Na}_2\text{V}_2(\text{PO}_4)_3$, it is $6.44(3) \text{\AA}$. These important differences suggest that the structures are noticeably different. Indeed, since the Na(1) sites are located between two lantern units along [001]_{hex}, partial occupation implies lower screening (that is, stronger electrostatic repulsions) between triangular oxygen octahedral faces from two lantern units, and thus longer inter-lantern V–V distances. Note that an empty or partially filled Na(1) site in the NASICON structure is very rarely encountered. Na-free NASICON structures include $\text{Fe}^{III}_2(\text{SO}_4)_3$, $\text{NbTi}(\text{PO}_4)_3$ and $\text{Nb}_2(\text{PO}_4)_3$ (ref. 5). The Na(1) site is fully occupied in $\text{NaTi}_2(\text{PO}_4)_3$ (ref. 28), $\text{Na}_3\text{Fe}_2(\text{PO}_4)_3$ (ref. 29), $\text{Na}_2\text{TiFe}(\text{PO}_4)_3$ (ref. 30), $\text{Na}_2\text{TiCr}(\text{PO}_4)_3$ (ref. 31) and $\text{Na}_2\text{VTi}(\text{PO}_4)_3$ (refs. 32,33). Hence, the partial occupancy of the Na(1) site in c- $\text{Na}_2\text{V}_2(\text{PO}_4)_3$ appears rather unique, which we attempt to rationalize.

The relatively high temperature ($\sim 500^\circ\text{C}$) we used for preparing c- $\text{Na}_3\text{V}_2(\text{PO}_4)_3$ is probably the origin of the main difference in Na(1) site occupancy when compared with e- $\text{Na}_3\text{V}_2(\text{PO}_4)_3$, obtained at room temperature through a solid–liquid interface. We previously demonstrated that in $\text{Na}_3\text{V}_2(\text{PO}_4)_3$, the population of the Na(1) site changes with temperature, from fully occupied in the α -monoclinic phase ($C2/c$) at room temperature to fractional occupancies in the γ -rhombohedral phase ($R-3c$) at 200°C (ref. 19). Therefore it is possible that the reaction of $\text{Na}_3\text{V}_2(\text{PO}_4)_3$ with $\text{Na}_1\text{V}_2(\text{PO}_4)_3$ at $\sim 500^\circ\text{C}$ may produce c- $\text{Na}_x\text{V}_2(\text{PO}_4)_3$ with fractional occupancies at the Na(1) site.

These experimental findings and interpretations are further strengthened by our published theoretical work¹⁶ that highlights the presence of a single-phase region associated with the mixed-valence phase $\text{Na}_2\text{V}_2(\text{PO}_4)_3$, as illustrated in Supplementary Fig. 5. At 300 K, no isolated single phase would be expected while performing electrochemistry between $\text{Na}_3\text{V}_2(\text{PO}_4)_3$ and $\text{Na}_1\text{V}_2(\text{PO}_4)_3$, and thus e- $\text{Na}_2\text{V}_2(\text{PO}_4)_3$ obtained from an operando electrochemical experiment performed at room temperature should be mixed with the $\text{Na}_1\text{V}_2(\text{PO}_4)_3$ phase or the $\text{Na}_3\text{V}_2(\text{PO}_4)_3$ phase. However, when higher temperature syntheses are conducted, that is, at temperature $T > 500 \text{ K}$, the stability region of $\text{Na}_2\text{V}_2(\text{PO}_4)_3$ is much enlarged, and thus c- $\text{Na}_2\text{V}_2(\text{PO}_4)_3$ tends to exist as an isolated thermodynamic single phase. Our theoretical works^{16,34} have confirmed the possibility of probing disordered $\text{Na}_1\text{V}_2(\text{PO}_4)_3$, $\text{Na}_{1.5}\text{V}_2(\text{PO}_4)_3$ and $\text{Na}_2\text{V}_2(\text{PO}_4)_3$ configurations, characterized by the specific partial fractional occupations of both Na(1) and Na(2) sites, thus explaining the chemically prepared or electrochemically obtained phases. We found

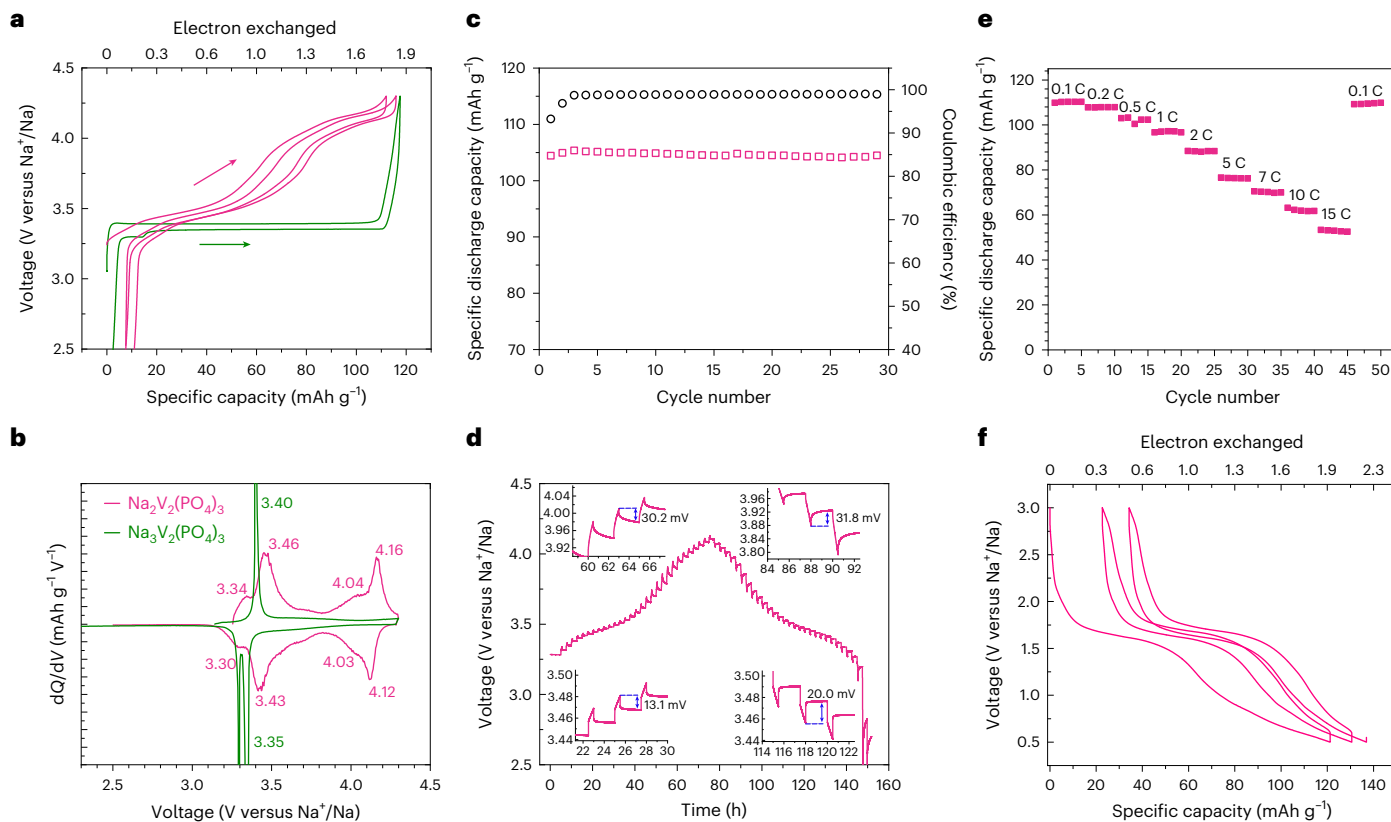


Fig. 3 | Electrochemistry of c- $\text{Na}_2\text{V}_2(\text{PO}_4)_3$. **a**, Electrochemical charge and discharge profiles of $\text{Na}_2\text{V}_2(\text{PO}_4)_3$ (green) and c- $\text{Na}_2\text{V}_2(\text{PO}_4)_3$ (pink) electrodes cycled between 2.5 and 4.3 V at C/10 (one Na^+ in 10 h) versus Na metal. **b**, Derivative (dQ/dV) plots of the first charge and discharge cycles obtained for c- $\text{Na}_2\text{V}_2(\text{PO}_4)_3$ and $\text{Na}_3\text{V}_2(\text{PO}_4)_3$ electrodes. **c**, Discharge capacities and coulombic efficiencies of the c- $\text{Na}_2\text{V}_2(\text{PO}_4)_3$ electrode upon 30 cycles. **d**, GITT

curve of c- $\text{Na}_2\text{V}_2(\text{PO}_4)_3$ electrode versus Na metal during the first electrochemical charge–discharge cycle. The insets show zoomed-in views. **e**, Rate capability of c- $\text{Na}_2\text{V}_2(\text{PO}_4)_3$ electrode versus Na metal with various C rates from 0.1 C to 15 C. **f**, Electrochemical charge and discharge profiles of c- $\text{Na}_2\text{V}_2(\text{PO}_4)_3$ electrodes cycled between 1.3 and 3.0 V at C/10.

that the local charge arrangements on the vanadium sites with higher/lower oxidation states may disrupt potentially stable structural arrangement between Na ions and their vacancies in $\text{Na}_x\text{M}_2(\text{PO}_4)_3$, thus lowering the migration barriers and enhancing the jump diffusivity of Na^+ , which, in turn, will enable the extraction of the ‘last’ Na^+ ion. For example, some of us recently determined that if compositions with low Na content (that is, $\text{Na}_{0+x}\text{V}_2(\text{PO}_4)_3$ with $x < 1$) were thermodynamically stable, the Na^+ extraction from $\text{Na}_1\text{V}_2(\text{PO}_4)_3$ towards an empty Na phase (that is, $\text{V}_2(\text{PO}_4)_3$) would be kinetically facilitated by the local charge arrangement of the mixed-valence vanadium sites $\text{V}^{4+/5+}$ at highly charged state³⁴.

To complement these statements, Table 1 provides energetics computed with first-principles calculations of different Na-vacancy orderings, whose Na site occupations correspond to the c- $\text{Na}_2\text{V}_2(\text{PO}_4)_3$ and e- $\text{Na}_2\text{V}_2(\text{PO}_4)_3$ structures. These calculations rationalize the structural differences between the c- $\text{Na}_2\text{V}_2(\text{PO}_4)_3$ and e- $\text{Na}_2\text{V}_2(\text{PO}_4)_3$ structures. The electrochemically observed $\text{Na}_2\text{V}_2(\text{PO}_4)_3$ phase is the ground state (electrochemical ground state, e-GS in Table 1), whereas the chemically prepared c- $\text{Na}_2\text{V}_2(\text{PO}_4)_3$ phase appears as a metastable structure. Indeed, the first is characterized by the full occupancy of the Na(1) site, whereas the second shows fractional occupations of the Na(1) and Na(2) sites. Table 1 also shows the computed Na-disordered structures for $\text{Na}_{1.5}\text{V}_2(\text{PO}_4)_3$ and $\text{Na}_1\text{V}_2(\text{PO}_4)_3$ compositions (Supplementary Figs. 6 and 7). The e-GS shows full occupation of the Na(1) site, whereas the metastable structures ($\alpha/\beta/\gamma$) display a partially occupied Na(1) site. Note that for an equal Na distribution among the Na(1) and Na(2) sites, $\text{Na}_2\text{V}_2(\text{PO}_4)_3$, $\text{Na}_{1.5}\text{V}_2(\text{PO}_4)_3$ and $\text{Na}_1\text{V}_2(\text{PO}_4)_3$ show very mild metastability (with energies of <25 meV per atom). This indicates that changes in Na-vacancy orderings (to accommodate

changes in the composition) in the metastable structures ($\alpha/\beta/\gamma$) can be accessed electrochemically, which is a strong indication of the solid solution mechanism for Na^+ extraction from these compositions. The depopulation of the Na(1) site in the metastable structures increases the volume (per formula unit) in $\text{Na}_x\text{V}_2(\text{PO}_4)_3$ versus the corresponding e-GS (Table 1 and Supplementary Fig. 8), in excellent agreement with volumes experimentally determined from Rietveld refinements for c- $\text{Na}_2\text{V}_2(\text{PO}_4)_3$ and e- $\text{Na}_2\text{V}_2(\text{PO}_4)_3$ (Extended Data Table 1). Notably, a $\text{Na}_2\text{V}_2(\text{PO}_4)_3$ configuration that has similar Na(1) and Na(2) occupations (that is, 0.66 for Na(1) and 0.55 for Na(2), for an effective composition of $\text{Na}_{2.31(12)}\text{V}_2(\text{PO}_4)_3$) exhibits a larger cell volume by ~1.4% than the corresponding ordered e-GS structure (that is, e- $\text{Na}_2\text{V}_2(\text{PO}_4)_3$). As mentioned earlier, this increase of the unit-cell volume in $\text{Na}_2\text{V}_2(\text{PO}_4)_3$ can be attributed to a depopulation of the Na(1) sites that increases the inter-lantern vanadium–vanadium distance ($D(\text{V}-\text{V})$; Fig. 2b). Hence we show that the partial occupation of the Na(1) site induces an increase in the unit-cell volume per formula unit, but with small changes in energies (<25 meV per atom), moving from the ordered to the disordered structures. In all three compositions examined, that is, $x = 1$, $x = 1.5$ and $x = 2.0$, the metastability of Na-vacancy orderings in $\text{Na}_x\text{V}_2(\text{PO}_4)_3$ appears accessible at room temperature, which indicates that these c- $\text{Na}_2\text{V}_2(\text{PO}_4)_3$ phases are accessible via electrochemical methods due to high Na solubility in this NASICON framework.

Electrochemical properties of c- $\text{Na}_2\text{V}_2(\text{PO}_4)_3$

The electrochemical properties of c- $\text{Na}_2\text{V}_2(\text{PO}_4)_3$ were investigated and are compared with those obtained for the conventional well-known $\text{Na}_3\text{V}_2(\text{PO}_4)_3$ (Fig. 3). Charge and discharge voltage–composition

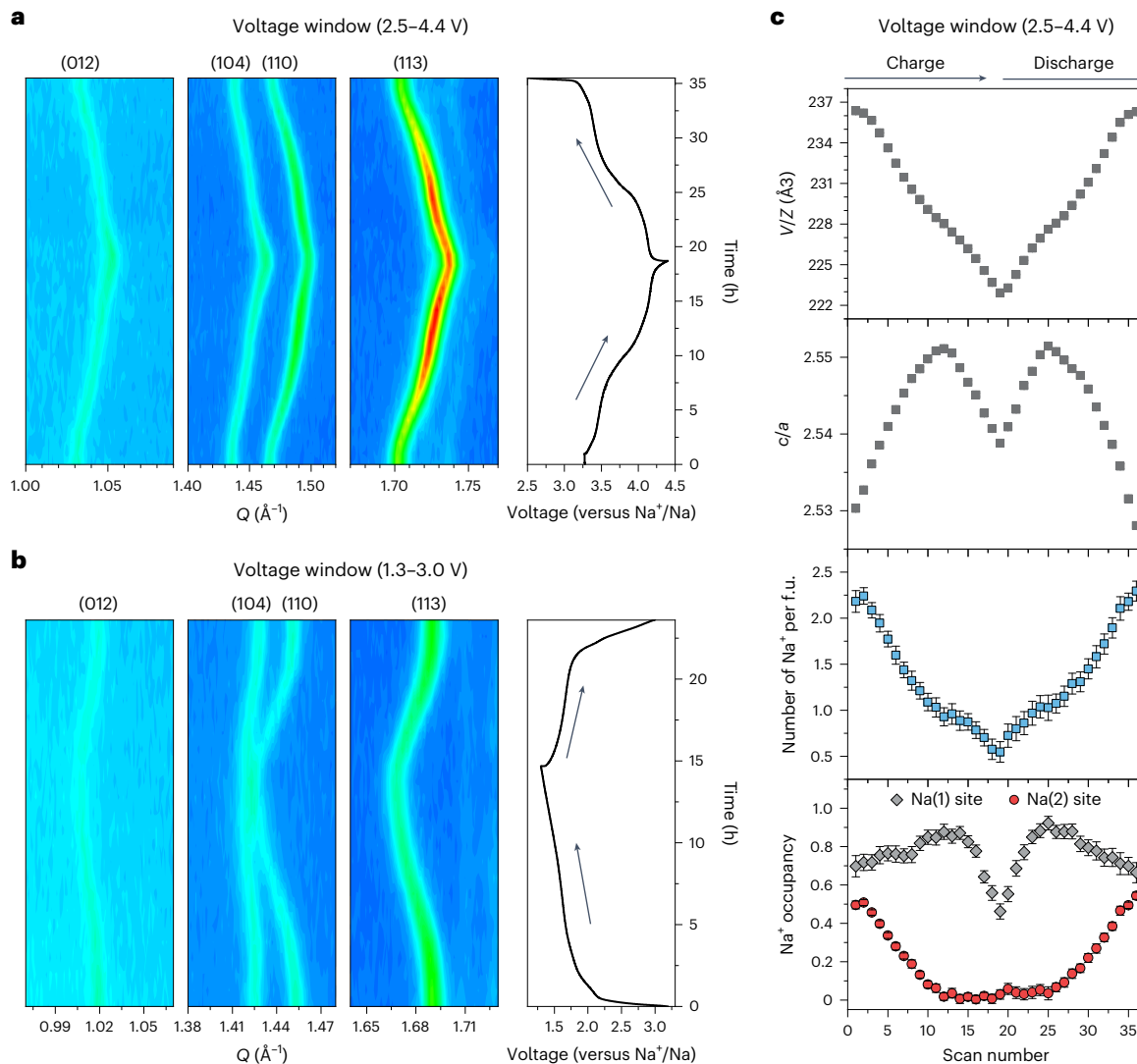


Fig. 4 | Structural evolution during battery operation. **a,b**, Operando XRD measurements using c-Na₂V₂(PO₄)₃ as a positive electrode in a half cell versus Na metal upon charge and discharge cycles, within voltage windows of 1.3–3.0 V (**b**) versus Na⁺/Na at C/10 (that is, one Na⁺ in 10 h) and 2.5–4.4 Volts (**a**). The right-hand plot shows voltage over time. **c**, Corresponding results (Na site

occupancies, number of Na⁺ per formula unit (f.u.), c/a ratio and V/Z) from Rietveld refinements within the voltage window of 2.5–4.4 Volts upon charge (scan numbers 1–19) and discharge (scan numbers 19–36). The error bars refer to standard deviations arising from the Rietveld refinements.

profiles of Na₂V₂(PO₄)₃ obtained during the first two cycles, with a half-cell configuration versus Na metal, are represented in Fig. 3a. Remarkably, c-Na₂V₂(PO₄)₃ (in pink) exhibits a sloping voltage–composition profile, unlike conventional Na₃V₂(PO₄)₃ (in green), which operates through a voltage–composition plateau at around 3.37 Volts versus Na. The first charge and discharge capacities of c-Na₂V₂(PO₄)₃ are 112 and 104 mAh g⁻¹, respectively.

Approximately 1.8 Na⁺ per formula unit was extracted from c-Na₂V₂(PO₄)₃ during the first charge, meaning that much less than one Na⁺ remains in the structure at the end of charge. This fact is remarkable, as for many other vanadium (V)-based NASICON-type materials, including the conventional Na₃V₂(PO₄)₃, one Na⁺ ion (that is, Na₁V₂(PO₄)₃) always remains in the structure at the end of the charge^{35–40}. In addition, Na₂V₂(PO₄)₃ operates at a much increased average voltage of ~3.70 Volts versus Na, compared to 3.37 Volts for the conventional Na₃V₂(PO₄)₃. As evidenced by the differential capacity curve (dQ/dV versus V) of Fig. 3b, the voltage–composition profile observed upon Na⁺ extraction from c-Na₂V₂(PO₄)₃ can be divided into two domains, at around 3.42 and 4.12 V versus Na, respectively. Approximately two

Na⁺ ions are reversibly extracted from Na₂V³⁺V⁴⁺(PO₄)₃, and the two distinct domains are ascribed to (1) the V^{4+/3+} redox couple at ~3.45 V versus Na/Na⁺ and (2) the V^{5+/4+} redox couple at ~4.15 V versus Na/Na⁺. Indeed, prior work on Na_xMV(PO₄)₃ (M = Al (ref. 37), Mn (refs. 41–49) or Fe (refs. 50–53)) by us and others has identified the V^{5+/4+} redox couple in NASICONs at a voltage close to ~4.0 Volts. Importantly, the redox activity at ~4.10 Volts of c-Na₂V₂(PO₄)₃ signifies that such electrodes possess a theoretical energy density approximately 15.5% higher than conventional Na₃V₂(PO₄)₃, exhibiting a discharge capacity of 104 mAh g⁻¹ after 29 cycles (Fig. 3c). In addition, galvanostatic intermittent titration technique (GITT) experiments of c-Na₂V₂(PO₄)₃ recorded during the first electrochemical cycle show a small overpotential (around 10–30 mVolts) over the whole voltage range during both charge and discharge, indicating good kinetics for Na⁺ diffusion (Fig. 3d). This is further shown in Fig. 3e, which illustrates the rate capability of the studied material measured for several rates expressed in units of C from 0.1 C to 15 C, with a 1 C rate meaning full charge over a period of 1 h (and 0.1 C a full charge over 10 h and 15 C a full charge in 4 min). The discharge capacity measured at 15 C corresponds to 48.6% of that obtained at 0.1 C.

As shown in Fig. 3f, approximately two Na^+ ions can be reversibly intercalated into c- $\text{Na}_2\text{V}_2(\text{PO}_4)_3$, down to 0.5 Volts versus Na^+/Na , most likely including partial electrolyte degradation through a parasitic reaction at low voltage (solid electrolyte interphase (SEI)). Extended Data Fig. 5 further supports this as it illustrates the full reversibility of the overall system, between 0.5 and 4.5 Volts for a global utilization of the $\text{Na}_x\text{V}_2(\text{PO}_4)_3$ framework with $0 \leq x \leq 4$. This may open the door for fabricating symmetrical $\text{Na}_2\text{V}_2(\text{PO}_4)_3/\text{electrolyte}/\text{Na}_2\text{V}_2(\text{PO}_4)_3$ cells, with liquid or solid electrolytes.

Using the local cluster expansion-based model of Wang et al.³⁴, we further evaluated the migration barriers of Na^+ for different phases of $\text{Na}_2\text{V}_2(\text{PO}_4)_3$, that is, the e-GS with fully occupied Na(1); metastable α -state with Na(1) occupancy of 0.75; and metastable β -state with Na(1) occupancy of 0.5 (Table 1). Na^+ migration barriers between the Na(1) and Na(2) sites in $\text{Na}_2\text{V}_2(\text{PO}_4)_3$ tend to decrease, following the sequence of ~744.9 meV for e-GS > -602.3 meV for metastable α -state > -438.0 meV for metastable β -state structures. This decrease of Na^+ migration barriers in $\text{Na}_2\text{V}_2(\text{PO}_4)_3$ configurations with less-occupied Na(1) sites indicates that disorder among the Na(1) and Na(2) sites eases the kinetics of Na^+ migration through vacancy-mediated mechanisms.

Structural evolution upon Na^+ extraction/insertion

To investigate the structural evolution and Na^+ extraction/insertion mechanism of $\text{Na}_2\text{V}_2(\text{PO}_4)_3$, operando SXRD experiments were performed, between 1.0 and 4.4 Volts versus Na^+/Na at a C rate of C/9 (one Na^+ is extracted in ~9 h), as illustrated in Fig. 4. The single-phase reaction mechanism inferred from the sloping voltage–composition profile is confirmed. The XRD reflection peaks continuously shift, reversibly, towards higher or lower Q space during charge or discharge (Fig. 4a,b), and accordingly the unit-cell volume gradually decreases or increases (Fig. 4c). While ‘classical’ $\text{Na}_3\text{V}_2(\text{PO}_4)_3$ has a flat voltage–composition profile with two successive two-phase reactions ($\text{Na}_3\text{V}_2(\text{PO}_4)_3 \rightarrow \text{Na}_2\text{V}_2(\text{PO}_4)_3$ and $\text{Na}_2\text{V}_2(\text{PO}_4)_3 \rightarrow \text{Na}_1\text{V}_2(\text{PO}_4)_3$), c- $\text{Na}_2\text{V}_2(\text{PO}_4)_3$ shows an entirely different reaction mechanism for Na^+ extraction: a sloping voltage–composition profile and a full solid solution mechanism over the explored voltage region. We propose that the different reaction mechanisms are nested in the different occupation factors of the Na(1) site in e- $\text{Na}_2\text{V}_2(\text{PO}_4)_3$ and c- $\text{Na}_2\text{V}_2(\text{PO}_4)_3$. When V-based NASICON compounds, such as $\text{Na}_4\text{MnV}(\text{PO}_4)_3$ and $\text{Na}_4\text{FeV}(\text{PO}_4)_3$, involve $\text{V}^{4+}/\text{V}^{5+}$ vanadium redox reactions at high voltage, above 3.9 Volts versus Na^+/Na , they often experience an asymmetric electrochemical reaction mechanism in the following discharge^{35–53}. Interestingly, this is not the case for the chemically prepared c- $\text{Na}_2\text{V}_2(\text{PO}_4)_3$. The overall electrochemical reaction is highly reversible and favours electrochemical operation over an extensive number of cycles.

The quantitative structural analysis through Rietveld refinements of the operando SXRD data also shows that the electrochemical reaction during charge and discharge is highly symmetric and reversible (Fig. 4 and Extended Data Table 2). Upon charging to 3.8 Volts versus Na, one Na^+ can be extracted and as a consequence, one Na^+ still remains in the structure, with partially occupied Na(1) and Na(2) sites. The refined parameters of $\text{Na}_1\text{V}_2(\text{PO}_4)_3$ obtained from c- $\text{Na}_2\text{V}_2(\text{PO}_4)_3$ are summarized as they are highly sensitive to the sodium content on the Na(1) site. Interestingly, while having the same composition, ‘classical’ $\text{Na}_1\text{V}_2(\text{PO}_4)_3$ obtained from the extraction of two Na^+ ions from $\text{Na}_3\text{V}_2(\text{PO}_4)_3$ shows different unit-cell dimensions ($a = 8.4276(2)$ Å, $c = 21.4731(4)$ Å, $V/Z = 220.13(1)$ Å³) with Na(1) fully occupied and empty Na(2) sites. The V/Z volumes of the pristine material and of that recovered at the end of charge are $236.35(2)$ Å³ and $222.92(2)$ Å³, respectively, which means that the overall volume change is less than 6% (5.7%; Extended Data Table 2). This is lower than the volume change between ‘conventional’ $\text{Na}_3\text{V}_2(\text{PO}_4)_3$ and $\text{Na}_1\text{V}_2(\text{PO}_4)_3$ (about 8.2%). Interestingly, the c/a ratio increases up to around mid-charge

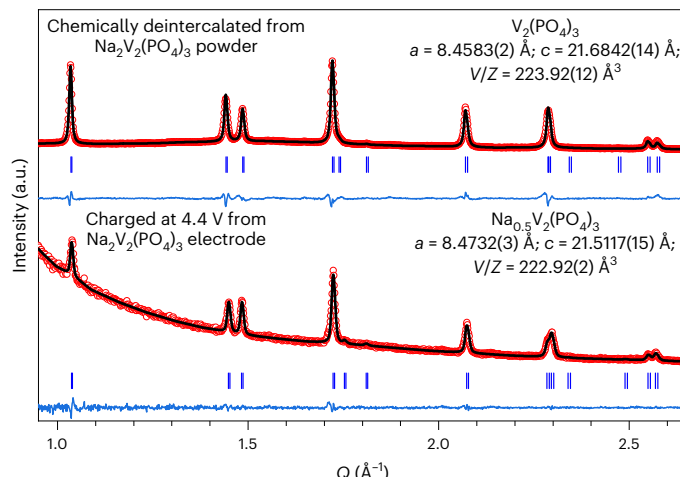


Fig. 5 | XRD patterns of $\text{Na}_x\text{V}_2(\text{PO}_4)_3$ (x close to 0). Rietveld refinements of the XRD patterns collected at the end of charge (4.4 V) during operando measurement and for the chemically deintercalated phase from the c- $\text{Na}_2\text{V}_2(\text{PO}_4)_3$ powder. Refined structural parameters are listed in Extended Data Table 3.

(scan no. 12) and then decreases until the end of charge. When it comes to Na^+ occupancy, the total number of Na^+ ions in the structure gradually decreases during charge and then increases during discharge. However, the contribution to the decreasing number of Na^+ ions until mid-charge is due to the depopulation of the Na(2) site with a partial transfer of Na^+ ions from the Na(2) site to the Na(1) site: the decreasing occupancy of Na(2), until zero at mid-charge, is thus observed in parallel with an increasing occupancy of Na(1). From scan no. 14, the depopulation of the Na(1) site occurs until the end of charge (Fig. 4c).

To ensure full oxidation of c- $\text{Na}_2\text{V}_2(\text{PO}_4)_3$, and for comparison to the composition obtained operando at the end of charge, chemical deintercalation from c- $\text{Na}_2\text{V}_2(\text{PO}_4)_3$ was carried out. The XRD profiles analysed by Rietveld refinements and structural parameters are compared in Fig. 5. The a parameter is further decreased for the chemically deintercalated phase in comparison to that observed for the composition recovered at the end of charge. By contrast, the c and V/Z parameters slightly increase. The occupancy factors for the Na(1) and Na(2) sites after the chemical deintercalation are zero, suggesting that full extraction of Na was achieved after the chemical oxidation process. The value of the V–O distance also supports this: it was $1.89(15)$ Å after chemical deintercalation but $1.92(3)$ Å at the end of the charge of up to 4.4 V versus Na^+/Na . We were able to obtain the composition $\text{V}_2(\text{PO}_4)_3$ with no residual alkali ions in the NASICON host structure and with a smaller V/Z unit-cell volume reported for a $\text{Na}_x\text{V}_2(\text{PO}_4)_3$ NASICON structure (Extended Data Table 3).

This study presents a different class of NASICON-related materials synthesized by a straightforward route. The great tunability of NASICON materials will allow many transition metals to be substituted, and thus we envisage many different NASICON-type compositions being discovered, containing Ti, V, Fe or Mn as redox-active transition metal elements. The unconventional synthesis procedure developed in this study enabled us to discover phases (Extended Data Fig. 6) that would be otherwise difficult to obtain through more conventional material synthesis routes.

Online content

Any methods, additional references, Nature Portfolio reporting summaries, source data, extended data, supplementary information, acknowledgements, peer review information; details of author contributions and competing interests; and statements of data and code availability are available at <https://doi.org/10.1038/s41563-024-02023-7>.

References

1. Armand, M. & Tarascon, J.-M. Building better batteries. *Nature* **451**, 652–657 (2008).
2. Tarascon, J. M. Is lithium the new gold? *Nat. Chem.* **2**, 510 (2010).
3. Yabuuchi, N. et al. Research development on sodium-ion batteries. *Chem. Rev.* **114**, 11636–11682 (2014).
4. Delmas, C. Sodium and sodium-ion batteries: 50 years of research. *Adv. Energy Mater.* **8**, 1703137 (2018).
5. Masquelier, C. & Croguennec, L. Polyanionic (phosphates, silicates, sulfates) frameworks as electrode materials for rechargeable Li (or Na) batteries. *Chem. Rev.* **113**, 6552–6591 (2013).
6. Han, M. H., Gonzalo, E., Singh, G. & Rojo, T. A comprehensive review of sodium layered oxides: powerful cathodes for Na-ion batteries. *Energy Environ. Sci.* **8**, 81–102 (2015).
7. Hosaka, T., Kubota, K., Hameed, A. S. & Komaba, S. Research development on K-ion batteries. *Chem. Rev.* **120**, 6358–6466 (2020).
8. Hasa, I. et al. Challenges of today for Na-based batteries of the future: from materials to cell metrics. *J. Power Sources* **482**, 228872 (2021).
9. Singh, B. et al. A chemical map of NaSICON electrode materials for sodium-ion batteries. *J. Mater. Chem. A* **9**, 281–292 (2021).
10. Ouyang, B. et al. Synthetic accessibility and stability rules of NASICONs. *Nat. Commun.* **12**, 5752 (2021).
11. Uebou, Y. et al. Electrochemical sodium insertion into the 3D-framework of $\text{Na}_3\text{M}_2(\text{PO}_4)_3$ ($\text{M}=\text{Fe}, \text{V}$). *Rep. Inst. Adv. Mater. Study Kyushu Univ.* **16**, 1–5 (2002).
12. Lim, S. Y., Kim, H., Shakoor, R. A., Jung, Y. & Choi, J. W. Electrochemical and thermal properties of NASICON structured $\text{Na}_3\text{V}_2(\text{PO}_4)_3$ as a sodium rechargeable battery cathode: a combined experimental and theoretical study. *J. Electrochem. Soc.* **159**, A1393–A1397 (2012).
13. Saravanan, K., Mason, C. W., Rudola, A., Wong, K. H. & Balaya, P. The first report on excellent cycling stability and superior rate capability of $\text{Na}_3\text{V}_2(\text{PO}_4)_3$ for sodium ion batteries. *Adv. Energy Mater.* **3**, 444–450 (2013).
14. Ishado, Y., Inoishi, A. & Okada, S. Exploring factors limiting three- Na^+ extraction from $\text{Na}_3\text{V}_2(\text{PO}_4)_3$. *Electrochemistry* **88**, 457–462 (2020).
15. Park, S. et al. Crystal structure of $\text{Na}_2\text{V}_2(\text{PO}_4)_3$, an intriguing phase spotted in the $\text{Na}_3\text{V}_2(\text{PO}_4)_3\text{-Na}_1\text{V}_2(\text{PO}_4)_3$ system. *Chem. Mater.* **34**, 451–462 (2022).
16. Wang, Z. et al. Phase stability and sodium-vacancy orderings in a NaSICON electrode. *J. Mater. Chem. A* **10**, 209–217 (2022).
17. Zakharkin, M. V. et al. Electrochemical properties and evolution of the phase transformation behavior in the NASICON-type $\text{Na}_{3+x}\text{Mn}_x\text{V}_{2-x}(\text{PO}_4)_3$ ($0 \leq x \leq 1$) cathodes for Na-ion batteries. *J. Power Sources* **470**, 228231 (2020).
18. Orikasa, Y. et al. Direct observation of a metastable crystal phase of Li_xFePO_4 under electrochemical phase transition. *J. Am. Chem. Soc.* **135**, 5497–5500 (2013).
19. Chotard, J.-N. et al. Discovery of a sodium-ordered form of $\text{Na}_3\text{V}_2(\text{PO}_4)_3$ below ambient temperature. *Chem. Mater.* **27**, 5982–5987 (2015).
20. Delacourt, C., Poizot, P., Tarascon, J. M. & Masquelier, C. The existence of a temperature-driven solid solution in Li_xFePO_4 for $0 \leq x \leq 1$. *Nat. Mater.* **4**, 254–260 (2005).
21. Lu, J., Oyama, G., Nishimura, S. I. & Yamada, A. Increased conductivity in the metastable intermediate in Li_xFePO_4 electrode. *Chem. Mater.* **28**, 1101–1106 (2016).
22. Delacourt, C., Rodríguez-Carvajal, J., Schmitt, B., Tarascon, J. M. & Masquelier, C. Crystal chemistry of the olivine-type Li_xFePO_4 system ($0 \leq x \leq 1$) between 25 and 370 °C. *Solid State Sci.* **7**, 1506–1516 (2005).
23. Chen, G., Song, X. & Richardson, T. J. Metastable solid-solution phases in the $\text{LiFePO}_4/\text{FePO}_4$ system. *J. Electrochem. Soc.* **154**, A627–A632 (2007).
24. Dodd, J. L., Yazami, R. & Fultz, B. Phase diagram of Li_xFePO_4 . *Electrochem. Solid State Lett.* **9**, 151–155 (2006).
25. Nishimura, S. I., Natsui, R. & Yamada, A. Superstructure in the metastable intermediate-phase $\text{Li}_{2/3}\text{FePO}_4$ accelerating the lithium battery cathode reaction. *Angew. Chem. Int. Ed.* **54**, 8939–8942 (2015).
26. Delmas, C., Cherkaoui, F., Nadiri, A. & Hagenmuller, P. A NASICON-type phase as intercalation electrode: $\text{NaTi}_2(\text{PO}_4)_3$. *Mater. Res. Bull.* **22**, 631–639 (1987).
27. Delmas, C. & Nadiri, A. The chemical short circuit method. An improvement in the intercalation-deintercalation techniques. *Mater. Res. Bull.* **23**, 65–72 (1988).
28. Hagenmuller, P. & Delmas, C. Intercalation in 3-D skeleton structures: ionic and electronic features. *MRS Online Proc. Libr.* **210**, 323–334 (1990).
29. d'Yvoire, F., Pintard-Scrépel, M., Bretey, E. & de la Rochère, M. Phase transitions and ionic conduction in 3D skeleton phosphates $\text{A}_3\text{M}_2(\text{PO}_4)_3$; $\text{A} = \text{Li}, \text{Na}, \text{Ag}, \text{K}; \text{M} = \text{Cr}, \text{Fe}$. *Solid State Ion.* **9–10**, 851–857 (1983).
30. Patoux, S., Rousse, G., Leriche, J. B. & Masquelier, C. Structural and electrochemical studies of rhombohedral $\text{Na}_2\text{TiM}(\text{PO}_4)_3$ and $\text{Li}_{1.6}\text{Na}_0.4\text{TiM}(\text{PO}_4)_3$ ($\text{M} = \text{Fe}, \text{Cr}$) phosphates. *Chem. Mater.* **15**, 2084–2093 (2003).
31. Kawai, K., Asakura, D., Nishimura, S.-I. & Yamada, A. Stabilization of a 4.5 V $\text{Cr}^{4+}/\text{Cr}^{3+}$ redox reaction in NASICON-type $\text{Na}_3\text{Cr}_2(\text{PO}_4)_3$ by Ti substitution. *Chem. Commun.* **55**, 13717–13720 (2019).
32. Wang, D. et al. Sodium vanadium titanium phosphate electrode for symmetric sodium-ion batteries with high power and long lifespan. *Nat. Commun.* **8**, 15888 (2017).
33. Lalere, F., Seznec, V., Courty, M., Chotard, J. N. & Masquelier, C. Coupled X-ray diffraction and electrochemical studies of the mixed Ti/V-containing NASICON: $\text{Na}_2\text{TiV}(\text{PO}_4)_3$. *J. Mater. Chem. A* **6**, 6654–6659 (2018).
34. Wang, Z. et al. Kinetic Monte Carlo simulations of sodium ion transport in NaSICON electrodes. *ACS Mater. Lett.* **5**, 2499–2507 (2023).
35. Chen, F. et al. A NASICON-type positive electrode for Na batteries with high energy density: $\text{Na}_4\text{MnV}(\text{PO}_4)_3$. *Small Methods* **3**, 1800218 (2018).
36. Park, S. et al. An asymmetric sodium extraction/insertion mechanism for the Fe/V-mixed NASICON $\text{Na}_4\text{FeV}(\text{PO}_4)_3$. *Chem. Mater.* **34**, 4142–4152 (2022).
37. Lalère, F. et al. Improving the energy density of $\text{Na}_3\text{V}_2(\text{PO}_4)_3$ -based positive electrodes through V/Al substitution. *J. Mater. Chem. A* **3**, 16198–16205 (2015).
38. Liu, R. et al. Exploring highly reversible 1.5-electron reactions ($\text{V}^{3+}/\text{V}^{4+}/\text{V}^{5+}$) in $\text{Na}_3\text{VCr}(\text{PO}_4)_3$ cathode for sodium-ion batteries. *ACS Appl. Mater. Interfaces* **9**, 43632–43639 (2017).
39. Ghosh, S., Jose, N., Senthilkumar, B., Amonpattarakit, P. & Senguttuvan, P. Multi-redox ($\text{V}^{5+}/\text{V}^{4+}/\text{V}^{3+}/\text{V}^{2+}$) driven asymmetric sodium (de)intercalation reactions in NASICON- $\text{Na}_3\text{VIn}(\text{PO}_4)_3$ cathode. *J. Electrochem. Soc.* **168**, 050534 (2021).
40. Inoishi, A., Yoshioka, Y., Zhao, L., Kitajou, A. & Okada, S. Improvement in the energy density of $\text{Na}_3\text{V}_2(\text{PO}_4)_3$ by Mg substitution. *Chem. ElectroChem* **4**, 2755–2759 (2017).
41. Zhou, W. et al. $\text{Na}_x\text{MV}(\text{PO}_4)_3$ ($\text{M} = \text{Mn}, \text{Fe}, \text{Ni}$) structure and properties for sodium extraction. *Nano Lett.* **16**, 7836–7841 (2016).
42. Zakharkin, M. V. et al. Enhancing Na^+ extraction limit through high voltage activation of the NASICON-type $\text{Na}_4\text{MnV}(\text{PO}_4)_3$ cathode. *ACS Appl. Energy Mater.* **1**, 5842–5846 (2018).
43. Xu, C. et al. Mn-rich phosphate cathodes for Na-ion batteries with superior rate performance. *ACS Energy Lett.* **7**, 97–107 (2022).

44. Soundharajan, V. et al. The advent of manganese-substituted sodium vanadium phosphate-based cathodes for sodium-ion batteries and their current progress: a focused review. *J. Mater. Chem. A* **10**, 1022–1046 (2022).
45. Buryak, N. S. et al. High-voltage structural evolution and its kinetic consequences for the $\text{Na}_4\text{MnV}(\text{PO}_4)_3$ sodium-ion battery cathode material. *J. Power Sources* **518**, 230769 (2022).
46. Anishchenko, D. V., Zakharkin, M. V., Nikitina, V. A., Stevenson, K. J. & Antipov, E. V. Phase boundary propagation kinetics predominately limit the rate capability of NASICON-type $\text{Na}_{3+x}\text{Mn}_x\text{V}_{2-x}(\text{PO}_4)_3$ ($0 \leq x \leq 1$) materials. *Electrochim. Acta* **354**, 136761 (2020).
47. Ghosh, S. et al. High capacity and high-rate NASICON- $\text{Na}_{3.75}\text{V}_{1.25}\text{Mn}_{0.75}(\text{PO}_4)_3$ cathode for Na-ion batteries via modulating electronic and crystal structures. *Adv. Energy Mater.* **10**, 1902918 (2020).
48. Park, S. et al. Irreversible electrochemical reaction at high voltage induced by distortion of Mn and V structural environments in $\text{Na}_4\text{MnV}(\text{PO}_4)_3$. *Chem. Mater.* **35**, 3181–3195 (2023).
49. Perfilyeva, T. I. et al. Complete three-electron vanadium redox in NASICON-type $\text{Na}_3\text{VSc}(\text{PO}_4)_3$ electrode material for Na-ion batteries. *J. Electrochem. Soc.* **168**, 110550 (2021).
50. Park, S. et al. Crystal structures and local environments of NASICON-type $\text{Na}_3\text{FeV}(\text{PO}_4)_3$ and $\text{Na}_4\text{FeV}(\text{PO}_4)_3$ positive electrode materials for Na-ion batteries. *Chem. Mater.* **33**, 5355–5367 (2021).
51. Hadouchi, M. et al. Fast sodium intercalation in $\text{Na}_{3.41}\text{Fe}_{0.59}\text{FeV}(\text{PO}_4)_3$: a novel sodium-deficient NASICON cathode for sodium-ion batteries. *Energy Storage Mater.* **35**, 192–202 (2021).
52. de Boisse, B. M., Ming, J., Nishimura, S. & Yamada, A. Alkaline excess strategy to NASICON-type compounds towards higher-capacity battery electrodes. *J. Electrochem. Soc.* **163**, A1469–A1473 (2016).
53. Xu, C. et al. A novel NASICON-typed $\text{Na}_4\text{VMn}_{0.5}\text{Fe}_{0.5}(\text{PO}_4)_3$ cathode for high-performance Na-ion batteries. *Adv. Energy Mater.* **11**, 2100729 (2021).

Publisher's note Springer Nature remains neutral with regard to jurisdictional claims in published maps and institutional affiliations.

Springer Nature or its licensor (e.g. a society or other partner) holds exclusive rights to this article under a publishing agreement with the author(s) or other rightsholder(s); author self-archiving of the accepted manuscript version of this article is solely governed by the terms of such publishing agreement and applicable law.

© The Author(s), under exclusive licence to Springer Nature Limited 2024

¹Laboratoire de Réactivité et de Chimie des Solides, Université de Picardie Jules Verne, CNRS, Amiens, France. ²Institut de Chimie de la Matière Condensée de Bordeaux (ICM CB), Université de Bordeaux, Bordeaux INP, CNRS, Pessac, France. ³TIAMAT, Amiens, France. ⁴Department of Materials Science and Engineering, National University of Singapore, Singapore, Singapore. ⁵Department of Materials Science and Engineering, Northwestern University, Evanston, IL, USA. ⁶Réseau Français sur le Stockage Electrochimique de l'Energie (RS2E), CNRS, Amiens, France. ⁷ALBA Synchrotron, Consortium for the Exploitation of the Synchrotron Light Laboratory (CELLS), Cerdanyola del Vallès, Spain. ⁸Chemical and Biomolecular Engineering, National University of Singapore, Singapore, Singapore. ⁹Department of Electrical and Computer Engineering, University of Houston, Houston, TX, USA. ¹⁰Institut Universitaire de France, Paris, France. ¹¹These authors contributed equally: Sunkyu Park, Ziliang Wang.  e-mail: pcanepa@central.uh.edu; laurence.croguennec@icmcb.cnrs.fr; christian.masquelier@u-picardie.fr

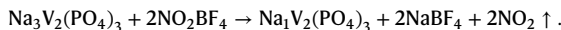
Methods

Synthesis of $\text{Na}_3\text{V}_2(\text{PO}_4)_3$

A carbon-coated VPO_4 precursor was first synthesized by mixing stoichiometric amounts of V_2O_5 (Alfa Aesar, 99.6%), H_3PO_4 (Alfa Aesar, 85%) and agar-agar (Fisher BioReagents) in deionized water to yield a solution that was stirred overnight in an oil bath at 80 °C. A solid residue was obtained, followed by further drying for 12 h overnight in the oven at 250 °C, before being ground again and heated at 890 °C for 2 h in an Ar atmosphere. After that, Na_3PO_4 (Acros Organics, 96%) was mixed with the resulting carbon-coated VPO_4 in a molar ratio of 1:2, and then heated at 800 °C for 2 h in an Ar atmosphere to obtain carbon-coated $\text{Na}_3\text{V}_2(\text{PO}_4)_3$. The prepared pristine $\text{Na}_3\text{V}_2(\text{PO}_4)_3$ powder contains agglomerates of several to tens of micrometres (Supplementary Fig. 2). The carbon content within the carbon-coated $\text{Na}_3\text{V}_2(\text{PO}_4)_3$ powder was about 1.8% in mass, as determined by thermogravimetric analysis (Supplementary Fig. 3).

Preparation of $\text{Na}_1\text{V}_2(\text{PO}_4)_3$ via chemical oxidation process

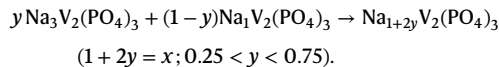
The $\text{Na}_3\text{V}_2(\text{PO}_4)_3$ powder was dispersed in acetonitrile (Sigma-Aldrich, 99.8%) using a magnetic stirrer, and a stoichiometric amount of a 0.1 M solution of nitronium tetrafluoroborate (Sigma-Aldrich, 95%) in acetonitrile was introduced dropwise into the first solution to produce the following chemical reaction:



The resulting dispersed powder in the solution was then filtered and washed with acetonitrile. The whole process was performed in an Ar-filled glove box. The Na/V/P stoichiometry ratios obtained from inductively coupled plasma spectroscopy for $\text{Na}_3\text{V}_2(\text{PO}_4)_3$ and $\text{Na}_1\text{V}_2(\text{PO}_4)_3$ are 3.04(5)/1.97(1)/2.99(4) and 1.01(5)/1.99(2)/2.99(3), respectively, in very good agreement with the target compositions.

Synthesis of $\text{Na}_x\text{V}_2(\text{PO}_4)_3$

$\text{Na}_x\text{V}_2(\text{PO}_4)_3$ compositions ($x = 1.5, 1.75, 2, 2.25, 2.5$) can be prepared with the corresponding molar ratio of $\text{Na}_3\text{V}_2(\text{PO}_4)_3$ and $\text{Na}_1\text{V}_2(\text{PO}_4)_3$ powders followed by a heat treatment in Ar atmosphere according to the following chemical reaction:



Indeed, powders of these two end members ($y\text{Na}_3\text{V}_2(\text{PO}_4)_3 + (1-y)\text{Na}_1\text{V}_2(\text{PO}_4)_3$) were thoroughly mixed, pelletized and sealed in a gold tube in an Ar-filled glove box prior to annealing at 500–550 °C for 12 h. $\text{Na}_{1.5}\text{V}_2(\text{PO}_4)_3$ was obtained by chemical oxidation and deintercalation of 1.5 Na^+ ions from $\text{Na}_3\text{V}_2(\text{PO}_4)_3$ by adjusting precisely the concentration of NO_2BF_4 followed by a subsequent thermal treatment at 550 °C. Temperature-controlled in situ XRD patterns of mixtures of the precursors according to $y\text{Na}_3\text{V}_2(\text{PO}_4)_3 + (1-y)\text{Na}_1\text{V}_2(\text{PO}_4)_3$ ($0.25 \leq y \leq 0.75$) are given in Supplementary Fig. 1a–e, with $y = 0.25, 0.375, 0.5, 0.625$ and 0.75.

Chemical analysis

The carbon content within the carbon-coated $\text{Na}_3\text{V}_2(\text{PO}_4)_3$ powder was determined by thermogravimetric analysis combined with mass spectroscopy (using a NETZSCH STA 449 C) heated to 680 °C at a heating rate of 10 °C min⁻¹ (Supplementary Fig. 3). The morphology of the powder was investigated by scanning electron microscopy with a Hitachi Model S-4500 microscope. The chemical compositions of the $\text{Na}_x\text{V}_2(\text{PO}_4)_3$ powders were controlled using inductively coupled plasma optical emission spectroscopy with a Varian model 720-ES spectrometer after the samples were dissolved in concentrated HCl solution under heating.

X-ray diffraction

Temperature-controlled in situ SXRD measurements were performed using a 0.5-mm-diameter capillary in transmission mode (Debye–Scherrer geometry), at a wavelength of 0.95289 Å at the MSPD beamline of the ALBA Synchrotron, Spain. The SXRD patterns were collected during heating/cooling ramps of 5 °C min⁻¹. On-the-fly data were collected for 20 s each so that a pattern was collected every ~3 °C. Every 50 °C, a longer acquisition of ~8 min was performed while keeping the temperature constant. The mixture of $\text{Na}_3\text{V}_2(\text{PO}_4)_3$ and $\text{Na}_1\text{V}_2(\text{PO}_4)_3$ in a molar ratio of 1:1 (that is, for $\text{Na}_x\text{V}_2(\text{PO}_4)_3$ with $x = 2$) was heated to 500 °C and then cooled to 35 °C. The formation of various $\text{Na}_x\text{V}_2(\text{PO}_4)_3$ compositions ($x = 1.75, 2, 2.25$ and 2.5) was also monitored by temperature-controlled XRD measurements with a laboratory bench X-ray $\text{Co K}\alpha_{1,2}$ radiation in reflection geometry (PANalytical X'Pert Pro). The XRD patterns were collected every 50 °C from 25 °C up to 500–550 °C (the sample being in a closed system filled with He gas), and then during cooling to 25 °C, with 1 h of acquisition for each pattern.

Electrochemical measurements

Electrochemical experiments were carried out with a half-cell configuration versus Na metal in a coin-cell set-up. Positive electrodes were made of the active material, carbon black (Alfa Aesar, 99.9+%) and polyvinylidene difluoride, with a weight ratio of 73:18:9 and with a mass loading of 6–8 mg cm⁻². One Celgard and one Whatman glass fibre (grade GF/D) sheets were used as separators, and the electrolyte was 1 M NaPF_6 in a mixture of ethylene-carbonate/dimethyl-carbonate (1:1, w/w) with 2 wt% of fluoroethylene carbonate. Battery cells were operated at a rate of C/10 (corresponding to the exchange of one Na^+ and one electron in 10 h) in the voltage window of 2.5–4.3 V versus Na^+/Na .

Operando X-ray diffraction

Operando XRD measurements were performed using an in situ cell (equipped with a beryllium window) placed in a PANalytical Empyrean diffractometer using $\text{Cu K}\alpha_{1,2}$ radiation in reflection mode. Each XRD pattern was collected with an acquisition time of 1 h in the 2 θ angular range of 12–40°, with a 2 θ step size of 0.0167°. The working electrodes were composed of the chemically prepared $\text{Na}_2\text{V}_2(\text{PO}_4)_3$ powder mixed with carbon black (80/20 in wt%), and Na metal was used as the counter electrode. Two different voltage regions were investigated, 2.5–4.4 V and 1.3–3.0 V versus Na^+/Na , at a rate of C/10 (one Na per formula unit within 10 h). The analysis of the XRD data was performed using the Rietveld method with FullProf Suite software. Note that operando measurements were done with a laboratory X-ray set-up in Bragg Brentano geometry (reflection), using an in situ cell with a Be window protected with an Al foil. Consequently, the intensities of the diffraction peaks at low 2 θ angles are substantially affected by absorption (of Be and of the sample itself) but can be mathematically corrected based on the mass attenuation coefficient. The XRD patterns of $\text{Na}_2\text{V}_2(\text{PO}_4)_3$ collected from SXRD, from lab XRD with a standard holder, from lab XRD in an in situ cell and before and after the intensity correction are compared in Supplementary Fig. 4. The results of the Rietveld refinements are compared in Supplementary Table 1. A detailed procedure for the correction of the intensities is given in the Supplementary Information. Despite this correction, the intensity of the (012) reflection peak recorded at a low angle ($Q = 0.017 \text{ \AA}^{-1}$) in an in situ cell remains lower than expected, thus affecting the values of the occupancy factors determined for the Na(1) and Na(2) sites by Rietveld refinements.

Computational methodology

In our prior theoretical work^{16,34}, we developed a first-principles multi-scale model, combining a cluster expansion formalism parameterized on DFT-computed Na-vacancy configurations with Monte Carlo simulations, to investigate phase behaviours and Na^+ transport of $\text{Na}_x\text{V}_2(\text{PO}_4)_3$ positive electrode material during Na (de)intercalation (Supplementary Fig. 5). With the accuracy of first-principles DFT calculations

in the strongly constrained and appropriately normed (SCAN) level of theory⁵⁴, we investigated the solubility of Na over a wide range of sodium compositions (that is, $1 \leq x \leq 4$). We considered a large number of Na-vacancy configurations (850 in total). A comprehensive temperature versus composition phase diagram of $\text{Na}_x\text{V}_2(\text{PO}_4)_3$ was derived. A close inspection of our DFT-computed structures at $\text{Na}_1\text{V}_2(\text{PO}_4)_3$, $\text{Na}_{1.5}\text{V}_2(\text{PO}_4)_3$ and $\text{Na}_2\text{V}_2(\text{PO}_4)_3$ results in ground state and metastable compositions, which are characterized by fully occupied Na(1) sites and partially occupied Na(1) sites, respectively. The corresponding key properties (that is, relative energies above the ground state, volume and Na(1) and Na(2) occupations) can be generated by DFT fully structural relaxations, as summarized in Table 1.

Data availability

Experimental data for Figs. 1–5 are available via Nextcloud at <https://extra.u-picardie.fr/nextcloud/index.php/s/tSZagY99WdkDnzY>. The results of the electronic structure calculations and other simulations reported in this work are freely available via Zenodo at <https://zenodo.org/records/13357637> (ref. 55). Source data are provided with this paper.

References

54. Sun, J., Ruzsinszky, A. & Perdew, J. Strongly constrained and appropriately normed semilocal density functional. *Phys. Rev. Lett.* **115**, 036402 (2015).
55. Wang, Z. & Canepa, P. caneparesearch/paper_NM23072487B_NVPsolidsolution: V1. Zenodo <https://doi.org/10.5281/zenodo.13357637> (2024).

Acknowledgements

We acknowledge C. Denage and E. Lebraud from the Institut de Chimie de la Matière Condensée de Bordeaux (ICMCB) for their support to prepare chemical and XRD experiments, as well as ALBA (Barcelona, Spain) for SXRD experiments on the MSPD beamline (proposal number 2002421208). We are also grateful to the Agence Nationale de la Recherche (ANR) and TIAMAT for the funding (CIFRE grant) of S. Park's PhD thesis. We thank the European Union's Horizon 2020 research and innovation programme under Marie

Sklodowska-Curie grant agreement no. 945357 for funding part of K. Choudhary's PhD thesis, and the Région Nouvelle-Aquitaine and the French National Research Agency (STORE-EX Labex Project ANR-10-LABX-76-01) for the partial financial support of this research. P.C. acknowledges funding from the National Research Foundation under NRF Fellowship NRFF12-2020-0012. P.C., Z.W., C.M. and J.-N.C. are grateful to the ANR-NRF for the funding of the NRF2019-NRF-ANR073 Na-MASTER project.

Author contributions

The initial project of this work was conceived by L.C., C.M., J.-N.C. and P.C. Most of the experimental work was performed by S.P. and K.C., supervised by J.-N.C., D.C., L.C., F.F. and C.M. Most of the computational work was performed by Z.W., supervised by P.C. The initial draft of the manuscript was written by S.P., and all the authors contributed heavily to the discussion and final version of this manuscript. All authors were consulted and gave their written approval on the present contribution statement.

Competing interests

The authors declare no competing interests.

Additional information

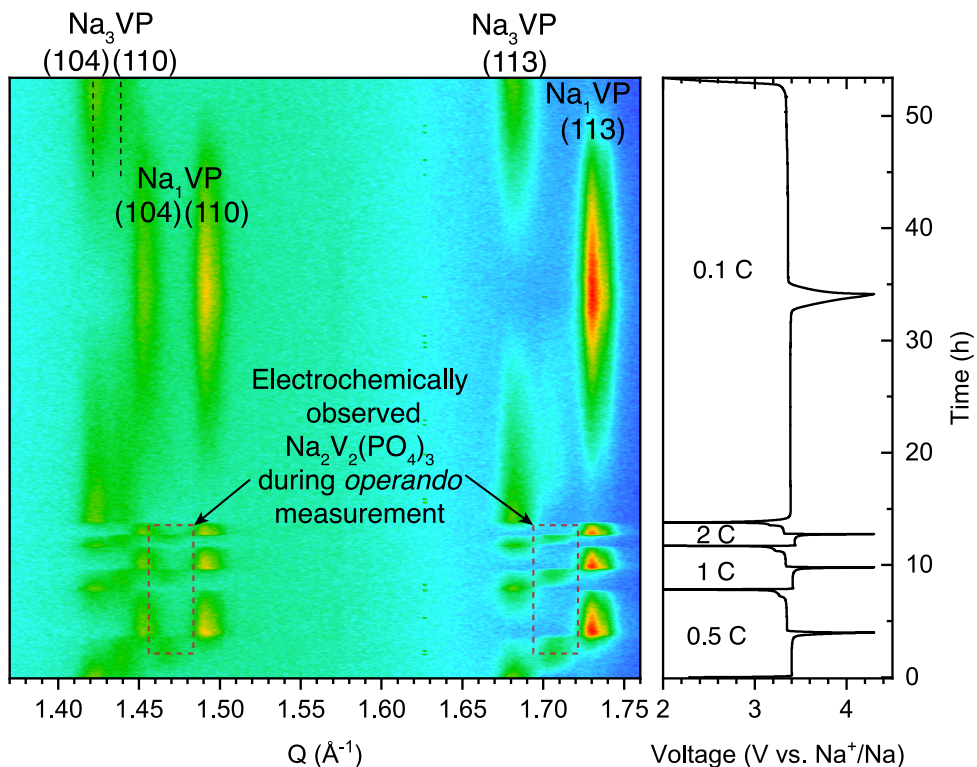
Extended data is available for this paper at <https://doi.org/10.1038/s41563-024-02023-7>.

Supplementary information The online version contains supplementary material available at <https://doi.org/10.1038/s41563-024-02023-7>.

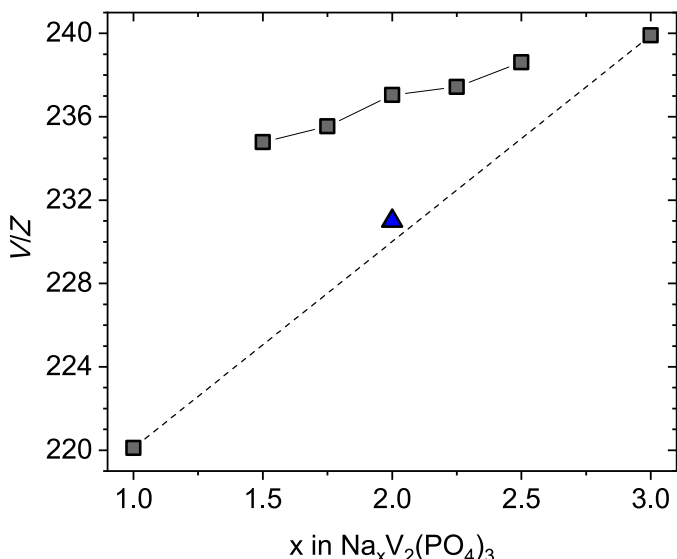
Correspondence and requests for materials should be addressed to Pieremanuele Canepa, Laurence Croguennec or Christian Masquelier.

Peer review information *Nature Materials* thanks Shinichi Komaba and the other, anonymous, reviewer(s) for their contribution to the peer review of this work.

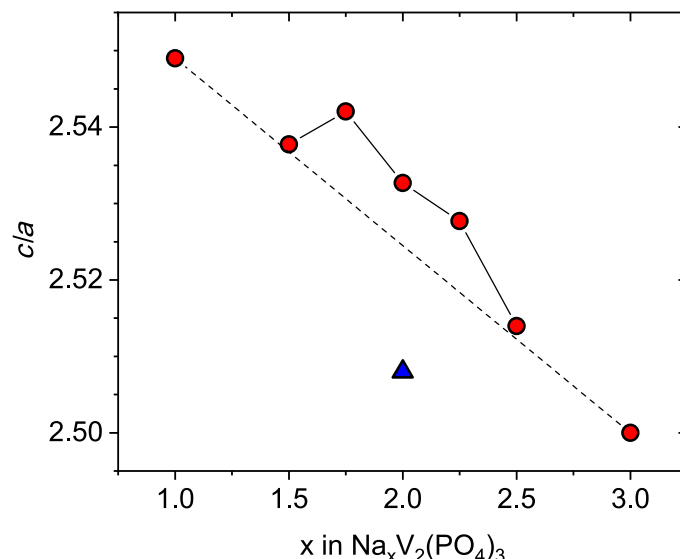
Reprints and permissions information is available at www.nature.com/reprints.



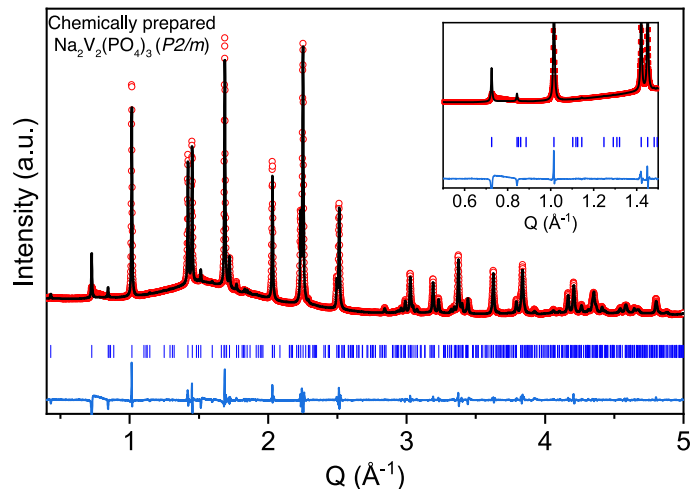
Extended Data Fig. 1 | Observation of the intermediate $\text{Na}_2\text{V}_2(\text{PO}_4)_3$ (Na_2VP) phase during battery operation. *Operando* XRD measurements using pristine $\text{Na}_3\text{V}_2(\text{PO}_4)_3$ as a positive electrode in a half cell versus Na metal. Voltage window of 2.0 – 4.3 V vs. Na^+/Na at cycling rates of C/10, C/2, 1 C and 2 C.



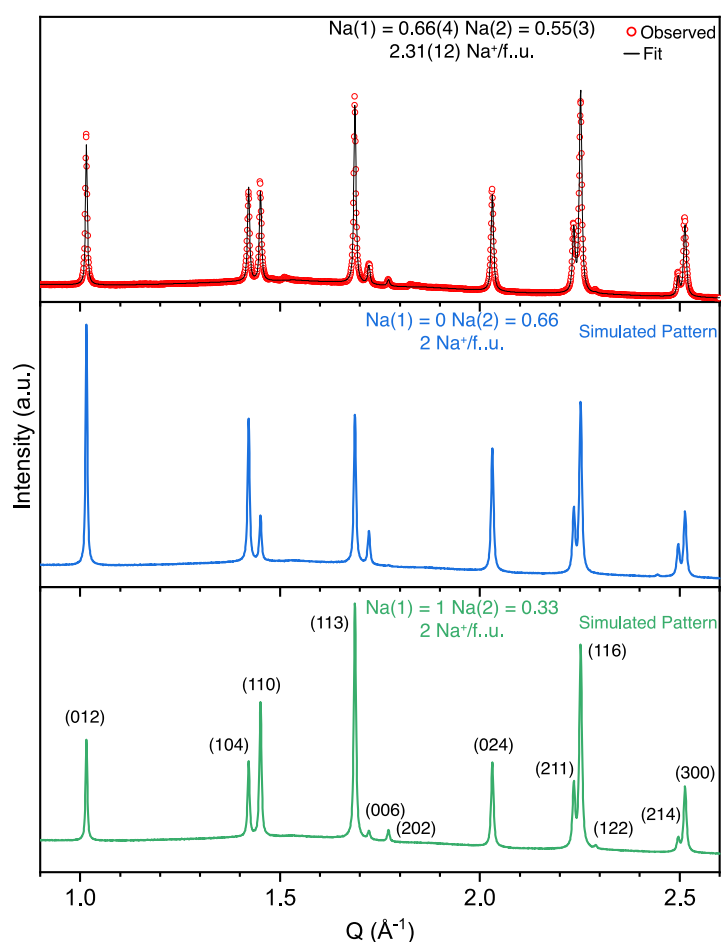
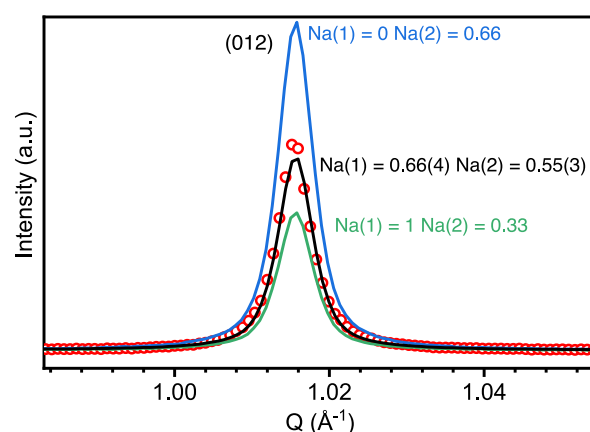
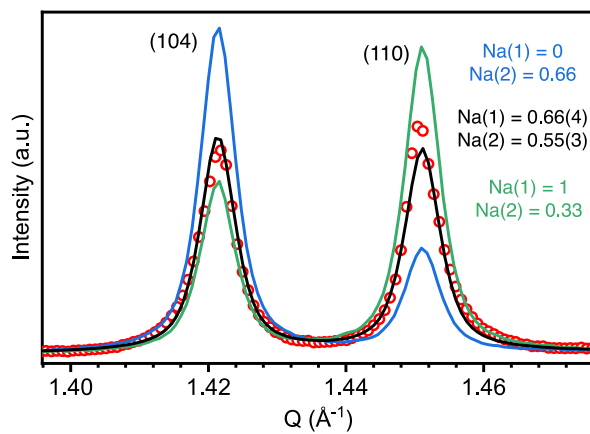
Extended Data Fig. 2 | Structural evolution of $\text{Na}_x\text{V}_2(\text{PO}_4)_3$. Unit cell volumes per formula unit (V/Z) and c/a ratios determined for chemically synthesized c- $\text{Na}_x\text{V}_2(\text{PO}_4)_3$ compositions at 25 °C, as a function of the Na_x content ($1 < x < 3$), and compared to those of $\text{Na}_3\text{V}_2(\text{PO}_4)_3$ and $\text{Na}_1\text{V}_2(\text{PO}_4)_3$. Note that the c- $\text{Na}_x\text{V}_2(\text{PO}_4)_3$ phases were prepared by annealing the mixtures of the



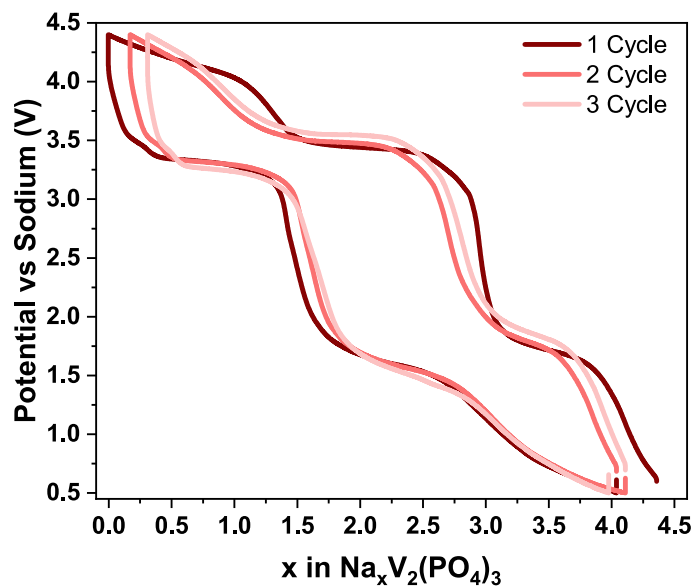
two end-members, $\text{Na}_3\text{V}_2(\text{PO}_4)_3$ and $\text{Na}_1\text{V}_2(\text{PO}_4)_3$, with the appropriate molar ratios. The e- $\text{Na}_2\text{V}_2(\text{PO}_4)_3$ phase electrochemically observed during *operando* is marked with blue triangle. The standard deviation on each calculated value is smaller than the size of the symbol (black square or red circle). The dashed lines joining the end members' compositions are guides for the eye.



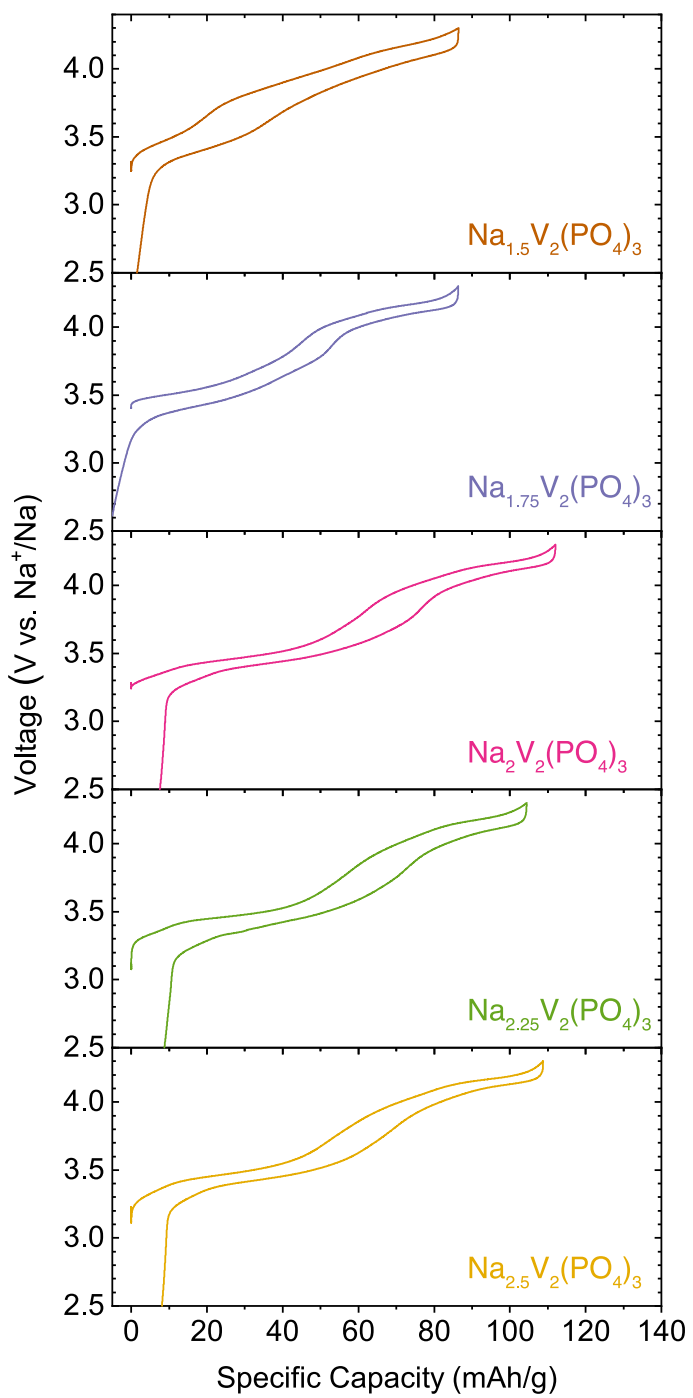
Extended Data Fig. 3 | Synchrotron XRD pattern of c- $\text{Na}_2\text{V}_2(\text{PO}_4)_3$. SXRD patterns of chemically prepared c- $\text{Na}_2\text{V}_2(\text{PO}_4)_3$ refined using a less symmetrical system ($P2/m$ space group), indicating that the diffraction peaks at 0.65 - 0.9 in Qspace are better explained.

a**b****c**

Extended Data Fig. 4 | Simulations of occupancy factors of Na(1) and Na(2) sites of c-Na₂V₂(PO₄)₃. (a) SXRD pattern of the chemically prepared c-Na₂V₂(PO₄)₃ with the refined results using R-3c space group, simulated SXRD patterns with Na(1) = 0, and Na(2) = 0.66 (blue), and Na(1) = 1, and Na(2) = 0.33 (green). Enlarged reflection peaks of (012) plane (b), and (104), (110) planes (c).



Extended Data Fig. 5 | The electrochemical cyclings of $\text{Na}_x\text{V}_2(\text{PO}_4)_3$ cathode. Global utilization of the $\text{Na}_x\text{V}_2(\text{PO}_4)_3$ framework with $0 \leq x \leq 4$, after the first discharge from OCV down to 0.5 V vs. Na^+/Na . Reminder, the first discharge voltage curve is omitted, and hence the first cycle started with charging process from $\text{Na}_4\text{V}_2(\text{PO}_4)_3$.



Extended Data Fig. 6 | Electrochemical (dis)charge profiles of the chemically synthesized $\text{Na}_x\text{V}_2(\text{PO}_4)_3$ cathodes. Electrochemical charge and discharge profiles of the chemically prepared c- $\text{Na}_x\text{V}_2(\text{PO}_4)_3$ ($x = 1.5, 1.75, 2, 2.25, 2.5$) electrode materials cycled between 2.5 and 4.3 V at C/10 (1 Na^+ in 10 h) versus Na metal.

Extended Data Table 1 | Unit cell parameters, V/Z values, Na site occupancy factors, and average V-O distances determined from the Rietveld refinement of the electrochemically-observed $\text{Na}_2\text{V}_2(\text{PO}_4)_3$ and the chemically-prepared $\text{Na}_2\text{V}_2(\text{PO}_4)_3$. Note that the electrochemically-observed $\text{Na}_2\text{V}_2(\text{PO}_4)_3$ is described in both $P2_1/c$ and $R-3c$ space groups for comparison purposes. Note that the stoichiometry ratio obtained from ICP results for the chemically-prepared $\text{Na}_2\text{V}_2(\text{PO}_4)_3$ is $\text{Na}_{2.08(4)}\text{V}_{2.02(1)}(\text{PO}_4)_3$

	S.G.	a (Å)	b (Å)	c (Å)	c/a	β (°)	V/Z (Å ³)	Na(1) Occ.	Na(2) Occ.	Total Na /f.u.	V-O (Å)
Electrochemically-observed $e\text{-Na}_2\text{V}_2(\text{PO}_4)_3$	$P2_1/c$	15.2377(5)	8.6082(5)	8.7391(4)	–	126.281(3)	231.02(2)	0.98(4)	0.363(6)	2.1(3)	1.99(9) / 2.00(9)
	$R-3c$	8.6096(2)	8.6096(2)	21.5910(8)	2.508	120	231.003(13)	0.98(5)	0.33(2)	1.94(12)	1.98(2)
Chemically-prepared $c\text{-Na}_2\text{V}_2(\text{PO}_4)_3$	$R-3c$	8.6599(2)	8.6599(2)	21.8882(6)	2.528	120	236.929(13)	0.66(4)	0.55(3)	2.31(12)	2.001(7)

Extended Data Table 2 | Unit cell parameters, V/Z values, Na site occupancy factors and average V-O distances determined from the Rietveld refinement of the XRD patterns collected *operando* during Na deintercalation from chemically-prepared c-Na₂V₂(PO₄)₃. Comparison with those obtained for chemically deintercalated Na₂V₂(PO₄)₃. *Refined and fixed at the last stages of refinement. Note that the stoichiometry ratio obtained from ICP results for the Na₂V₂(PO₄)₃ after the chemical de-sodiation process is Na_{0.25(5)}V_{1.99(1)}(PO₄)₃

	<i>a</i> (Å)	<i>c</i> (Å)	<i>c/a</i>	<i>V/Z</i> (Å ³)	Na(1) Occ.	Na(2) Occ.	Total Na /f.u.	V-O (Å)
Pristine	8.6497(4)	21.8865(14)	2.530	236.35(2)	0.70(6)	0.49(2)	2.18(12)	2.001(7)
Charged at 3.8 V	8.5383(3)	21.7706(16)	2.551	229.08(2)	0.85(4)	0.08(2)	1.09(9)	1.97(3)
Charged at 4.4 V	8.4732(3)	21.5117(15)	2.487	222.92(2)	0.46(4)	0.03(2)	0.55(11)	1.92(3)
Chemically deintercalated	8.4583(2)	21.6842(14)	2.507	223.92(12)	0.00(3)	0*	0.00(3)	1.89(15)
Discharged 3.9 V	8.5182(3)	21.7338(17)	2.551	227.62(2)	0.92(4)	0.04(3)	1.03(14)	1.97(3)
Discharged 2.5 V	8.6516(3)	21.8716(13)	2.528	236.29(2)	0.66(5)	0.54(2)	2.29(11)	2.03(3)

Extended Data Table 3 | Refined structural parameters of chemically deintercalated phase from the $\text{Na}_2\text{V}_2(\text{PO}_4)_3$ powder collected within a capillary at 298 K. *Refined and fixed at the last stages of refinement

$\text{Na}_0\text{V}_2(\text{PO}_4)_3$
 Space group: $R-3c$ (#167); $Z = 6$
 $a = 8.4583(2)$ Å; $c = 21.6842(9)$ Å; $c/a = 2.507$
 $V = 1343.52(7)$ Å³; $V/Z = 223.920(12)$ Å³
 $R_{\text{wp}} = 11.0\%$; $R_{\text{p}} = 14.6\%$; $R_{\text{Bragg}} = 5.11\%$

Atom	Wyckoff position	x/a	y/b	z/c	Uiso, Å ²	Occ.
V(1)	12c	0	0	0.1451(3)	0.034(2)	1
P(1)	18e	0.2698(12)	0	0.25	0.091(5)	1
Na(1)	6b	0	0	0	0.074*	0.00(3)
Na(2)	18e	0.6420(13)	0	0.25	0.120*	0*
O(1)	36f	0.0241(16)	0.1929(15)	0.1911(6)	0.033(5)	1
O(2)	36f	0.1937(15)	0.1611(17)	0.0890(10)	0.120(6)	1

Kinetic Monte Carlo Simulations of Sodium Ion Transport in NaSICON Electrodes

Ziliang Wang, Tara P. Mishra, Weihang Xie, Zeyu Deng, Gopalakrishnan Sai Gautam, Anthony K. Cheetham, and Pieremanuele Canepa*



Cite This: *ACS Materials Lett.* 2023, 5, 2499–2507



Read Online

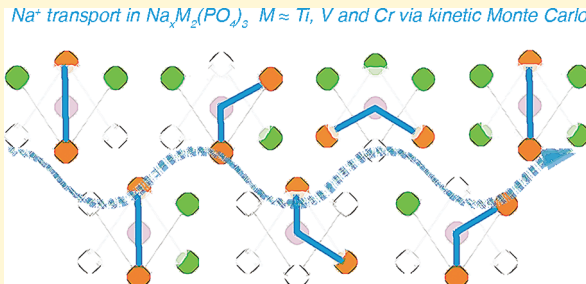
ACCESS |

Metrics & More

Article Recommendations

Supporting Information

ABSTRACT: The development of high-performance sodium (Na) ion batteries requires improved electrode materials. The energy and power densities of Na superionic conductor (NaSICON) electrode materials are promising for large-scale energy storage applications. However, several practical issues limit the full utilization of the theoretical energy densities of the NaSICON electrodes. A pressing challenge lies in the limited sodium extraction in low Na content NaSICONs, e.g., $\text{Na}_1\text{V}^{\text{IV}}\text{V}^{\text{IV}}(\text{PO}_4)_3 \leftrightarrow \text{V}^{\text{V}}\text{V}^{\text{IV}}(\text{PO}_4)_3 + \text{e}^- + \text{Na}^+$. Therefore, it is important to quantify the Na-ion mobility in a broad range of NaSICON electrodes. Using a kinetic Monte Carlo approach bearing the accuracy of first-principles calculations, we elucidate the variability of Na-ion transport vs Na content in three important NaSICON electrode materials, $\text{Na}_x\text{Ti}_2(\text{PO}_4)_3$, $\text{Na}_x\text{V}_2(\text{PO}_4)_3$, and $\text{Na}_x\text{Cr}_2(\text{PO}_4)_3$. We show Na^+ transport in NaSICON electrode materials is almost entirely determined by the local electrostatic and chemical environment set by the transition metals and the polyanionic scaffold. The competition with the ordering-disordering phenomena of Na vacancies also plays a role in influencing Na transport. We identify the Na content providing the highest room-temperature diffusivities in these electrodes, i.e., $\text{Na}_{2.7}\text{Ti}_2(\text{PO}_4)_3$, $\text{Na}_{2.9}\text{V}_2(\text{PO}_4)_3$, and $\text{Na}_{2.6}\text{Cr}_2(\text{PO}_4)_3$. We link the variations in the Na^+ kinetic properties by analyzing the competition of ligand field stabilization transition metal ions and their ionic radii. We interpret the limited Na extraction at $x = 1$ observed experimentally by gaining insights into the local Na vacancy interplay. Targeted chemical substitutions of transition metals disrupting local charge arrangements will be critical to reducing the occurrence of strong Na^+ -vacancy orderings at low Na concentrations, thus expanding the accessible capacities of these electrode materials.



1. INTRODUCTION

Having achieved widespread commercialization, rechargeable lithium (Li)-ion batteries (LIBs) are now at the risk of geopolitically constrained supply chains of key raw materials, such as cobalt, nickel, and Li.^{1–3} Sodium (Na)-ion batteries (SIBs) appear to be promising alternatives to the LIB analogs, as Na-metal can be harvested directly from seawater.^{4–6} Extensive research is underway to optimize electrodes and electrolytes for SIBs.^{7–21} One of the material classes for NIBs is the polyanionic sodium superionic conductor (NaSICON), discovered by Hong et al.,^{22,23} a framework studied for its fast Na-conducting properties. Electrodes crystallizing in the NaSICON framework, with formula $\text{Na}_x\text{M}_2(\text{PO}_4)_3$ (where M = transition metal), can be highly tuned to achieve promising energy densities,^{10,14,24} by changing the ratio and types of transition metals in the NaSICON, such as $\text{Na}_x\text{TiV}(\text{PO}_4)_3$, $\text{Na}_x\text{TiMn}(\text{PO}_4)_3$, $\text{Na}_x\text{VMn}(\text{PO}_4)_3$, and $\text{Na}_x\text{CrMn}(\text{PO}_4)_3$.

For most NaSICON electrodes, the accessible capacity is significantly lower than the theoretical value, which is linked to difficulties in reversibly extracting the entire available Na

content. For example, in $\text{Na}_x\text{V}_2(\text{PO}_4)_3$, the reversible extraction of four sodium ions entails the utilization of all vanadium redox states ($\text{V}^{\text{V}}/\text{V}^{\text{IV}}$, $\text{V}^{\text{IV}}/\text{V}^{\text{III}}$, and $\text{V}^{\text{III}}/\text{V}^{\text{II}}$) with a theoretical gravimetric capacity of $\sim 235 \text{ mAh g}^{-1}$. In practice, only two sodium ions can be reversibly extracted from $\text{Na}_3\text{V}_2(\text{PO}_4)_3$ up to $\text{Na}_1\text{V}_2(\text{PO}_4)_3$.^{14,15,24–26} While Gopalakrishnan and Rangan suggested the possibility of chemically extracting the last Na^+ forming $\text{V}_2(\text{PO}_4)_3$,²⁷ successive endeavors have proven unsuccessful. Hence, understanding the factors that limit reversible Na extraction within NaSICONs and facilitating the same remains an active topic of research.

Received: June 7, 2023

Accepted: August 9, 2023

Published: August 14, 2023



In this Letter, using density functional theory (DFT) based kinetic Monte Carlo (kMC) simulations, we unveil the physical origins for the variation in Na^+ transport properties in three NaSICON electrode materials, namely, $\text{Na}_x\text{Ti}_2(\text{PO}_4)_3$, $\text{Na}_x\text{V}_2(\text{PO}_4)_3$, and $\text{Na}_x\text{Cr}_2(\text{PO}_4)_3$. Our analysis reveals the kinetic limits to reversibly extracting Na ions in these NaSICONs apart from identifying the Na-composition ranges to achieve a high Na^+ diffusivity. The macroscopic Na^+ transport is highly influenced by the interplay between Na-vacancy arrangements and transition metals. Our results shed light on the optimization of NaSICON electrodes for improved reversible capacities.

2. RESULTS

To investigate the Na^+ transport in $\text{Na}_x\text{Ti}_2(\text{PO}_4)_3$, $\text{Na}_x\text{V}_2(\text{PO}_4)_3$, and $\text{Na}_x\text{Cr}_2(\text{PO}_4)_3$, we rely on a combination of DFT calculations, constructing a cluster expansion Hamiltonian, and performing kinetic Monte Carlo simulations (*vide infra*).^{28,29} The ground-state structures representing specific Na-vacancy arrangements at different Na compositions of the $\text{Na}_x\text{Ti}_2(\text{PO}_4)_3$, $\text{Na}_x\text{V}_2(\text{PO}_4)_3$, and $\text{Na}_x\text{Cr}_2(\text{PO}_4)_3$ NaSICON were taken from refs 10 and 14. To estimate the Na^+ migration barriers in the three NaSICONs, we selected several sodium compositions, including $x = 1, 3$, and 4 in $\text{Na}_x\text{Ti}_2(\text{PO}_4)_3$; $x = 1, 2, 3$, and 4 in $\text{Na}_x\text{V}_2(\text{PO}_4)_3$; and $x = 1$ and 3 in $\text{Na}_x\text{Cr}_2(\text{PO}_4)_3$.

At $x = 1$ and 4 , all three NaSICONs crystallize in the rhombohedral space group ($\text{R}\bar{3}\text{c}$ or $\text{R}\bar{3}$). While $\text{Na}_4\text{Cr}_2(\text{PO}_4)_3$ is included for completeness in this investigation, it is not expected to be stable (due to the instability of Cr^{II} in the solid state³⁰) and has never been reported experimentally. $\text{Na}_3\text{M}_2(\text{PO}_4)_3$ configurations with monoclinic (Cc or $\text{C}2/c$) symmetry represent the compositions with the lowest formation energies in the $\text{Na}_x\text{M}_2(\text{PO}_4)_3$ pseudobinary tie line of all the three NaSICONs.^{10,14} Recent investigations predicted the mixed-valence $\text{Na}_2\text{V}_2(\text{PO}_4)_3$ as a thermodynamically stable phase.^{14,24}

Each Na-vacancy (Va) configuration at the above Na compositions was optimized using the strongly constrained and appropriately normed exchange and correlation functional within DFT.³¹ A Hubbard U correction (SCAN+ U) was applied, which has been confirmed to accurately predict the redox electrochemistry during Na (de)intercalation.^{14,29,30,32,33} We use the nudged elastic band (NEB) method to simulate the Na^+ migration barriers.³⁴

Typically, the migration mechanism of ions in fast conductors is ascribed to be a local property of the immediate chemical environment of the migrating species, which is strongly influenced by the local ion-vacancy configuration(s).^{28,29,35,36} Figure 1 shows the relevant local portion of the NaSICON structure—the migration unit (MU)—that is sufficient to capture the Na migration with variations in the local configurations of Na and vacancies. Figure 1a represents the general MU in $\text{Na}_x\text{M}_2(\text{PO}_4)_3$, where groups of corner-shared octahedra contain six Na(2) sites centered around a Na(1) site. For the sake of visualization, the MO_6 and the PO_4^{3-} groups are not shown. Within each MU octahedron, two Na(2) sites will be “active”, taking part in the $\text{Na}(2)\leftrightarrow\text{Na}(1)\leftrightarrow\text{Na}(2)$ migration event, whereas the remaining four Na(2) sites and/or vacancies will be “inactive” (Figure 1a) and spectating the process of Na migration. Herein, we consider a single Na migration hop $\text{Na}(2)\leftrightarrow\text{Na}(1)$ as the fundamental Na-ion migration event in a single MU.^{22,23,26,29,37,38}

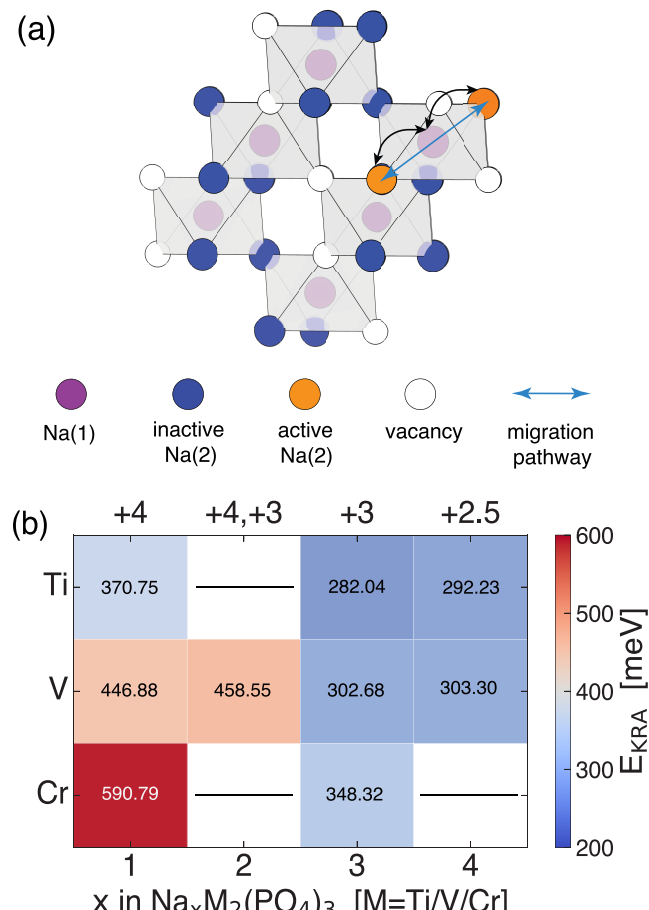


Figure 1. Model of Na^+ migration in the NaSICON $\text{Na}_x\text{M}_2(\text{PO}_4)_3$ identifying the migration unit (MU) and associated Na-ion migration barriers. (a) A representation of the Na-vacancy sublattice in NaSICON, illustrated by the corner-sharing octahedra. Two Wyckoff positions, the Na(1) (6b) sites, are shown by purple circles and the Na(2) (18e) sites by orange or blue circles, depending on the participation of the Na(2) site in a migration event. Empty circles denote vacancies. Each Na(1) site is surrounded by six nearest neighbor Na(2) sites. In each octahedron, two Na(2) sites participate in the Na-ion migration pathway (orange circles connected by blue line), whereas every single hop $\text{Na}(2)\leftrightarrow\text{Na}(1)$ is denoted by the black double-arrows. (b) Computed E_{KRA} 's for the migration event $\text{Na}(2)\leftrightarrow\text{Na}(1)$ in the MU (values are indicated in each box), with varied Na compositions (x) and transition metals (M). Black lines indicate compositions where migration barriers were not computed (see the main text). Na compositions are shown in the bottom x axis, and the formal oxidation states of the transition metals are in the top x axis.

The collective diffusion of Na ions in the NaSICON electrodes can be captured by our lattice model, which is composed of thousands of MUs, with different Na-vacancy orderings. Indeed, ensembles of MUs are used to tessellate periodically the $\text{Na}_x\text{M}_2(\text{PO}_4)_3$ structures in the composition range $1 \leq x \leq 4$. At intermediate compositions ($1 < x < 4$), a variety of MUs with different local Na vacancy arrangements is sufficient to approximate the migrating environments of the Na ions. The subsets of crystallographic sites of the migrating Na ions are fully encompassed by an ensemble of MUs incorporating all possible Na-vacancy occupation arrangements. Therefore, the partial occupations of Na sites as refined

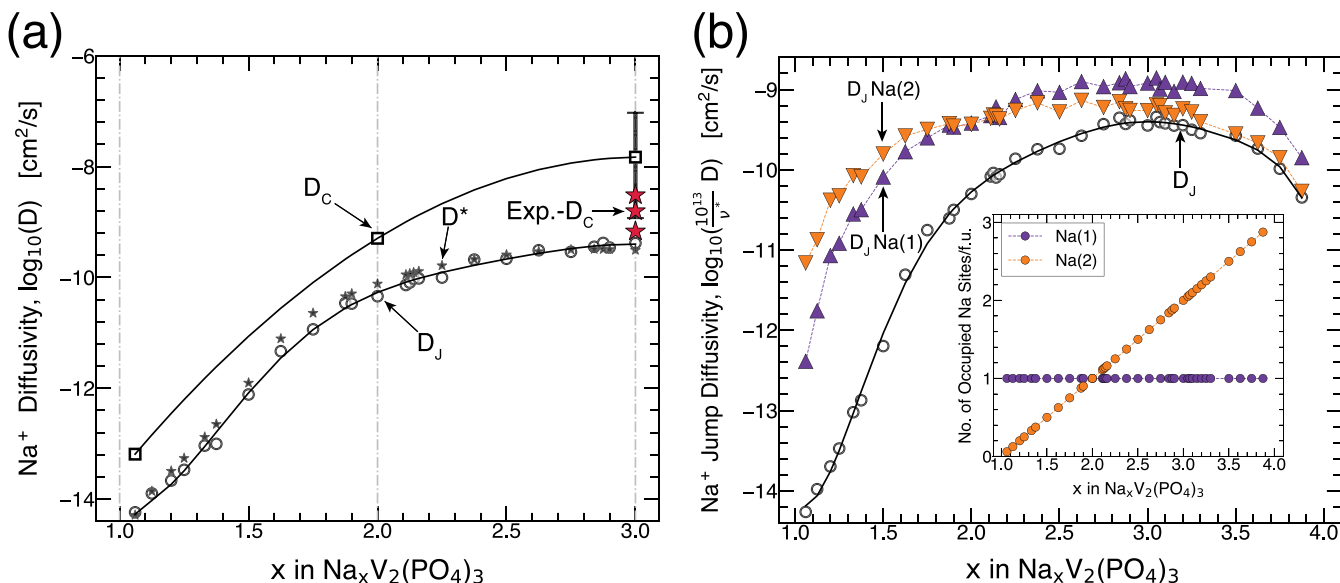


Figure 2. Predicted diffusivities of $\text{Na}_x\text{V}_2(\text{PO}_4)_3$ at 300 K. Panel a plots D_j (circles), D^* (stars), and D_c (squares). The pre-exponential factor is assumed as 1×10^{13} Hz.³⁵ Vertical lines represent the phase boundaries derived from the phase diagram at ~ 300 K.¹⁴ Values of D_c are only in the single-phase regions, i.e., $x = 1, 2$, and 3 . At intermediate compositions (two-phase regions), the thermodynamic factor $\Theta = 0$ leads to zero D_c . In the two-phase regions, D_c is approximated using Vegard's law. The standard deviation of our predictions is shown at $x = 3.0$. Solid lines in black are the polynomial model fitted on the predictions. The experimental values of chemical diffusivity ($\text{exp.}-D_c$, red stars) are from ref 47 at $x = 3$. Panel b plots D_j (black circles), $D_j\text{Na}(1)$, which arises from the $\text{Na}(1)$ -ion movement (purple triangles), and $D_j\text{Na}(2)$ from the $\text{Na}(2)$ -ion movement (orange triangles). In panel b, all D_j 's are renormalized with a $10^{13}/\nu^*$ factor, due to the uncertainty in the prefactor ν^* .^{35,48} The inset shows the computed occupation number of $\text{Na}(1)$ (in purple) and $\text{Na}(2)$ (in yellow) sites per formula unit vs. x extracted from the kMC simulations at 300 K.

from experimental techniques, such as X-ray diffraction,^{14,24,39,40} can be described by the 3D networks formed by thousands of MUs.

Based on the assumption that the transport property relies mainly on the local Na-vacancy orderings, all possible migration pathways within the MUs were extensively simulated using the NEB method combined with SCAN+U calculations. The computed migration barriers are reported in Section 1 of the Supporting Information (SI). We did not evaluate the migration energy of Na^+ at $x = 2$ in $\text{Na}_x\text{Ti}_2(\text{PO}_4)_3$ and $\text{Na}_x\text{Cr}_2(\text{PO}_4)_3$, as well as at $x = 4$ in $\text{Na}_x\text{Cr}_2(\text{PO}_4)_3$, since they have not been reported experimentally.

The computed migration barrier (E_{barrier}) results are in good agreement with prior computational and experimental studies (see section 1 of the SI). For example, for $\text{Na}_3\text{Cr}_2(\text{PO}_4)_3$, the $E_{\text{barrier}} \sim 621$ meV agrees well with the ~ 620 meV experimental value for the α phase of the same system.¹⁶ Similarly, for $\text{Na}_3\text{V}_2(\text{PO}_4)_3$, we predict an $E_{\text{barrier}} \sim 455$ meV, which is comparable with the range of values 353–513 meV computed with the HSE06 functional.⁴¹ In the case of $\text{Na}_3\text{Ti}_2(\text{PO}_4)_3$, the predicted $E_{\text{barrier}} \sim 530$ meV underestimates the experimental value of ~ 750 meV from ref 39.

The directional dependence of E_{barrier} is removed by using the kinetically resolved activation barriers (E_{KRA}), as defined in ref 35. Low values of E_{KRA} correspond to low migration barriers and vice versa. The computed E_{KRA} values of Na^+ migration events of the type $\text{Na}(2) \leftrightarrow \text{Na}(1)$ of an MU that best represents the ground state configurations at different x are shown in Figure 1b. The lowest values of E_{KRA} are calculated at compositions $\text{Na}_3\text{M}_2(\text{PO}_4)_3$ and follow the order $\text{Ti} \sim 282$ meV < $\text{V} \sim 303$ meV < $\text{Cr} \sim 348$ meV. In contrast, the maximum E_{KRA} values are observed at $x \sim 1$, in agreement with existing reports.^{16,26,39} The barriers at $x = 3$ across the

different NaSICONs follow the ligand field stabilization energies (LFSE) for $\text{Ti}^{\text{III}}(d^1) < \text{V}^{\text{III}}(d^2) < \text{Cr}^{\text{III}}(d^3)$, and the decreasing order of the transition metal sizes.^{42,43} Note that LFSE also correlates with the NaSICON pseudobinary formation energies $\text{Na}_3\text{Cr}_2(\text{PO}_4)_3 \gg \text{Na}_3\text{V}_2(\text{PO}_4)_3 > \text{Na}_3\text{Ti}_2(\text{PO}_4)_3$, thus increasing the Na migration barriers in the same order.¹⁰

Starting from the computed E_{KRA} encompassing several Na-vacancy arrangements in the MU (see section 2 of the SI), a local cluster expansion (LCE) Hamiltonian³⁵ was trained for each NaSICON system. We use the LCE together with our kinetic Monte Carlo simulation package⁴⁴ to investigate the Na^+ transport within the NaSICON structures (see sections 2 and 3 in the SI), by performing long-time (on the order of milliseconds) and large-scale ($8 \times 8 \times 8$ formula units corresponding to 4096 Na sites) simulations. The LCE Hamiltonian could investigate Na^+ benchmarked on barriers obtained from first-principles calculations. The accuracy of predicted E_{KRA} 's, obtained from the LCE formalism is bound within root mean square (RMS) errors of ± 31.75 meV for $\text{Na}_x\text{V}_2(\text{PO}_4)_3$, ± 25.29 meV for $\text{Na}_x\text{Ti}_2(\text{PO}_4)_3$, and ± 35.81 meV for $\text{Na}_x\text{Cr}_2(\text{PO}_4)_3$ (see section 2 in the SI), which are within the perceived accuracy of migration barriers computed from first principles (± 50 meV).⁴⁵

By tracking all possible Na migration events of each NaSICON, we simulated the Na^+ diffusion, quantified by (i) the jump diffusivity (D_j), (ii) the tracer diffusivity (D^*), and (iii) the chemical diffusivity (D_c).³⁶ From the temperature vs composition phase diagrams of these NaSICON systems,¹⁴ using canonical Monte Carlo simulations, 1850 initial Na-vacancy configurations for each system (50 different configurations at 37 unique Na compositions) with specific Na-vacancy arrangements were generated at ~ 973 K, which is

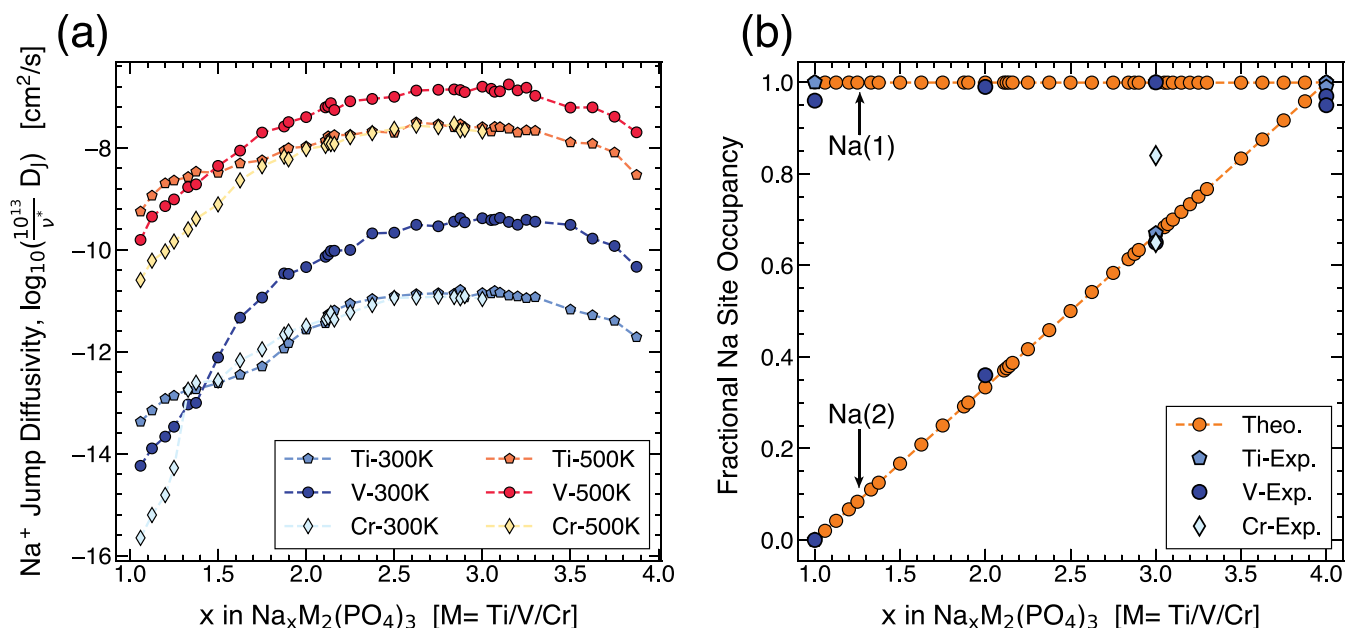


Figure 3. Computed Na^+ D_J at 300 and 500 K (panel a) and fractional occupancy at 300 K (panel b) of $\text{Na}(1)$ and $\text{Na}(2)$ sites in $\text{Na}_x\text{M}_2(\text{PO}_4)_3$ ($\text{M} = \text{Ti}, \text{V}$, or Cr). Due to the uncertainty in the prefactor ν^* , all D_J values are normalized using a $10^{13}/\nu^*$ factor. In panel a, data at 300 and 500 K are shown in blue and red/yellow symbols. For $\text{Na}_x\text{Cr}_2(\text{PO}_4)_3$, Na extraction can only occur for $1 \leq x \leq 3$.¹⁷ The computed results (Theo.) in panel b are denoted by orange circles, with experimental values in blue shapes.^{15,18,24,52,53} The computed Na-site occupancy does not show significant differences among the three NaSICONs within our predictions; hence, data for $\text{Na}_x\text{V}_2(\text{PO}_4)_3$ is plotted in panel b.

the typical synthesis temperature of these NaSICONs. Thus, these model structures mimic Na-vacancy configurations that are obtained postsynthesis^{17,22–24,26,46} and are used in the kMC simulations as starting configurations. Subsequently, we performed 500 equilibration sweeps: one sweep is the total number of Na-vacancy sites in the simulation model, i.e., 4096 followed by 3000 kMC sampling sweeps of each configuration and statistically averaged the transport properties over a wide temperature range (300 to 900 K, see section 3 of the SI).

We used $\text{Na}_x\text{V}_2(\text{PO}_4)_3$ to discuss the behavior of the diffusion coefficients predicted by our kMC simulations. Figure 2a shows the computed D_J , D^* , and D_C values for $\text{Na}_x\text{V}_2(\text{PO}_4)_3$ at 300 K as a function of x .

We derived the D_J by tracking the center-of-mass of all of the migrating Na^+ species, including the cross-correlations between different Na ions, which are excluded in the tracer diffusivity D^* . For this reason, in Figure 2a, D_J and D^* are different, but of similar magnitude, highlighting minimal contributions from cross-correlations, similar to observations in other electrode materials.³⁵ From the statistical analysis of the computed diffusivities, we derived a standard deviation (Figure 2a) of approximately ± 1 order of magnitude (± 120 meV in terms of E_{barrier}).⁴⁵

In $\text{Na}_x\text{V}_2(\text{PO}_4)_3$, the Na^+ jump diffusivities of Figure 2a increase progressively from low Na content ($\sim 5.77 \times 10^{-15}$ cm² s⁻¹ at $x \sim 1$) to high Na content ($\sim 4.16 \times 10^{-10}$ cm² s⁻¹ at $x = 3.0$). Diffusivities for $\text{Na}_3\text{V}_2(\text{PO}_4)_3$ are in good agreement with existing measurements.^{26,38,49}

We derive a fourth order polynomial fit for the monotonically increasing D_J across $1 \leq x \leq 3$, namely, $D_J(x) = C + E_1x + E_2x^2 + E_3x^3 + E_4x^4$ (black line in Figure 2). The coefficients of the fit E_1 , E_2 , E_3 , and E_4 are reported in the SI. The fitted polynomial reflects the concentration dependence of D_J .

The chemical diffusivity D_C depends on the thermodynamic factor Θ , as per $D_C = D_J\Theta$; values of Θ are from ref 14. D_J and Θ contribute oppositely to D_C . As Θ is related to the gradient of the Na chemical potential (eq 13 in SI), Θ usually takes large values for highly ordered (stable) configurations (Supporting Figure 16 in the SI), increasing the D_C of the corresponding ordered phase. In contrast, low values of D_J are typically found in ordered phases due to a lack of accessible vacant sites controlled by strong ion-vacancy ordering interactions. In $\text{Na}_x\text{V}_2(\text{PO}_4)_3$, D_C is dominated by D_J , as denoted by the relatively low values of room temperature chemical diffusivity at $x = 1$ and 2 (instead of the large values as controlled by Θ).³⁵ Gray vertical lines in Figure 2a depict the phase boundaries for $\text{Na}_x\text{V}_2(\text{PO}_4)_3$ from ref 14 at 300 K. The predicted values of D_C at $\text{Na}_3\text{V}_2(\text{PO}_4)_3$ (1.18×10^{-9} to 9.35×10^{-8} cm² s⁻¹) are higher than the experimental values (4.59×10^{-10} to 2.0×10^{-9} cm² s⁻¹) measured by electrochemical impedance spectroscopy (EIS).^{38,47}

While some experimental values of D_C ^{38,47} fall within the standard deviations of our predictions, other experimental studies have reported significantly different D_C values, such as 3×10^{-15} and 6×10^{-13} cm² s⁻¹ measured using the galvanostatic intermittent titration technique (GITT),⁵⁰ and 4×10^{-14} to 2.48×10^{-13} cm² s⁻¹ measured by EIS.⁵¹ Such large differences in experimental D_C values can be attributed to different synthesis procedures of $\text{Na}_3\text{V}_2(\text{PO}_4)_3$, which can affect the (im)purity of the particles, the particle sizes, and the defect concentrations, thus causing significant variations in transport properties.³⁸ Nevertheless, we expect our kMC simulations to yield an accurate value of D_C within bulk $\text{Na}_x\text{V}_2(\text{PO}_4)_3$ given that our confidence interval of calculated D_C is quite narrow.

The computed D_C for $\text{Na}_x\text{V}_2(\text{PO}_4)_3$ at 300, 700, and 900 K (Supporting Figure 17 of the SI) is superimposed on the

temperature–composition phase diagram,¹⁴ where the single-phase regions are always connected by dashed lines representing the two-phase regions. For all temperatures explored, we observe an increase in D_C in the composition range $1 \leq x \leq 3$. Unsurprisingly, the D_C values increase for increasing temperatures (i.e., at $x = 3$ from $1.48 \times 10^{-8} \text{ cm}^2 \text{ s}^{-1}$ at 300 K to $2.5 \times 10^{-3} \text{ cm}^2 \text{ s}^{-1}$ at 900 K), signifying high thermally activated motion of Na^+ .

Given the dominating contributions of D_J to the effective chemical diffusivity,³⁶ we can gain valuable insights about the jump diffusivity (D_J) of $\text{Na}_x\text{V}_2(\text{PO}_4)_3$ at 300 K by separating D_J into the specific contributions from each sodium site, i.e., $\text{Na}(1)$ and $\text{Na}(2)$ in Figure 2b. Here, we obtain $D_J\text{Na}(1)$ in the $\text{Na}_x\text{V}_2(\text{PO}_4)_3$ structure by tracking all unique Na^+ hopping events of the type $\text{Na}(1) \rightarrow \text{Na}(2)$, while we track $\text{Na}(2) \rightarrow \text{Na}(1)$ for $D_J\text{Na}(2)$. The differences between the overall D_J and individual $D_J\text{Na}(1)$ and $D_J\text{Na}(2)$ originate mainly from the number of the $\text{Na}(1)$ and $\text{Na}(2)$ sites available (see eqs 8, 9, and 10 in SI).

Values of $D_J\text{Na}(2)$ and $D_J\text{Na}(1)$ show similar magnitudes and appear higher than the overall D_J , especially in the composition range $1 \leq x \leq 3$. Both the $D_J\text{Na}(1)$ and $D_J\text{Na}(2)$ achieve their maxima at intermediate Na compositions, specifically $1.21 \times 10^{-9} \text{ cm}^2 \text{ s}^{-1}$ at $x \approx 2.94$ for $D_J\text{Na}(1)$ and $1.15 \times 10^{-9} \text{ cm}^2 \text{ s}^{-1}$ at $x \approx 2.71$ for $D_J\text{Na}(2)$. We observe a sharp decrease of Na diffusivity near $x \sim 1$, where values $D_J\text{Na}(2)$ and $D_J\text{Na}(1)$ are $6.91 \times 10^{-12} \text{ cm}^2 \text{ s}^{-1}$ and $4.11 \times 10^{-13} \text{ cm}^2 \text{ s}^{-1}$, respectively.

The number of occupied Na sites extracted from kMC simulations (inset of Figure 2b) agrees well with existing site occupations at 300 K from experiment and theory.^{14,24} $\text{Na}(1)$ sites (purple line) are always fully occupied in the range $1 \leq x \leq 3$, whereas the $\text{Na}(2)$ occupation (orange) varies from empty at $x = 1$ to fully occupied, with three $\text{Na}(2)$ sites per formula unit at $x = 4$. The number of occupied $\text{Na}(2)$ sites is much lower than that of $\text{Na}(1)$ at compositions around $x = 1$,¹⁴ reflecting the difference in stability of the two sites at $x = 1$, which results in boosting the $D_J\text{Na}(2)$ over $D_J\text{Na}(1)$. Effects of cross-correlations among Na ions distributed between $\text{Na}(1)$ and $\text{Na}(2)$ sites remain convoluted in the computed values of D_J .

We discuss the kMC predictions of two additional NaSICONs, $\text{Na}_x\text{Ti}_2(\text{PO}_4)_3$, and $\text{Na}_x\text{Cr}_2(\text{PO}_4)_3$, with similar electrochemical behavior to $\text{Na}_x\text{V}_2(\text{PO}_4)_3$.^{10,14–18} For $\text{Na}_x\text{Ti}_2(\text{PO}_4)_3$, the sodium composition ranges $1 \leq x \leq 3$ and $3 \leq x \leq 4$ are accessible electrochemically,^{10,18} whereas for $\text{Na}_x\text{Cr}_2(\text{PO}_4)_3$, Na extraction only occurs in $1 \leq x \leq 3$.^{10,17} Similar to $\text{Na}_x\text{V}_2(\text{PO}_4)_3$, $\text{Na}_x\text{Ti}_2(\text{PO}_4)_3$, and $\text{Na}_x\text{Cr}_2(\text{PO}_4)_3$ show single phases at $x = 1$ and $x = 3$.^{10,17,18,52,53} Figure 3a shows the computed D_J of $\text{Na}_x\text{V}_2(\text{PO}_4)_3$, $\text{Na}_x\text{Ti}_2(\text{PO}_4)_3$, and $\text{Na}_x\text{Cr}_2(\text{PO}_4)_3$ at 300 and 500 K.

For all systems, we observe an increase of D_J in the composition range $1 \leq x \leq 3$, followed by a gradual decrease of D_J for $3 < x \leq 4$ in $\text{Na}_x\text{Ti}_2(\text{PO}_4)_3$ and $\text{Na}_x\text{V}_2(\text{PO}_4)_3$. At 300 K, D_J reaches a maximum for all systems at $x \sim 3$, with $\text{Na}_x\text{V}_2(\text{PO}_4)_3$ displaying a higher magnitude of D_J in the range $1.5 \leq x \leq 4$ than $\text{Na}_x\text{Ti}_2(\text{PO}_4)_3$ and $\text{Na}_x\text{Cr}_2(\text{PO}_4)_3$. At 500 K, in comparison, the D_J values of all three NaSICONs were of a similar order of magnitude, corresponding intuitively to higher diffusion rates with increasing temperatures.

The maximum values of D_J occur at similar compositions for all NaSICONs, $4.09 \times 10^{-10} \text{ cm}^2 \text{ s}^{-1}$ for $\text{Na}_x\text{V}_2(\text{PO}_4)_3$ at $x \sim 2.9$, $1.71 \times 10^{-11} \text{ cm}^2 \text{ s}^{-1}$ for $\text{Na}_x\text{Ti}_2(\text{PO}_4)_3$ at $x \sim 2.7$, and

$1.39 \times 10^{-11} \text{ cm}^2 \text{ s}^{-1}$ for $\text{Na}_x\text{Cr}_2(\text{PO}_4)_3$ at $x \sim 2.6$, respectively. Similarly, the lowest values of D_J occur at a low Na content (i.e., $x \sim 1$) for all NaSICONs. For example, the lowest D_J among the NaSICONs at $x \sim 1$ is $2.2 \times 10^{-16} \text{ cm}^2 \text{ s}^{-1}$ for $\text{Na}_1\text{Cr}_2(\text{PO}_4)_3$. The low values of D_J at $x \sim 1$ suggest that the reversible extraction of the “last” Na ion from NaSICON electrodes may be limited also by the poor kinetics at low Na contents.

To understand the Na^+ distributions at 300 K, we extract the fractional occupancies of $\text{Na}(1)$ and $\text{Na}(2)$ sites (Figure 3b) and compare them with the experimental data of these NaSICON systems. At room temperature, we observe high stability of the $\text{Na}(1)$ site across the entire Na concentration range ($1 \leq x \leq 4$), where it remains fully occupied, while $\text{Na}(2)$ occupancy monotonically increases with increasing x . Our kMC results agree quantitatively with the experimentally refined $\text{Na}(1)/\text{Na}(2)$ occupations.^{15,18,24,52,53} In the case of $\text{Na}_3\text{Cr}_2(\text{PO}_4)_3$, the predicted occupation of $\text{Na}(1)$ (~ 1) overestimates the experimental data (~ 0.84), which suggests that the nominal composition may deviate from the real composition of synthesized NaSICONs.⁵³

3. DISCUSSION

In this Letter, using kMC simulations that bear the accuracy of DFT calculations, we investigated the variability of Na-ion transport vs Na content in three important NaSICON electrodes for Na-ion batteries: $\text{Na}_x\text{Ti}_2(\text{PO}_4)_3$, $\text{Na}_x\text{V}_2(\text{PO}_4)_3$, and $\text{Na}_x\text{Cr}_2(\text{PO}_4)_3$. We demonstrated that the ion transport properties (D_J , D^* , and D_C) of NaSICONs have a configurational dependence on the local sodium vacancy arrangements near the migration events.

In the three NaSICONs, we observed an increase of D_J from low Na concentrations of $x \sim 1$ to $x \sim 3$. For $\text{Na}_x\text{V}_2(\text{PO}_4)_3$ and $\text{Na}_x\text{Ti}_2(\text{PO}_4)_3$, we observed a decrease in D_J in the composition range $3 < x \leq 4$ (Figure 3a).

Interplay of Ligand Field Stabilization and Ionic Radii of Transition Metals. Two main factors: (i) the ligand field stabilization of transition metals and their (ii) ionic radii, can explain variations of migration barriers and diffusivities in these NaSICONs as a function of Na composition.

Different NaSICONs exhibit different migration barriers at the same Na content (see Figure 1b), with implications for the observed D_J . For example, at $x \sim 1$, the highest $E_{\text{KRA}} \sim 591$ meV is exhibited by $\text{Na}_1\text{Cr}_2(\text{PO}_4)_3$, well exceeding 447 meV in $\text{Na}_1\text{V}_2(\text{PO}_4)_3$, and 371 meV in $\text{Na}_1\text{Ti}_2(\text{PO}_4)_3$. Since at $x \sim 1$ all transition metals, Cr, Ti, and V, are tetra-valent (verified by the magnetic moments of Supporting Figure 7 in the SI), differences in migration energies in NaSICONs at this composition are controlled by the transition metal ionic radii, which will lead to different sizes of “bottlenecks” for the migrating Na ion.²⁴

At $x = 1$, the transition metal ionic radii follow the trend of $\text{Ti}^{\text{IV}} (\sim 0.61 \text{ \AA}) > \text{V}^{\text{IV}} (\sim 0.58 \text{ \AA}) > \text{Cr}^{\text{IV}} (\sim 0.55 \text{ \AA})$, which causes a similar variation in the lattice parameters.^{10,24,52} Thus, the sizes of the bottlenecks (i.e., the transition state) for the migrating Na^+ reduce in the order of $\text{Na}_1\text{Ti}_2(\text{PO}_4)_3 > \text{Na}_1\text{V}_2(\text{PO}_4)_3 > \text{Na}_1\text{Cr}_2(\text{PO}_4)_3$,²⁴ reflecting an identical trend in D_J values observed (see Figure 3a). Furthermore, the polyhedral volumes of transition-metal octahedra are $\sim 9.80 \text{ \AA}^3$ for TiO_6 , $\sim 9.33 \text{ \AA}^3$ for VO_6 , and $\sim 8.77 \text{ \AA}^3$ for CrO_6 . The bond distance between the migrating Na^+ at the transition state and nearby O^{2-} (which is linearly correlated with the migration barriers) follows a sequence of $\text{Na}_1\text{Ti}_2(\text{PO}_4)_3 (\sim 2.36 \text{ \AA}) >$

$\text{Na}_1\text{V}_2(\text{PO}_4)_3$ ($\sim 2.30 \text{ \AA}$) > $\text{Na}_1\text{Cr}_2(\text{PO}_4)_3$ ($\sim 2.27 \text{ \AA}$). This sequence indicates the narrower sizes of the migration “bottleneck” from $\text{Na}_1\text{Ti}_2(\text{PO}_4)_3$, via $\text{Na}_1\text{V}_2(\text{PO}_4)_3$, to $\text{Na}_1\text{Cr}_2(\text{PO}_4)_3$, hence explaining the reduced values of D_J in Figure 3a.

The impact of transition metal ionic radii is lower at a higher Na content (i.e., at $x \sim 3$), since the large ionic radius of Na^+ (when six-coordinated) dictates lattice parameters more significantly. Thus, variations observed in E_{barrier} and D_J are to be linked to the electronic structure (and LFSE) of the transition metals involved than to changes in lattice parameters or bottleneck sizes. Specifically, LFSE stabilizes Cr^{III} ($3d^3$) more than V^{IV} ($3d^2$; see Supporting Figure 8 in the SI), due to the high stability of the half-filled high-spin t_{2g} orbitals of Cr^{III} .¹⁰ A higher Na^+ E_{barrier} in $\text{Na}_3\text{Cr}_2(\text{PO}_4)_3$ compared to $\text{Na}_3\text{V}_2(\text{PO}_4)_3$ is expected as more energy is required to oxidize a Cr^{III} that is near a migrating Na^+ to Cr^{IV} , which is consistent with a lower value of D_J (Figure 3a) for $\text{Na}_3\text{Cr}_2(\text{PO}_4)_3$ than that for $\text{Na}_3\text{V}_2(\text{PO}_4)_3$.

In the case of $\text{Na}_3\text{Ti}_2(\text{PO}_4)_3$, Na^+ migration is penalized compared to $\text{Na}_3\text{V}_2(\text{PO}_4)_3$ since the highly stable configuration of $\text{Ti}^{\text{IV}}(3d^0)$ needs to be reduced by the migrating Na^+ to the unpreferred $\text{Ti}^{\text{III}}(3d^1)$ configuration. Thus, the energy cost associated with a local Ti reduction near a migrating Na causes the D_J for $\text{Na}_3\text{Ti}_2(\text{PO}_4)_3$ to be lower than $\text{Na}_3\text{V}_2(\text{PO}_4)_3$. In general, at composition $x > 2$, $\text{Na}_x\text{V}_2(\text{PO}_4)_3$ shows consistently higher D_J compared to $\text{Na}_x\text{Ti}_2(\text{PO}_4)_3$ and $\text{Na}_x\text{Cr}_2(\text{PO}_4)_3$ (Figure 3a).

Extracting the Last Na from $\text{Na}_1\text{M}_2(\text{PO}_4)_3$. From the occupation of Na sites (Figure 3b) at $x = 1$, we identified that only Na(1) sites were fully occupied, whereas Na(2) sites were empty. Such an arrangement of the Na ions relates to the “structural integrity” of $\text{Na}_1\text{M}_2(\text{PO}_4)_3$, where only Na(1) is occupied and screens the electrostatic repulsions of nearby MO_6 octahedra stacked along the c axis imparting stability to the $\text{Na}_1\text{M}_2(\text{PO}_4)_3$.^{24,54–56} Furthermore, we observed a large site energy difference ($\sim 880 \text{ meV}$) between the lower energy Na(1) site and Na(2) at $x \sim 1$ in $\text{Na}_1\text{V}_2(\text{PO}_4)_3$ (see Supporting Figure 2 of the SI). These results indicate that Na(2) sites are thermodynamically unstable at $x \sim 1$, which hinders the ion transport in $\text{Na}_1\text{M}_2(\text{PO}_4)_3$.⁸ We also observed an abrupt decline of D_J (i.e., $\sim 5.8 \times 10^{-15} \text{ cm}^2 \text{ s}^{-1}$) in $\text{Na}_1\text{V}_2(\text{PO}_4)_3$, suggesting that further Na extraction $x < 1$ is impractical. Such a drop of diffusivity at $x = 1$ has also been commented on in prior reports.^{38,49,50,57}

Low values of D_J at low Na concentrations limit the full utilization of NaSICON capacities. The extraction of the last Na-ion should happen via $\text{Na}_1\text{V}^{\text{IV}}\text{V}^{\text{IV}}(\text{PO}_4)_3 \leftrightarrow \text{V}^{\text{V}}\text{V}^{\text{IV}}(\text{PO}_4)_3 + \text{e}^- + \text{Na}^+$, in the case of $\text{Na}_x\text{V}_2(\text{PO}_4)_3$. This reaction is not redox-limited, as the high-voltage $\text{V}^{\text{V}}/\text{V}^{\text{IV}}$ redox couple is reversibly accessible.^{19,58,59} To date, the chemical Na extraction from $\text{Na}_1\text{V}_2(\text{PO}_4)_3$ has been elusive.²⁷ The impractical extraction from $\text{Na}_1\text{V}_2(\text{PO}_4)_3$ can be partially attributed to the low Na diffusivities (Figures 2 and 3).^{38,49,50}

We propose that atomic substitutions on either Na sites, transition metal sites, or the inclusion of alternative polyanion groups may represent practical approaches to facilitate the extraction of the last Na ion in these NaSICONs. The feasibility of such a method has been confirmed in several studies.^{19,55,60,61} The last Na ion can be extracted from $\text{Na}_1\text{Nb}_2(\text{PO}_4)_3$ forming the mix-valence $\text{Nb}_2(\text{PO}_4)_3$,⁶² or from the mixed NaSICON $\text{Na}_x\text{TiNb}(\text{PO}_4)_3$.^{63,64} Thus, mixing V with “softer” transition metals from the second and third rows,

bearing redox characteristics similar to those of vanadium, may unlock additional capacity in NaSICONs.

Migration Barriers in Mixed-Transition-Metal NaSICONs. On the one hand, at low Na content (i.e., $x = 1$) transition metals with higher oxidation states will tend to repel the Na ions at Na(1) electrostatically and hence destabilize the Na(1) site with an increase of the site energy at Na(1). In addition, the occurrence of transition metals with higher oxidation states will decrease the electron density on the surrounding O^{2-} , which will reduce their electrostatic attraction to Na ions and increase the repulsion between nearby “O₃” faces of the MO_6 octahedra. This will contribute to enlarging the Na-migration bottlenecks.²⁴ On the other hand, transition metals with a lower oxidation state will attract more Na ions around, resulting in the population of nearby Na(2) sites, which may lower the site energy difference between Na(1) and Na(2) sites at the composition $x = 1$. These considerations suggest that the local charge arrangement with higher/lower oxidation states of transition metals may introduce disorder on the Na vacancy lattice, which may decrease the E_{barrier} at $x = 1$. To quantify this aspect, we evaluated additional Na-migration barriers for NaSICONs with mixed transition metals in a 1:1 ratio (see Figure 4).

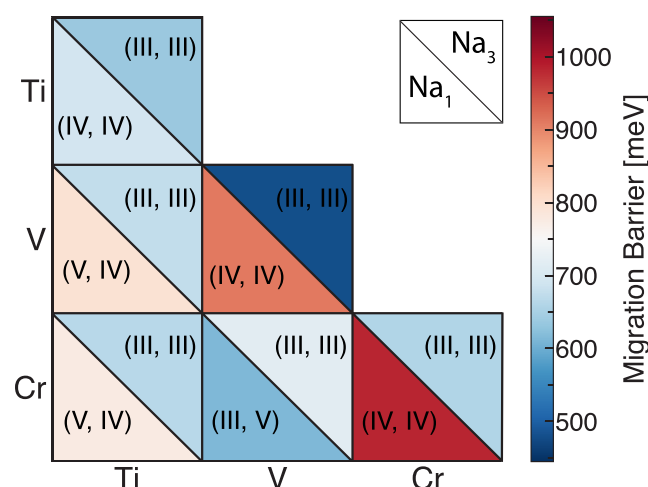


Figure 4. Migration barriers for $\text{Na}_1\text{MM}'(\text{PO}_4)_3$ and $\text{Na}_1\text{MM}'(\text{PO}_4)_3$, where M and M' = Ti, V, or Cr mixed transition metals, where M, M' = Ti, V, or Cr. The ratio of the transition metals is kept at 1:1. The three diagonal squares are 1-transition-metal NaSICONs, where only consistent tetra-valent (IV) and trivalent (III) states were observed at Na_1 and Na_3 compositions. Each square is divided into a lower triangle and a higher triangle, corresponding to the migration barriers for Na_1 and Na_3 compositions, respectively. Within each triangle, we identify the oxidation states of the two transition metals, which provide the local charge ordering environment for migrating Na^+ as (m, n) , where m and n correspond to the oxidation states of the transition metal labeled on the y axis and x axis, respectively. For example, (III, V) in the lower-triangle of the $\text{Na}_1\text{CrV}(\text{PO}_4)_3$ square identifies the local charge arrangement of Cr^{III} and V^{V} oxidation states.

In $\text{Na}_1\text{VTi}(\text{PO}_4)_3$ and $\text{Na}_1\text{VCr}(\text{PO}_4)_3$, we observed an E_{barrier} of ~ 794 and $\sim 613 \text{ meV}$, respectively (see Supporting Figure 10 in the SI), lower than the $\sim 910 \text{ meV}$ in $\text{Na}_1\text{V}_2(\text{PO}_4)_3$. Instead of the single oxidation state of V^{IV} observed at $\text{Na}_1\text{V}_2(\text{PO}_4)_3$, we found a local charge arrangement of V^{V} and Ti^{IV} redox states near the migrating Na ion in

$\text{Na}_1\text{VTi}(\text{PO}_4)_3$. Similarly, in $\text{Na}_1\text{VCr}(\text{PO}_4)_3$, suggest an ordering of the V^{V} and Cr^{III} states (see Supporting Figure 9 in the SI) in agreement with existing experiments.^{55,65} Furthermore, the site energy difference between $\text{Na}(2)$ and $\text{Na}(1)$ also decreased from ~ 880 meV for $\text{Na}_1\text{V}_2(\text{PO}_4)_3$ to 744 meV for $\text{Na}_1\text{VTi}(\text{PO}_4)_3$ and from 576 meV for $\text{Na}_1\text{VCr}(\text{PO}_4)_3$.

The lower values of E_{barrier} for mixed transition-metal-NaSICONs at $x = 1$ will increase D_j for $\text{Na}_1\text{VTi}(\text{PO}_4)_3$ and $\text{Na}_1\text{VCr}(\text{PO}_4)_3$ by ~ 2 and ~ 4 orders of magnitude, respectively,⁴⁵ in comparison to a D_j of $\text{Na}_1\text{V}_2(\text{PO}_4)_3$. A lower E_{barrier} of 774 meV for $\text{Na}_1\text{TiCr}(\text{PO}_4)_3$ will also increase its D_j by approximately 3 orders of magnitude compared to $\text{Na}_1\text{Cr}_2(\text{PO}_4)_3$.

In $\text{Na}_3\text{VTi}(\text{PO}_4)_3$, $\text{Na}_3\text{VCr}(\text{PO}_4)_3$, and $\text{Na}_3\text{TiCr}(\text{PO}_4)_3$, the E_{barrier} values are ~ 676 meV, ~ 719 meV, and ~ 667 meV, respectively (see Supporting Figure 12 in the SI). Only trivalent transition metals, such as V^{III} , Ti^{III} , and Cr^{III} , were found in these systems (see Supporting Figure 11 in the SI), which set specific local charge arrangements for the migrating Na^+ . Compared with the migration barriers for the $\text{Na}_3\text{V}_2(\text{PO}_4)_3$, $\text{Na}_3\text{Ti}_2(\text{PO}_4)_3$, and $\text{Na}_3\text{Cr}_2(\text{PO}_4)_3$ NaSICON analogs at $x = 3$, which were ~ 485 , ~ 638 , and ~ 659 meV, respectively, the deviations between the E_{barrier} of single-transition-metal NaSICON and mixed-transition-metal NaSICON are as small as ~ 50 meV, except $\text{Na}_3\text{V}_2(\text{PO}_4)_3$, which exhibits a significantly lower E_{barrier} .

Our results in Figure 4 indicate that the local charge arrangements on the transition metal sites with higher/lower oxidation states may disrupt potentially stable $\text{Na}-\text{V}$ arrangements at $\text{Na}_1\text{M}_2(\text{PO}_4)_3$, thus lowering the migration barriers and enhancing the $\text{Na}^+ D_j$, which, in turn, may enable the extraction of the last Na. For example, in the case of the $\text{Na}_x\text{V}_2(\text{PO}_4)_3$ system, if compositions with low Na content (i.e., $\text{Na}_{0+x}\text{V}_2(\text{PO}_4)_3$) were thermodynamically stable, the Na extraction from $\text{Na}_1\text{V}_2(\text{PO}_4)_3$ would be highly facilitated because of the favorable local charge arrangement of the mixed-valence vanadium sites $\text{V}^{\text{IV}/\text{V}}$.

4. CONCLUSION

In conclusion, our *ab initio*-based kMC approach revealed the complex relationships among Na-ion transport in $\text{Na}_x\text{Ti}_2(\text{PO}_4)_3$, $\text{Na}_x\text{V}_2(\text{PO}_4)_3$, and $\text{Na}_x\text{Cr}_2(\text{PO}_4)_3$ NaSICON electrode materials as a function of Na content and temperatures. We identified optimal compositions providing maximum intrinsic Na^+ diffusivity for $\text{Na}_x\text{Ti}_2(\text{PO}_4)_3$, $\text{Na}_x\text{V}_2(\text{PO}_4)_3$, and $\text{Na}_x\text{Cr}_2(\text{PO}_4)_3$. Our analysis demonstrated that the Na transport properties of NaSICON materials are highly dependent on the local chemical environments determined by the local arrangements of sodium ions and their vacancies as well as the oxidation states of transition metals. In particular, we elucidated that the environments favoring stable Na-vacancy orderings, typically in the fully charged region, should be disrupted to increase the energy density of NaSICON electrodes, such as $\text{Na}_x\text{V}_2(\text{PO}_4)_3$. The insights gained from this study into the Na^+ diffusion properties in $\text{Na}_x\text{Ti}_2(\text{PO}_4)_3$, $\text{Na}_x\text{V}_2(\text{PO}_4)_3$, and $\text{Na}_x\text{Cr}_2(\text{PO}_4)_3$ shed light on appropriately tailored combinations of transition metals that can be used to access swift Na transport in polyanionic electrodes for inexpensive Na-ion batteries.

■ ASSOCIATED CONTENT

SI Supporting Information

The Supporting Information is available free of charge at <https://pubs.acs.org/doi/10.1021/acsmaterialslett.3c00610>.

Details of simulations of migration barriers with first-principles methods, the formalism of the local cluster expansion, and details of kinetic Monte Carlo simulations ([PDF](#))

■ AUTHOR INFORMATION

Corresponding Author

Pieremanuele Canepa – Department of Materials Science and Engineering, National University of Singapore, Singapore 117575, Singapore; Department of Chemical and Biomolecular Engineering, National University of Singapore, Singapore 117585, Singapore; Department of Electrical and Computer Engineering, University of Houston, Houston, Texas 77204, United States of America; [orcid.org/0000-0002-5168-9253](#); Email: pcanepa@nus.edu.sg, pcanepa@central.uh.edu

Authors

Ziliang Wang – Department of Materials Science and Engineering, National University of Singapore, Singapore 117575, Singapore

Tara P. Mishra – Department of Materials Science and Engineering, National University of Singapore, Singapore 117575, Singapore; Singapore-MIT Alliance for Research and Technology, Singapore 138602, Singapore; [orcid.org/0000-0002-3000-2555](#)

Weihang Xie – Department of Materials Science and Engineering, National University of Singapore, Singapore 117575, Singapore; [orcid.org/0000-0002-6498-2328](#)

Zeyu Deng – Department of Materials Science and Engineering, National University of Singapore, Singapore 117575, Singapore; [orcid.org/0000-0003-0109-9367](#)

Gopalakrishnan Sai Gautam – Department of Materials Engineering, Indian Institute of Science, Bengaluru, Karnataka 560012, India; [orcid.org/0000-0002-1303-0976](#)

Anthony K. Cheetham – Department of Materials Science and Engineering, National University of Singapore, Singapore 117575, Singapore; Materials Department and Materials Research Laboratory, University of California, Santa Barbara, Santa Barbara, California 93106, United States of America; [orcid.org/0000-0003-1518-4845](#)

Complete contact information is available at:
<https://pubs.acs.org/10.1021/acsmaterialslett.3c00610>

Author Contributions

CRedit: Ziliang Wang data curation, formal analysis, investigation, methodology, software, validation, visualization, writing-original draft; Tara Mishra investigation, methodology, software, supervision, writing-review & editing; Xie Weihang methodology, software, validation, writing-review & editing; Zeyu Deng methodology, software, supervision; Gopalakrishnan Sai Gautam formal analysis, supervision, writing-review & editing; Anthony K. Cheetham writing-review & editing; Pieremanuele Canepa conceptualization, funding acquisition, project administration, resources, supervision, validation, writing-review & editing.

Notes

The authors declare no competing financial interest.

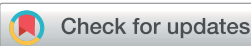
ACKNOWLEDGMENTS

We acknowledge funding from the National Research Foundation, Singapore under his NRF Fellowship NRFF12-2020-0012. Z.D. acknowledges the support from his Lee Kuan Yew Postdoctoral Fellowship 22-S930-A0001. The computational work was performed on resources of the National Supercomputing Centre, Singapore (<https://www.nscc.sg>).

REFERENCES

- (1) Tarascon, J.-M. Is lithium the new gold? *Nat. Chem.* **2010**, *2*, 510–510.
- (2) Olivetti, E. A.; Ceder, G.; Gaustad, G. G.; Fu, X. Lithium-Ion Battery Supply Chain Considerations: Analysis of Potential Bottlenecks in Critical Metals. *Joule* **2017**, *1*, 229–243.
- (3) Turcheniuk, K.; Bondarev, D.; Singhal, V.; Yushin, G. Ten years left to redesign lithium-ion batteries. *Nature* **2018**, *559*, 467–470.
- (4) Palomares, V.; Serras, P.; Villaluenga, I.; Hueso, K. B.; Carretero-González, J.; Rojo, T. Na-ion batteries, recent advances and present challenges to become low cost energy storage systems. *Energy Environ. Sci.* **2012**, *5*, 5884.
- (5) Larcher, D.; Tarascon, J.-M. Towards greener and more sustainable batteries for electrical energy storage. *Nat. Chem.* **2015**, *7*, 19–29.
- (6) Chayambuka, K.; Mulder, G.; Danilov, D. L.; Notten, P. H. L. From Li-Ion Batteries toward Na-Ion Chemistries: Challenges and Opportunities. *Adv. Energy Mater.* **2020**, *10*, 2001310.
- (7) Kaufman, J. L.; Vinckevičiūtė, J.; Krishna Kolli, S.; Gabriel Goiri, J.; Van der Ven, A. Understanding intercalation compounds for sodium-ion batteries and beyond. *Philos. Trans. Royal Soc. A* **2019**, *377*, 20190020.
- (8) Deng, Z.; Sai Gautam, G.; Kolli, S. K.; Chotard, J.-N.; Cheetham, A. K.; Masquelier, C.; Canepa, P. Phase Behavior in Rhombohedral NaSICON Electrolytes and Electrodes. *Chem. Mater.* **2020**, *32*, 7908–7920.
- (9) Deb, D.; Sai Gautam, G. Critical overview of polyanionic frameworks as positive electrodes for Na-ion batteries. *J. Mater. Res.* **2022**, *37*, 3169–3196.
- (10) Singh, B.; Wang, Z.; Park, S.; Gautam, G. S.; Chotard, J.-N.; Croguennec, L.; Carlier, D.; Cheetham, A. K.; Masquelier, C.; Canepa, P. A chemical map of NaSICON electrode materials for sodium-ion batteries. *J. Mater. Chem. A* **2021**, *9*, 281–292.
- (11) Kim, S.-W.; Seo, D.-H.; Ma, X.; Ceder, G.; Kang, K. Electrode Materials for Rechargeable Sodium-Ion Batteries: Potential Alternatives to Current Lithium-Ion Batteries. *Adv. Energy Mater.* **2012**, *2*, 710–721.
- (12) Hasa, I.; Mariyappan, S.; Saurel, D.; Adelhelm, P.; Koposov, A. Y.; Masquelier, C.; Croguennec, L.; Casas-Cabanas, M. Challenges of today for Na-based batteries of the future: From materials to cell metrics. *J. Power Sources* **2021**, *482*, 228872.
- (13) Masquelier, C.; Croguennec, L. Polyanionic (Phosphates, Silicates, Sulfates) Frameworks as Electrode Materials for Rechargeable Li (or Na) Batteries. *Chem. Rev.* **2013**, *113*, 6552–6591.
- (14) Wang, Z.; Park, S.; Deng, Z.; Carlier, D.; Chotard, J.-N.; Croguennec, L.; Gautam, G. S.; Cheetham, A. K.; Masquelier, C.; Canepa, P. Phase stability and sodium-vacancy orderings in a NaSICON electrode. *J. Mater. Chem. A* **2021**, *10*, 209–217.
- (15) Chotard, J.-N.; Rousse, G.; David, R.; Mentré, O.; Courty, M.; Masquelier, C. Discovery of a Sodium-Ordered Form of $\text{Na}_3\text{V}_2(\text{PO}_4)_3$ below Ambient Temperature. *Chem. Mater.* **2015**, *27*, 5982–5987.
- (16) Nogai, A. S.; Stefanovich, S. Y.; Bush, A. A.; Uskenbaev, D. E.; Nogai, A. A. Dipole ordering and ionic conductivity in NASICON-Type $\text{Na}_3\text{Cr}_2(\text{PO}_4)_3$ structures. *Phys. Solid State* **2018**, *60*, 23–30.
- (17) Kawai, K.; Zhao, W.; Nishimura, S.-i.; Yamada, A. High-Voltage $\text{Cr}^{4+}/\text{Cr}^{3+}$ Redox Couple in Polyanion Compounds. *ACS Appl. Energy Mater.* **2018**, *1*, 928–931.
- (18) Senguttuvan, P.; Rousse, G.; Arroyo y de Dompablo, M. E.; Vezin, H.; Tarascon, J.-M.; Palacín, M. R. Low-Potential Sodium Insertion in a NASICON-Type Structure through the Ti(III)/Ti(II) Redox Couple. *J. Am. Chem. Soc.* **2013**, *135*, 3897–3903.
- (19) Lalère, F.; Seznec, V.; Courty, M.; David, R.; Chotard, J. N.; Masquelier, C. Improving the energy density of $\text{Na}_3\text{V}_2(\text{PO}_4)_3$ -based positive electrodes through V/Al substitution. *J. Mater. Chem. A* **2015**, *3*, 16198–16205.
- (20) Lalère, F.; Leriche, J.; Courty, M.; Boulineau, S.; Viallet, V.; Masquelier, C.; Seznec, V. An all-solid state NASICON sodium battery operating at 200 °C. *J. Power Sources* **2014**, *247*, 975–980.
- (21) Zhang, Q.; Liao, C.; Zhai, T.; Li, H. A High Rate 1.2 V Aqueous Sodium-ion Battery Based on All NASICON Structured $\text{NaTi}_2(\text{PO}_4)_3$ and $\text{Na}_3\text{V}_2(\text{PO}_4)_3$. *Electrochim. Acta* **2016**, *196*, 470–478.
- (22) Hong, H.-P. Crystal structures and crystal chemistry in the system $\text{Na}_{1+x}\text{Zr}_2\text{Si}_x\text{P}_{3-x}\text{O}_{12}$. *Mater. Res. Bull.* **1976**, *11*, 173–182.
- (23) Goodenough, J.; Hong, H.-P.; Kafalas, J. Fast Na^+ -ion transport in skeleton structures. *Mater. Res. Bull.* **1976**, *11*, 203–220.
- (24) Park, S.; Wang, Z.; Deng, Z.; Moog, I.; Canepa, P.; Fauth, F.; Carlier, D.; Croguennec, L.; Masquelier, C.; Chotard, J.-N. Crystal Structure of $\text{Na}_x\text{V}_2(\text{PO}_4)_3$, an Intriguing Phase Spotted in the $\text{Na}_3\text{V}_2(\text{PO}_4)_3-\text{Na}_1\text{V}_2(\text{PO}_4)_3$ System. *Chem. Mater.* **2022**, *34*, 451–462.
- (25) Lalère, F.; Seznec, V.; Courty, M.; Chotard, J. N.; Masquelier, C. Coupled X-ray diffraction and electrochemical studies of the mixed Ti/V-containing NASICON: $\text{Na}_2\text{TiV}(\text{PO}_4)_3$. *J. Mater. Chem. A* **2018**, *6*, 6654–6659.
- (26) Ishado, Y.; Inoishi, A.; Okada, S. Exploring Factors Limiting Three- Na^+ Extraction from $\text{Na}_3\text{V}_2(\text{PO}_4)_3$. *Electrochemistry* **2020**, *88*, 457–462.
- (27) Gopalakrishnan, J.; Rangan, K. K. Vanadium phosphate ($\text{V}_2(\text{PO}_4)_3$): a novel NASICO N-type vanadium phosphate synthesized by oxidative deintercalation of sodium from sodium vanadium phosphate ($\text{Na}_3\text{V}_2(\text{PO}_4)_3$). *Chem. Mater.* **1992**, *4*, 745–747.
- (28) Van der Ven, A.; Thomas, J. C.; Xu, Q.; Swoboda, B.; Morgan, D. Nondilute diffusion from first principles: Li diffusion in Li_xTiS_2 . *Phys. Rev. B* **2008**, *78*, 104306.
- (29) Deng, Z.; Mishra, T. P.; Mahayoni, E.; Ma, Q.; Tieu, A. J. K.; Guillon, O.; Chotard, J.-N.; Seznec, V.; Cheetham, A. K.; Masquelier, C.; Gautam, G. S.; Canepa, P. Fundamental investigations on the sodium-ion transport properties of mixed polyanion solid-state battery electrolytes. *Nat. Commun.* **2022**, *13*, 4470.
- (30) Long, O. Y.; Sai Gautam, G.; Carter, E. A. Evaluating optimal U for 3d transition-metal oxides within the SCAN+U framework. *Phys. Rev. Materials* **2020**, *4*, 045401.
- (31) Sun, J.; Ruzsinszky, A.; Perdew, J. Strongly Constrained and Appropriately Normed Semilocal Density Functional. *Phys. Rev. Lett.* **2015**, *115*, 036402.
- (32) Sai Gautam, G.; Carter, E. A. Evaluating transition metal oxides within DFT-SCAN and SCAN+U frameworks for solar thermochemical applications. *Phys. Rev. Materials* **2018**, *2*, 095401.
- (33) Devi, R.; Singh, B.; Canepa, P.; Sai Gautam, G. Effect of exchange-correlation functionals on the estimation of migration barriers in battery materials. *npj Comput. Mater.* **2022**, *8*, 160.
- (34) Sheppard, D.; Terrell, R.; Henkelman, G. Optimization methods for finding minimum energy paths. *J. Chem. Phys.* **2008**, *128*, 134106.
- (35) Van der Ven, A.; Ceder, G.; Asta, M.; Tepesch, P. D. First-principles theory of ionic diffusion with nondilute carriers. *Phys. Rev. B* **2001**, *64*, 184307.
- (36) Van der Ven, A.; Deng, Z.; Banerjee, S.; Ong, S. P. Rechargeable Alkali-Ion Battery Materials: Theory and Computation. *Chem. Rev.* **2020**, *120*, 6977–7019.
- (37) Boilot, J.; Collin, G.; Colombari, P. Relation structure-fast ion conduction in the NASICON solid solution. *J. Solid State Chem.* **1988**, *73*, 160–171.

- (38) Chen, S.; Wu, C.; Shen, L.; Zhu, C.; Huang, Y.; Xi, K.; Maier, J.; Yu, Y. Challenges and Perspectives for NASICON-Type Electrode Materials for Advanced Sodium-Ion Batteries. *Adv. Mater.* **2017**, *29*, 1700431.
- (39) Kabbour, H.; Coillot, D.; Colmont, M.; Masquelier, C.; Mentré, O. α -Na₃M₂(PO₄)₃ (M = Ti, Fe): Absolute Cationic Ordering in NASICON-Type Phases. *J. Am. Chem. Soc.* **2011**, *133*, 11900–11903.
- (40) Lucaleau, G.; Barj, M.; Soubeyroux, J.; Dianoux, A.; Delmas, C. Neutron scattering and diffraction study of Na₃Cr₂P₃O₁₂, NaZr₂P₃O₁₂ and Na₃ZrMgP₃O₁₂. *Solid State Ionics* **1986**, *18–19*, 959–963.
- (41) Bui, K. M.; Dinh, V. A.; Okada, S.; Ohno, T. Hybrid functional study of the NASICON-type Na₃V₂(PO₄)₃: crystal and electronic structures, and polaron–Na vacancy complex diffusion. *Phys. Chem. Chem. Phys.* **2015**, *17*, 30433–30439.
- (42) McKee, J. R.; Kauffman, J. M. A practical Solvay process experiment. *J. Chem. Educ.* **1981**, *58*, 1035.
- (43) Cox, P. A. *Transition Metal Oxides*; Oxford University Press: New York, 1995; p 296.
- (44) Deng, Z.; Mishra, T. P.; Xie, W.; Saeed, D. A.; Gautam, G. S.; Canepa, P. kMCpy: A python package to simulate transport properties in solids with kinetic Monte Carlo. *Comput. Mater. Sci.* **2023**, *229*, 112394.
- (45) Rong, Z.; Malik, R.; Canepa, P.; Sai Gautam, G.; Liu, M.; Jain, A.; Persson, K.; Ceder, G. Materials Design Rules for Multivalent Ion Mobility in Intercalation Structures. *Chem. Mater.* **2015**, *27*, 6016–6021.
- (46) Delmas, C.; Cherkaoui, F.; Nadiri, A.; Hagenmuller, P. A nasicon-type phase as intercalation electrode: NaTi₂(PO₄)₃. *Mater. Res. Bull.* **1987**, *22*, 631–639.
- (47) Fang, J.; Wang, S.; Li, Z.; Chen, H.; Xia, L.; Ding, L.; Wang, H. Porous Na₃V₂(PO₄)₃@C nanoparticles enwrapped in three-dimensional graphene for high performance sodium-ion batteries. *J. Mater. Chem. A* **2016**, *4*, 1180–1185.
- (48) Kaxiras, E.; Erlebacher, J. Adatom diffusion by orchestrated exchange on semiconductor surfaces. *Phys. Rev. Lett.* **1994**, *72*, 1714–1717.
- (49) Lan, T.; Ma, Q.; Tsai, C.; Tietz, F.; Guillon, O. Ionic Conductivity of Na₃V₂P₃O₁₂ as a Function of Electrochemical Potential and its Impact on Battery Performance. *Batteries & Supercaps* **2021**, *4*, 479–484.
- (50) Böckenfeld, N.; Balducci, A. Determination of sodium ion diffusion coefficients in sodium vanadium phosphate. *J. Solid State Electrochem.* **2014**, *18*, 959–964.
- (51) Shen, W.; Li, H.; Wang, C.; Li, Z.; Xu, Q.; Liu, H.; Wang, Y. Improved electrochemical performance of the Na₃V₂(PO₄)₃ cathode by B-doping of the carbon coating layer for sodium-ion batteries. *J. Mater. Chem. A* **2015**, *3*, 15190–15201.
- (52) Pang, G.; Yuan, C.; Nie, P.; Ding, B.; Zhu, J.; Zhang, X. Synthesis of NASICON-type structured NaTi₂(PO₄)₃ – graphene nanocomposite as an anode for aqueous rechargeable Na-ion batteries. *Nanoscale* **2014**, *6*, 6328–6334.
- (53) Vijayan, L.; Cheruku, R.; Govindaraj, G.; Rajagopan, S. Physical and electrical properties of combustion synthesized NASICON type Na₃Cr₂(PO₄)₃ crystallites: Effect of glycine molar ratios. *Mater. Chem. Phys.* **2011**, *130*, 862–869.
- (54) Chen, F.; Kovrugin, V. M.; David, R.; Mentré, O.; Fauth, F.; Chotard, J.; Masquelier, C. A NASICON-Type Positive Electrode for Na Batteries with High Energy Density: Na₄MnV(PO₄)₃. *Small Methods* **2019**, *3*, 1800218.
- (55) Liu, R.; Xu, G.; Li, Q.; Zheng, S.; Zheng, G.; Gong, Z.; Li, Y.; Kruskop, E.; Fu, R.; Chen, Z.; Amine, K.; Yang, Y. Exploring Highly Reversible 1.5-Electron Reactions (V³⁺/V⁴⁺/V⁵⁺) in Na₃VCr(PO₄)₃ Cathode for Sodium-Ion Batteries. *ACS Appl. Mater. Interfaces* **2017**, *9*, 43632–43639.
- (56) Wang, J.; Wang, Y.; Seo, D.; Shi, T.; Chen, S.; Tian, Y.; Kim, H.; Ceder, G. A High-Energy NASICON-Type Cathode Material for Na-Ion Batteries. *Adv. Energy Mater.* **2020**, *10*, 1903968.
- (57) Niu, Y.; Xu, M.; Zhang, Y.; Han, J.; Wang, Y.; Li, C. M. Detailed investigation of a NaTi₂(PO₄)₃ anode prepared by pyro-synthesis for Na-ion batteries. *RSC Adv.* **2016**, *6*, 45605–45611.
- (58) Wang, Q.; Zhao, Y.; Gao, J.; Geng, H.; Li, J.; Jin, H. Triggering the Reversible Reaction of V³⁺/V⁴⁺/V⁵⁺ in Na₃V₂(PO₄)₃ by Cr³⁺ Substitution. *ACS Appl. Mater. Interfaces* **2020**, *12*, 50315–50323.
- (59) Wang, Q.; Gao, H.; Li, J.; Liu, G.-B.; Jin, H. Importance of Crystallographic Sites on Sodium-Ion Extraction from NASICON-Structured Cathodes for Sodium-Ion Batteries. *ACS Appl. Mater. Interfaces* **2021**, *13*, 14312–14320.
- (60) Patoux, S.; Rousse, G.; Leriche, J.-B.; Masquelier, C. Structural and Electrochemical Studies of Rhombohedral Na₂TiM(PO₄)₃ and Li_{1.6}Na_{0.4}TiM(PO₄)_{rm3} (M = Fe, Cr) Phosphates. *Chem. Mater.* **2003**, *15*, 2084–2093.
- (61) Park, S.; Chotard, J.-N.; Carlier, D.; Moog, I.; Duttine, M.; Fauth, F.; Iadecola, A.; Croguennec, L.; Masquelier, C. An Asymmetric Sodium Extraction/Insertion Mechanism for the Fe/V-Mixed NASICON Na₄FeV(PO₄)₃. *Chem. Mater.* **2022**, *34*, 4142–4152.
- (62) Patra, B.; Kumar, K.; Deb, D.; Ghosh, S.; Gautam, G. S.; Senguttuvan, P. Unveiling a high capacity multi-redox (Nb⁵⁺/Nb⁴⁺/Nb³⁺) NASICON-Nb₂(PO₄)₃ anode for Li- and Na-ion batteries. *J. Mater. Chem. A* **2023**, *11*, 8173.
- (63) Bennouna, L.; Arsalane, S.; Brochu, R.; Lee, M.; Chassaing, J.; Quarton, M. Specificites des ions Nb^{IV} et Mo^{IV} dans les monophosphates de type Nasicon. *J. Solid State Chem.* **1995**, *114*, 224–229.
- (64) Tillement, O.; Couturier, J.; Angenault, J.; Quarton, M. Crystal chemistry and electrical study of Na_xNbTi(PO₄)₃. *Solid State Ionics* **1991**, *48*, 249–255.
- (65) Wang, D.; Bie, X.; Fu, Q.; Dixon, D.; Bramnik, N.; Hu, Y.-S.; Fauth, F.; Wei, Y.; Ehrenberg, H.; Chen, G.; Du, F. Sodium vanadium titanium phosphate electrode for symmetric sodium-ion batteries with high power and long lifespan. *Nat. Commun.* **2017**, *8*, 15888.



Cite this: *J. Mater. Chem. A*, 2021, **9**, 281

A chemical map of NaICON electrode materials for sodium-ion batteries†

Baltej Singh,^{‡,a} Ziliang Wang,^{‡,a} Sunkyu Park,^{bcd} Gopalakrishnan Sai Gautam,^{ID, e} Jean-Noël Chotard,^{bdf} Laurence Croguennec,^{ID, cdf} Dany Carlier,^{cdf} Anthony K. Cheetham,^{ID, ag} Christian Masquelier^{ID, bdf} and Pieremanuele Canepa^{ID, *ah}

Na-ion batteries are promising devices for smart grids and electric vehicles due to the cost effectiveness arising from the overall abundance of sodium (Na) and its even geographical distribution. Among other factors, the energy density of Na-ion batteries is limited by the cathode electrode chemistry. NaICON-based electrode materials are known for their wide range of electrochemical potentials, high ionic conductivity, and most importantly their structural and thermal stabilities. Using first-principles calculations, we chart the chemical space of 3d transition metal-based NaICON phosphates with the formula $\text{Na}_x\text{MM}'(\text{PO}_4)_3$ (with M and M' = Ti, V, Cr, Mn, Fe, Co and Ni) to analyze their thermodynamic stabilities and the intercalation voltages for Na^+ ions. Specifically, we compute the Na insertion voltages and related properties of 28 distinct NaICON compositions. We investigate the thermodynamic stability of Na-intercalation in previously unreported $\text{Na}_x\text{Mn}_2(\text{PO}_4)_3$ and $\text{Na}_x\text{VCo}(\text{PO}_4)_3$. The calculated quaternary phase diagrams of the Na-P-O-Co and Na-P-O-Ni chemical systems explain the origin of the suspected instability of Ni and Co-based NaICON compositions. From our analysis, we are also able to rationalize anomalies in previously reported experimental data in this diverse and important chemical space.

Received 2nd November 2020
Accepted 21st November 2020

DOI: 10.1039/d0ta10688g
rsc.li/materials-a

1. Introduction

Developing new battery systems capable of storing increasing quantities of energy poses extraordinary scientific and economic challenges. Lithium (Li)-ion batteries power the world's portable devices, such as mobile phones, cameras, laptops, etc., but the supply chains of Li and the required

transition metals may soon be at risk due to geopolitical considerations.^{1,2} Sodium (Na) appears to be a viable alternative to Li for battery applications due to its earth abundance, as well as the possibility of harvesting it directly from sea water. With Na being ~50 times more affordable compared to Li, Na-ion batteries (NIBs) are being explored by researchers worldwide, including a number of commercialization attempts.^{3–8} In addition, inexpensive stainless-steel current collectors are typically used in NIBs instead of the expensive copper ones found in Li-ion cells.

Cathode materials factor prominently in the overall energy density stored by NIBs, and the optimization of electrode chemistries to provide high intercalation voltages and gravimetric/volumetric capacities remains a crucial aspect in the design of competitive NIBs. In theory, transition metal layered oxide-based cathode materials for NIBs would offer the largest theoretical energy densities.^{5–7,9,10} However, the dominant two dimensional character of their structures strongly affects the longevity of the cathode material, with the electrochemical cell exhibiting a shorter-than-desired cycle life.^{6,7,10–15} Promising alternatives to layered oxides are polyanion-based cathode materials.¹⁶ Polyanion electrode materials leverage a combination of multivalent cations (e.g., P^{5+} , Si^{4+} and S^{6+}) and anions (mostly O^{2-}) arranging into phosphate, silicate and sulfate (PO_4^{3-} , SiO_4^{4-} and SO_4^{2-}), which are thermodynamically stable by virtue of the strong binding energy of their polyanionic covalent bonds.^{17–19}

^aDepartment of Materials Science and Engineering, National University of Singapore, Singapore 117575, Singapore. E-mail: pcanepa@nus.edu.sg

^bLaboratoire de Réactivité et de Chimie des Solides (LRCS), CNRS UMR 7314, Université de Picardie Jules Verne, 80039 Amiens Cedex, France. E-mail: christian.masquelier@u-picardie.fr

^cCNRS, Univ. Bordeaux, Bordeaux INP, ICMCB, UMR CNRS 5026, F-33600, Pessac, France

^dRS2E, Réseau Français sur le Stockage Electrochimique de l'Energie, FR CNRS 3459, F-80039 Amiens Cedex 1, France

^eDepartment of Materials Engineering, Indian Institute of Science, Bengaluru, 560012, Karnataka, India

^fALISTORE-ERI European Research Institute, FR CNRS 3104, Amiens, F-80039 Cedex 1, France

^gMaterials Department and Materials Research Laboratory, University of California, Santa Barbara, California 93106, USA

^hChemical and Biomolecular Engineering, National University of Singapore, 4 Engineering Drive 4, Singapore, 117585

† Electronic supplementary information (ESI) available. See DOI: [10.1039/d0ta10688g](https://doi.org/10.1039/d0ta10688g)

‡ These authors contributed equally.

An important class of phosphate electrodes discovered by Hong and Goodenough is the Natrium Super Ionic CONductors (NaSICONs),^{20,21} with the formula $\text{Na}_x\text{MM}'(\text{XO}_4)_3$, where M and M' are metals and X = Si, P and/or S. NaSICON electrode materials and electrolytes typically display significant Na^+ -mobility.²² The NaSICON framework is important for the development of new NIB materials,^{17,22–29} since its structural tunability enables the exploration of a vast chemical space, which greatly diversifies the potential, electrochemical properties and related structural features. In theory, a charged $\text{MM}'(\text{PO}_4)_3$ NaSICON framework with redox-active transition metals M and M' would allow the intercalation of up to 4 Na^+ ions,⁹ which make these materials promising in terms of energy density.³⁰ Notwithstanding the challenges of working with carbon-based anodes in NIBs,^{9,31–33} one could benefit from the presence of 4 Na^+ ions in NaSICONs, *e.g.*, $\text{Na}_4\text{Mn}^{\text{II}}\text{V}^{\text{III}}(\text{PO}_4)_3$.^{34,35} However, the reversible extraction/intercalation of 4 Na^+ ions is yet to be reported in NaSICON frameworks.

As an example of a NaSICON cathode electrode, $\text{Na}_3\text{V}^{\text{III}}\text{V}^{\text{III}}(\text{PO}_4)_3$ (NVP) can reversibly exchange two electrons (*via* the activation of the $\text{V}^{\text{IV}}/\text{V}^{\text{III}}$ redox couple) delivering $\text{Na}_1\text{V}^{\text{IV}}\text{V}^{\text{IV}}(\text{PO}_4)_3$ at an average voltage of ~3.4 V *vs.* Na/Na^+ with a capacity of ~110 mA h g⁻¹ and an energy density of ~370 W h kg⁻¹.^{27,36,37} One additional Na^+ can be inserted (electro)chemically into NVP to achieve $\text{Na}_4\text{V}^{\text{II}}\text{V}^{\text{III}}(\text{PO}_4)_3$ with a voltage of ~1.63 V *vs.* Na/Na^+ . The reversible extraction of 3 Na^+ ions (*i.e.*, starting from $\text{Na}_4\text{V}^{\text{II}}\text{V}^{\text{III}}(\text{PO}_4)_3$ as the pristine material to $\text{Na}_1\text{V}^{\text{IV}}\text{V}^{\text{IV}}(\text{PO}_4)_3$) is possible but not practical due to the 1.8 V difference between the two processes ($\text{V}^{\text{IV}}/\text{V}^{\text{III}}$ and $\text{V}^{\text{III}}/\text{V}^{\text{II}}$) and the difficult synthesis of $\text{Na}_4\text{V}_2(\text{PO}_4)_3$. Uebou *et al.*³⁸ demonstrated the extraction of ~2.5 Na^+ ions with partial reversibility.

Symmetric Na electrochemical cells entirely made of NaSICON frameworks adopt NVP as both the electrodes;³⁹ in the charged state of the battery the anode is $\text{Na}_4\text{V}^{\text{II}}\text{V}^{\text{II}}(\text{PO}_4)_3$ and the cathode is $\text{Na}_1\text{V}^{\text{IV}}\text{V}^{\text{IV}}(\text{PO}_4)_3$ with $\text{Na}_3\text{Zr}_2\text{Si}_2\text{PO}_{12}$ as the electrolyte. This could deliver an average voltage of ~1.8 V.^{39–41} NVP suffers from poor intrinsic electronic conductivity due to the isolated VO_6 octahedra, which are never face-, edge- or corner-sharing with each other,^{25,42} in contrast to their arrangement in layered-oxide cathodes where edge-sharing exists between MO_6 moieties.^{6,9}

The Ti analogue of NVP is the Ti^{IV} -containing $\text{NaTi}^{\text{IV}}\text{Ti}^{\text{IV}}(\text{PO}_4)_3$ composition, which is stable in air and can reversibly exchange two electrons by benefitting from the $\text{Ti}^{\text{IV}}/\text{Ti}^{\text{III}}$ redox couple, but at a lower voltage of ~2.1 V *vs.* Na/Na^+ compared to that of ~3.4 V for $\text{V}^{\text{IV}}/\text{V}^{\text{III}}$ redox in NVP.^{25,26} $\text{NaTi}^{\text{IV}}\text{Ti}^{\text{IV}}(\text{PO}_4)_3$ is also commonly used as a negative electrode material.²⁸ The NaSICON $\text{Na}_3\text{Fe}^{\text{III}}\text{Fe}^{\text{III}}(\text{PO}_4)_3$ exhibits a voltage-composition plateau at ~2.5 V *vs.* Na/Na^+ with a discharge capacity of ~61 mA h g⁻¹ and is associated with the redox couple $\text{Fe}^{\text{III}}/\text{Fe}^{\text{II}}$.⁴³ The $\text{Fe}^{\text{IV}}/\text{Fe}^{\text{III}}$ redox couple was claimed to be observed in $\text{Na}_3\text{Fe}^{\text{III}}\text{Fe}^{\text{III}}(\text{PO}_4)_3$ at ~3.4 V *vs.* Na/Na^+ , with a limited specific discharge capacity of ~22 mA h g⁻¹.⁴⁴ Nevertheless, the formation of tetravalent iron ions has not yet been reproduced.

Yamada *et al.*⁴⁵ reported a voltage of ~4.5 V *vs.* Na/Na^+ (enabled by the reversible $\text{Cr}^{\text{IV}}/\text{Cr}^{\text{III}}$ redox couple) when Na^+ is extracted from $\text{Na}_3\text{Cr}^{\text{III}}\text{Cr}^{\text{III}}(\text{PO}_4)_3$, which corresponds to the highest voltage ever reported among NaSICON materials with a single TM species. Importantly, the Mn, Co and Ni, $\text{Na}_x\text{M}_2(-\text{PO}_4)_3$ NaSICON analogues have not yet been reported.

The high voltage delivered by the $\text{Cr}^{\text{IV}}/\text{Cr}^{\text{III}}$ redox couple offers scope for exploring new high-voltage/capacity materials using more than one TM, *e.g.*, $\text{Na}_4\text{Cr}^{\text{III}}\text{Mn}^{\text{II}}(\text{PO}_4)_3$.^{30,46} Other NaSICON materials, such as $\text{Na}_3\text{V}^{\text{III}}\text{Cr}^{\text{III}}(\text{PO}_4)_3$,⁴⁷ $\text{Na}_2\text{Ti}^{\text{IV}}\text{V}^{\text{III}}(\text{PO}_4)_3$,^{48,49} $\text{Na}_3\text{Ti}^{\text{IV}}\text{Mn}^{\text{II}}(\text{PO}_4)_3$,^{50,51} $\text{Na}_2\text{Ti}^{\text{IV}}\text{Fe}^{\text{III}}(\text{PO}_4)_3$,⁵² $\text{Na}_4\text{V}^{\text{III}}\text{Mn}^{\text{II}}(\text{PO}_4)_3$,^{34,35,53–56} $\text{Na}_3\text{V}^{\text{III}}\text{Fe}^{\text{III}}(\text{PO}_4)_3$ (ref. 29 and 35) and $\text{Na}_4\text{V}^{\text{III}}\text{Ni}^{\text{II}}(\text{PO}_4)_3$,³⁵ have also been studied to enable high reversible capacity and longevity as anode and cathode electrodes.

In general, to access three electrons (*i.e.*, 3 Na^+ ions per 2 TMs per formula unit) in any mixed TM NaSICON, two criteria must be met: (i) the TM must be in the +2 and +3 oxidation states in the fully discharged state (*i.e.*, 4 Na^+ ions) and (ii) at least one of the TMs must accommodate multiple redox active oxidation states. Compounds that meet these criteria are mainly either Mn or V-based NaSICONs, *e.g.*, $\text{Na}_2\text{Ti}^{\text{IV}}\text{V}^{\text{III}}(\text{PO}_4)_3$, $\text{Na}_3\text{Ti}^{\text{IV}}\text{Mn}^{\text{II}}(\text{PO}_4)_3$, $\text{Na}_4\text{Mn}^{\text{II}}\text{V}^{\text{III}}(\text{PO}_4)_3$, and $\text{Na}_4\text{Cr}^{\text{III}}\text{Mn}^{\text{II}}(\text{PO}_4)_3$, which undergo reversible electrochemical reactions up to three electrons with average voltages of ~2.4, ~3.2, ~3.4, and ~4.1 V *vs.* Na/Na^+ . While $\text{Na}_4\text{Cr}^{\text{III}}\text{Mn}^{\text{II}}(\text{PO}_4)_3$ exhibits a high theoretical energy density (566 W h kg⁻¹) for a gravimetric capacity of 160 mA h g⁻¹,³⁰ only ~40 mA h g⁻¹ was reported at voltages below 1.6 V *vs.* Na/Na^+ .

However, there remains a wide chemical space yet to be explored, which could yield new combinations of TMs enabling improved NaSICON electrode materials. A systematic study, either experimental or theoretical, of trends in voltages and the phase behavior of possible transition-metal combinations within NaSICON electrode materials has not yet been reported.

We present a first-principles study that charts the chemical space of 28 different $\text{Na}_x\text{MM}'(\text{PO}_4)_3$ -electrode chemistries, where M and M' can be any of the 3d TM, Ti, V, Cr, Mn, Fe, Co and Ni, with the Na content varying in the range of $1 \leq x \leq 4$. We derive the intercalation voltages for all the 28 $\text{Na}_x\text{MM}'(\text{PO}_4)_3$ systems, validate our predictions with available experimental data, and identify promising NaSICON compositions to be targeted experimentally. We find new promising or not fully explored $\text{Na}_x\text{MM}'(\text{PO}_4)_3$ compositions, *e.g.*, $\text{Na}_x\text{Mn}_2(\text{PO}_4)_3$ ($1 \leq x \leq 4$), $\text{Na}_x\text{Co}_2(\text{PO}_4)_3$ ($3 \leq x \leq 4$), $\text{Na}_x\text{TiCo}(\text{PO}_4)_3$ ($2 \leq x \leq 4$), $\text{Na}_x\text{VCo}(\text{PO}_4)_3$ ($1 \leq x \leq 4$), $\text{Na}_x\text{CrCo}(\text{PO}_4)_3$ ($2 \leq x \leq 4$), $\text{Na}_x\text{CoMn}(\text{PO}_4)_3$ ($2 \leq x \leq 4$) and $\text{Na}_x\text{CrFe}(\text{PO}_4)_3$ ($2 \leq x \leq 4$). We analyze the possible origins of the difficulties in synthesizing specific NaSICON chemistries.

2. Results

2.1 Structural features of $\text{Na}_x\text{MM}'(\text{PO}_4)_3$ electrodes

Depending on the TM species, temperature and/or Na content (x) per formula unit (f.u.) NaSICON materials typically adopt a rhombohedral ($R\bar{3}C$),^{45,57} an ordered monoclinic ($C2/c$ or Cc),^{20,21,47} or, in the specific case of $\alpha\text{-Na}_3\text{Ti}^{\text{III}}\text{Ti}^{\text{III}}(\text{PO}_4)_3$,

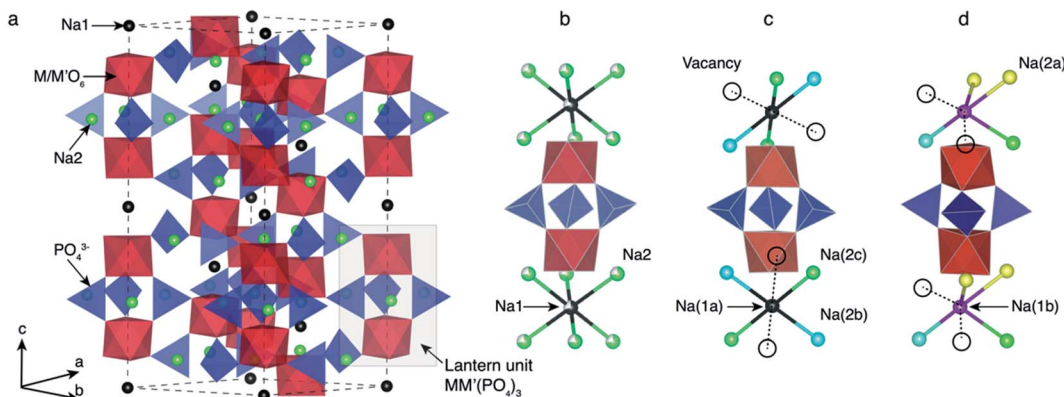


Fig. 1 (a) The rhombohedral ($R\bar{3}c$) structure of $\text{Na}_4\text{MM}'(\text{PO}_4)_3$ with M and $\text{M}' = \text{Ti}, \text{V}, \text{Cr}, \text{Mn}, \text{Fe}, \text{Co}$ and Ni. The “lantern unit” is made up of two MO_6 (or $\text{M}'\text{O}_6$) octahedra (red) sharing corners with PO_4^{3-} tetrahedra (blue). The gray box in (a) highlights the arrangement of the lantern units. Two distinct Na ions, *i.e.*, Na1 (black) and Na2 (green), are present in the rhombohedral NaSICONs. Panel (b) shows the lantern representation of the Na disordering (with partial Na occupancies on Na1 and Na2 sites) in the rhombohedral $\text{Na}_3\text{MM}'(\text{PO}_4)_3$ polymorph. Panel (c) shows a local view (lantern unit) of the complete ordering of Na^+ ions in the corresponding $\text{Na}_3\text{MM}'(\text{PO}_4)_3$ monoclinic ($C2/c$) phase. Panel (d) shows the local environment of sites Na1b (violet) and Na2a (yellow) in the same monoclinic arrangement. Vacancies are represented by open circles.

a triclinic structure ($P\bar{1}$).⁵⁸ For example, $\text{Na}_4\text{V}^{\text{II}}\text{V}^{\text{III}}(\text{PO}_4)_3$ and $\text{Na}_4\text{Fe}^{\text{II}}\text{Fe}^{\text{III}}(\text{PO}_4)_3$ (ref. 59) are rhombohedral, while $\text{Na}_3\text{V}^{\text{III}}\text{V}^{\text{III}}(\text{PO}_4)_3$,⁵⁷ $\text{Na}_3\text{Fe}^{\text{III}}\text{Fe}^{\text{III}}(\text{PO}_4)_3$,⁴³ $\text{Na}_3\text{Ti}^{\text{III}}\text{Ti}^{\text{III}}(\text{PO}_4)_3$ and $\text{Na}_3\text{Cr}^{\text{III}}\text{Cr}^{\text{III}}(\text{PO}_4)_3$ tend to form monoclinic⁵⁸ structures at room temperature due to Na/vacancy orderings. Fig. 1 shows the archetypal structure of the rhombohedral $\text{Na}_x\text{MM}'(\text{PO}_4)_3$.

$\text{Na}_x\text{MM}'(\text{PO}_4)_3$ materials consist of (M, M') O_6 octahedral and PO_4 tetrahedral units. As shown in Fig. 1, three PO_4 tetrahedra share all their corners with two (M, M') O_6 octahedra forming the “lantern units”—a recurrent motif of NaSICON structures. The lantern units assemble into a 3-D MM'(PO_4)₃ framework producing two types of available sites for Na in the rhombohedral phase (Fig. 1b): Na1 (one per f.u.) and Na2 (three per f.u.). The six-coordinated Na1 sites are located between two (M, M') O_6 octahedra, while the Na2 sites remain eight-coordinated with the O atoms of the PO_4 tetrahedra. At $x = 4$ in $\text{Na}_x\text{MM}'(\text{PO}_4)_3$, all the Na positions (*i.e.*, 1 × Na1 and 3 × Na2 per f.u.) are fully occupied and the structure is ordered and rhombohedral. In several NaSICONs, the Na^+ ions are fully ordered at $x = 3$ and the structure adopts monoclinic ($C2/c$) symmetry (Fig. 1c), where the Na1 site splits into two distinct sites (*i.e.*, fully occupied Na1a and Na1b). The Na2 site splits into five sites (3 fully occupied, Na2a, Na2b and Na2c, and 2 vacancies).

2.2 Na intercalation in $\text{Na}_x\text{M}_2(\text{PO}_4)_3$ NaSICONs

The energetics of Na intercalation and the corresponding average voltages (see Methodology in Section 5) for single TM (M = M') NaSICON electrodes are shown in panels (a) and (b) of Fig. 2. The computed formation energies for the most stable orderings in $\text{Na}_x\text{M}_2(\text{PO}_4)_3$ are displayed in Fig. 2a as a function of Na concentration, where the lower energy envelopes form the so-called convex hull (solid lines) for a given $\text{Na}_x\text{M}_2(\text{PO}_4)_3$ system. The convex hull highlights the thermodynamic phase behavior at 0 K of Na (de)intercalation from/into the $\text{Na}_x\text{M}_2(\text{PO}_4)_3$ frameworks. Since the convex hull at 0 K does not include

any entropic and pV effects, it informs on the propensity of Na to bond with the $\text{M}_2(\text{PO}_4)_3$ frameworks. Among the M = Ti, V, Cr, Mn, Fe, Co and Ni compounds, NaSICONs based on Ti, V, Cr and Fe have been reported experimentally.^{28,36,43–45} From previous experimental work, the redox activities of Ti and V provide accessible Na concentrations ranging in $1 \leq x \leq 4$, while $\text{Na}_x\text{Cr}_2(\text{PO}_4)_3$ spans a narrower range of Na concentration ($1 \leq x \leq 3$), being limited by the $\text{Cr}^{\text{IV}}/\text{Cr}^{\text{III}}$ redox couple. Notably, the $\text{Cr}^{\text{III}}/\text{Cr}^{\text{II}}$ redox couple has not been cycled reversibly in NaSICON frameworks so far.

The structures represented by specific Na/vacancy orderings falling above the convex hull are thermodynamically unstable/metastable and are shown in Fig. S1–S7 of the ESI.† Note that the unstable Na/vacancy orderings should decompose to the closest ground state(s) identified by the convex hulls in Fig. 2a. For example, in Fig. S2,† $\text{Na}_2\text{V}_2(\text{PO}_4)_3$ ($C2$) is found to be slightly metastable (~1.8 meV per atom above the stability line) and will phase separate into $\text{Na}_1\text{V}^{\text{IV}}\text{V}^{\text{IV}}(\text{PO}_4)_3$ and $\text{Na}_3\text{V}^{\text{III}}\text{V}^{\text{III}}(\text{PO}_4)_3$. Given the small metastability of $\text{Na}_2\text{V}_2(\text{PO}_4)_3$, we expect this compound to be stabilized by entropic effects. Consequently, the stable structures lying on the convex hull (*e.g.*, $\text{Na}_3\text{V}^{\text{III}}\text{V}^{\text{III}}(\text{PO}_4)_3$) give rise to a “step” in the calculated Na voltage curve (see Fig. S2†). The convexity, that is the depth of the convex hull, is an indication of the thermodynamic stabilities of the specific Na/vacancy configurations. The calculated ground states on the convex hull do not necessarily correspond to topotactic structures since we allow changes to the symmetry (*e.g.*, rhombohedral → monoclinic) of the host during deintercalation of Na from $\text{Na}_4\text{MM}'(\text{PO}_4)_3$ in our calculations.

Analyzing Fig. 2a and b, the following general trends can be deduced:

- (i) The end member compositions in $\text{Na}_x\text{M}_2(\text{PO}_4)_3$, *i.e.*, $x = 1$ and 4, typically adopt the rhombohedral ($R\bar{3}c$ or $R\bar{3}$) space group. Exceptions to this trend are $\text{Na}_4\text{Cr}^{\text{II}}\text{Cr}^{\text{III}}(\text{PO}_4)_3$ and $\text{Na}_4\text{Mn}^{\text{II}}\text{Mn}^{\text{III}}(\text{PO}_4)_3$, which are predicted to have triclinic ($P\bar{1}$) symmetry probably due to Jahn–Teller distortions of high-spin

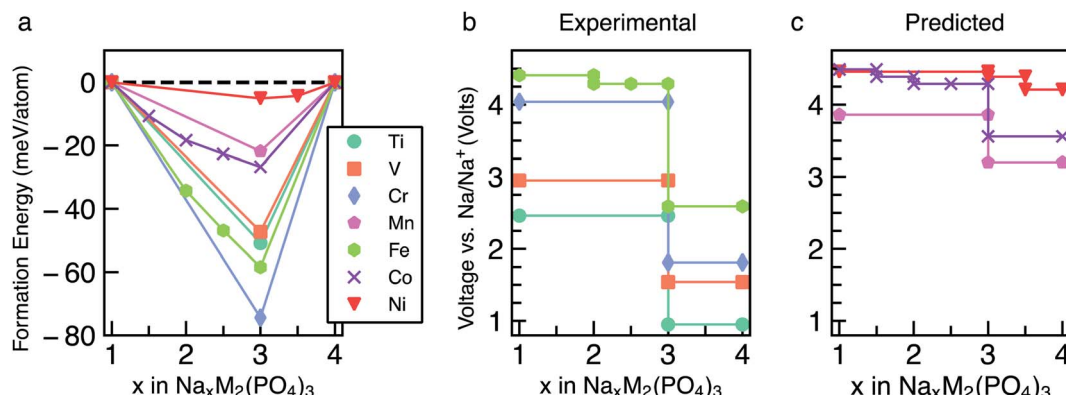


Fig. 2 Panel (a) shows the computed formation energies and respective convex hulls for Na vacancy orderings as a function of Na concentration (x) in $\text{Na}_x\text{M}_2(\text{PO}_4)_3$ where $\text{M} = \text{Ti}, \text{V}, \text{Cr}, \text{Mn}, \text{Fe}, \text{Co}$ and Ni . Panels (b) and (c) show the intercalation voltages vs. Na/Na^+ for the experimentally known ($\text{M} = \text{Ti}, \text{V}, \text{Cr}$ and Fe) and predicted ($\text{M} = \text{Mn}, \text{Co}$ and Ni) $\text{Na}_x\text{M}_2(\text{PO}_4)_3$ compounds, respectively. Only the stable orderings forming the convex hull are displayed in panel (a). The energies of unstable configurations for each convex hull are shown in Fig. S1–S7 of the ESI.[†]

Cr^{2+} and Mn^{3+} d⁴ ions. These have not yet been observed experimentally.

(ii) A global minimum in the formation energy curves is present across all transition-metal $\text{Na}_x\text{M}_2(\text{PO}_4)_3$ systems at $x = 3$ (Fig. 2a).⁴¹

(iii) Among all the $\text{Na}_3\text{M}^{\text{III}}\text{M}^{\text{III}}(\text{PO}_4)_3$ compounds investigated, $\text{Na}_3\text{Cr}^{\text{III}}\text{Cr}^{\text{III}}(\text{PO}_4)_3$ displays the deepest or lowest (*i.e.*, most favorable) formation energy, followed by $\text{Na}_3\text{-Fe}^{\text{III}}\text{Fe}^{\text{III}}(\text{PO}_4)_3 > \text{Na}_3\text{Ti}^{\text{III}}\text{Ti}^{\text{III}}(\text{PO}_4)_3 \approx \text{Na}_3\text{V}^{\text{III}}\text{V}^{\text{III}}(\text{PO}_4)_3$, respectively, which reflects the stability of the M^{3+} oxidation states of these TMs. The stability of $\text{Na}_3\text{Cr}^{\text{III}}\text{Cr}^{\text{III}}(\text{PO}_4)_3$ is enhanced by the large ligand field stabilization energy of the Cr^{3+} (3d³) cation. The other compounds, $\text{Na}_3\text{Co}^{\text{III}}\text{Co}^{\text{III}}(\text{PO}_4)_3$, $\text{Na}_3\text{Mn}^{\text{III}}\text{Mn}^{\text{III}}(\text{PO}_4)_3$ and $\text{Na}_3\text{Ni}^{\text{III}}\text{Ni}^{\text{III}}(\text{PO}_4)_3$, display shallower (*i.e.*, less favorable) formation energies (<25 meV per atom, Fig. 2a). The shallow convex hulls for $\text{Na}_x\text{Mn}_2(\text{PO}_4)_3$ and $\text{Na}_x\text{Ni}_2(\text{PO}_4)_3$ are caused by the Mn^{3+} and Ni^{3+} ions which are both Jahn–Teller active. The magnetic moment of Co^{3+} $\text{Na}_3\text{Co}^{\text{III}}\text{Co}^{\text{III}}(\text{PO}_4)_3$ is $\sim 3.0 \mu_{\text{B}}$, indicating an intermediate spin state and possible Jahn–Teller activity.

(iv) Unsurprisingly, the deep minima in the convex hull plot of Fig. 2a lead to a large voltage step as shown in Fig. 2b and d, following the sequence $\text{Cr} > \text{Fe} > \text{Ti} > \text{V} > \text{Co} > \text{Mn} > \text{Ni}$.

(v) The $\text{M}(\text{III/II})$ redox couples that correspond to Na contents from $x = 3$ to $x = 4$, follow the voltage trend $\text{Ni} > \text{Co} > \text{Mn} > \text{Fe} > \text{Cr} > \text{V} > \text{Ti}$, while the $\text{M}(\text{IV/III})$ couples ($x = 1$ to $x = 3$) follow the sequence $\text{Ni} > \text{Co} > \text{Fe} > \text{Cr} > \text{Mn} > \text{V} > \text{Ti}$. Thus, Ni and Co (V and Ti) display the highest (lowest) average voltages for both M redox couples.

To validate our methodology, we have benchmarked our results against experimental observations in $\text{Na}_x\text{V}_2(\text{PO}_4)_3$, which has been extensively studied.^{57,60} Experimentally, $\text{Na}_3\text{-V}^{\text{III}}\text{V}^{\text{III}}(\text{PO}_4)_3$ adopts monoclinic symmetry ($C2/c$) at room temperature, which is in qualitative agreement with our DFT calculations identifying the monoclinic ordering (Cc) as the stable structure at $x = 3$. From Fig. 2a, $\text{Na}_3\text{V}^{\text{III}}\text{V}^{\text{III}}(\text{PO}_4)_3$ is on the convex hull with $\text{Na}_1\text{V}^{\text{IV}}\text{V}^{\text{IV}}(\text{PO}_4)$ and $\text{Na}_4\text{V}^{\text{II}}\text{V}^{\text{III}}(\text{PO}_4)_3$, which adopt the rhombohedral space groups $R\bar{3}c$ and $R\bar{3}$, respectively;

this is consistent with X-ray diffraction experiments.^{36,57,61} In Fig. 2b, the extraction of 2 Na atoms from $\text{Na}_3\text{V}^{\text{III}}\text{V}^{\text{III}}(\text{PO}_4)_3$ gives rise to an average voltage of $\sim 2.96 \text{ V}$ vs. Na/Na^+ and corresponds to the $\text{V}^{\text{IV}}/\text{V}^{\text{III}}$ redox couple, while the insertion of Na into $\text{Na}_3\text{-V}^{\text{III}}\text{V}^{\text{III}}(\text{PO}_4)_3$ results in a voltage of 1.54 V (associated with the $\text{V}^{\text{III}}/\text{V}^{\text{II}}$ redox couple). Experimentally, both the V redox couples ($\text{V}^{\text{IV}}/\text{V}^{\text{III}}$ and $\text{V}^{\text{III}}/\text{V}^{\text{II}}$) are involved in two-phase reaction mechanisms, yielding average voltages of $\sim 3.40 \text{ V}$ and $\sim 1.63 \text{ V}$ vs. Na/Na^+ , respectively,⁶⁰ which are in reasonable agreement with our computed values. Notably, both GGA+U and hybrid functionals underestimate the computed voltages of $\text{Na}_x\text{V}_2(\text{PO}_4)_3$ (see Section S2 in the ESI[†]). Another important assessment to verify the validity of our simulations is ensuring that changes in oxidation states of the TMs upon Na extraction/insertion are captured. We verify that the correct redox processes do occur in our calculations by tracking the on-site magnetic moments on the TM atoms (Table S1[†]), as well as the transition metal coordination environments (Table S2[†]), which are discussed in Section S3 of the ESI.[†]

Whenever we could not assign the expected oxidation state of the TMs directly from the computed magnetic moments (*e.g.*, in the cases of Fe, Co and Ni based NaSICONs), we inspected the density of states (DOS). Additional DOSs are reported in Section S4 of the ESI (Fig. S9–S12).[†] As an example, we show in Fig. 3 the total and atom-projected DOS in $\text{Na}_x\text{V}_2(\text{PO}_4)_3$, for $x = 1, 3$ and 4 , which are the ground states identified in Fig. 2. The DOS is displayed for spin up and spin down states in the range of interest (-2.5 to 2 eV) around the Fermi energy. Unless a given structure is metallic, the top of the Fermi energy is arbitrarily set to the top of the valence band.

Panels (a) and (b) in Fig. 3 show the results for $\text{Na}_1\text{-V}^{\text{IV}}\text{V}^{\text{IV}}(\text{PO}_4)_3$ and $\text{Na}_3\text{V}^{\text{III}}\text{V}^{\text{III}}(\text{PO}_4)_3$, respectively. From the projected DOS, the valence bands near the Fermi energy are occupied by 3d electrons of vanadium (red line), while the 2p O states (orange line) lie at lower energies. In general, the vanadium 3d states tend to dominate the valence band and shift at higher energies as more Na is inserted, closing the band gap ($>1 \text{ eV}$ for both compounds). The monoclinic distortion of

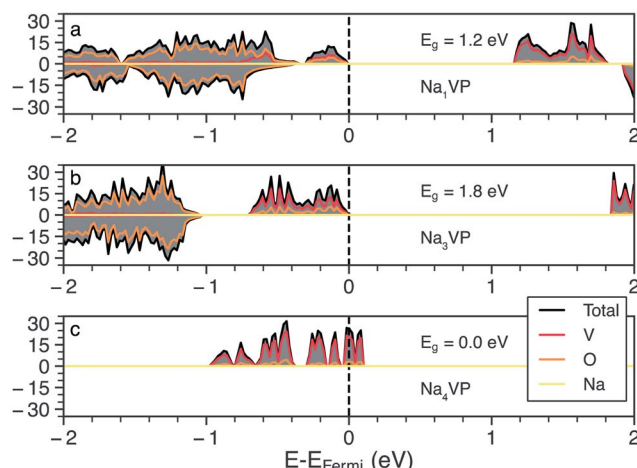


Fig. 3 The total (gray) and atom projected (V red, O orange and Na yellow) DOS of the $\text{Na}_x\text{V}_2(\text{PO}_4)_3$ NaSICON (NVP), where for Na concentrations $x = 1$ (panel a), 3 (panel b) and 4 (panel c). The vertical line denotes the Fermi energy level and E_g is the calculated band gap at the GGA+ U level of theory.

$\text{Na}_3\text{V}^{\text{III}}\text{V}^{\text{III}}(\text{PO}_4)_3$ is responsible for an increase in the band gap (~ 1.8 eV) contrary to the $\text{Na} = 1$ and $\text{Na} = 4$ trends. As expected, the intercalation of more Na^+ ions as in $\text{Na}_4\text{V}^{\text{III}}\text{V}^{\text{II}}(\text{PO}_4)_3$ (Fig. 3c) further increases (destabilizes) the valence band, with this composition becoming gapless and showing a Fermi energy

dominated by V(3d) states when GGA+ U is used. For the $\text{Na}_4\text{V}^{\text{III}}\text{V}^{\text{II}}(\text{PO}_4)_3$, the band gap opens to ~ 0.3 eV when the more accurate HSE06 hybrid functional is used at the relaxed HSE06 structure. Very recent hybrid functional simulations on $\text{Na}_x\text{Ti}_2(\text{PO}_4)_3$ have verified these orders of magnitude, with $\text{Na}_4\text{Ti}^{\text{III}}\text{Ti}^{\text{II}}(\text{PO}_4)_3$ showing a small band gap of ~ 0.59 eV.⁶²

In the case of $\text{Na}_x\text{Ni}_2(\text{PO}_4)_3$ the projected DOS of Fig. S12† suggests metallic behavior at all the Na concentrations explored (*i.e.*, $x = 1, 3$ and 4). $\text{Na}_x\text{Mn}_2(\text{PO}_4)_3$ and $\text{Na}_x\text{Co}_2(\text{PO}_4)_3$ show band gaps > 1.0 eV at $x = 3$ and 4, but become metallic at $x = 1$, as shown in Fig. S9 and S11.† $\text{Na}_1\text{Fe}^{\text{IV}}\text{Fe}^{\text{IV}}(\text{PO}_4)_3$ also appears, surprisingly, metallic (Fig. S10†), which introduces difficulties in localizing the $\text{Fe}^{\text{III}}/\text{Fe}^{\text{IV}}$ redox couple. Therefore, due to the apparent metallic behavior of some of these systems (Fe, Co and Ni-based NaSICONs), we were unable to assign unique oxidation states to their TMs. Notably, DFT is a ground state theory and not adequate in the prediction of accurate band gaps.⁶³

2.3 Na^+ ion intercalation in $\text{Na}_x\text{MM}'(\text{PO}_4)_3$ NaSICON structures

We extend our analysis to the reversible extraction of Na from mixed $\text{Na}_4\text{MM}'(\text{PO}_4)_3$ compounds where, for the sake of simplicity, the ratio $\text{M} : \text{M}'$ is fixed as 1 : 1. While all the $\text{M} : \text{M}'$ combinations have been considered, to simplify our discussion we concentrate on the cases where $\text{M} = \text{Ti}$, while $\text{M}' = \text{Ti}, \text{V}, \text{Cr}, \text{Mn}, \text{Fe}, \text{Co}$ and Ni . Other mixed $\text{Na}_4\text{MM}'(\text{PO}_4)_3$ are reported in

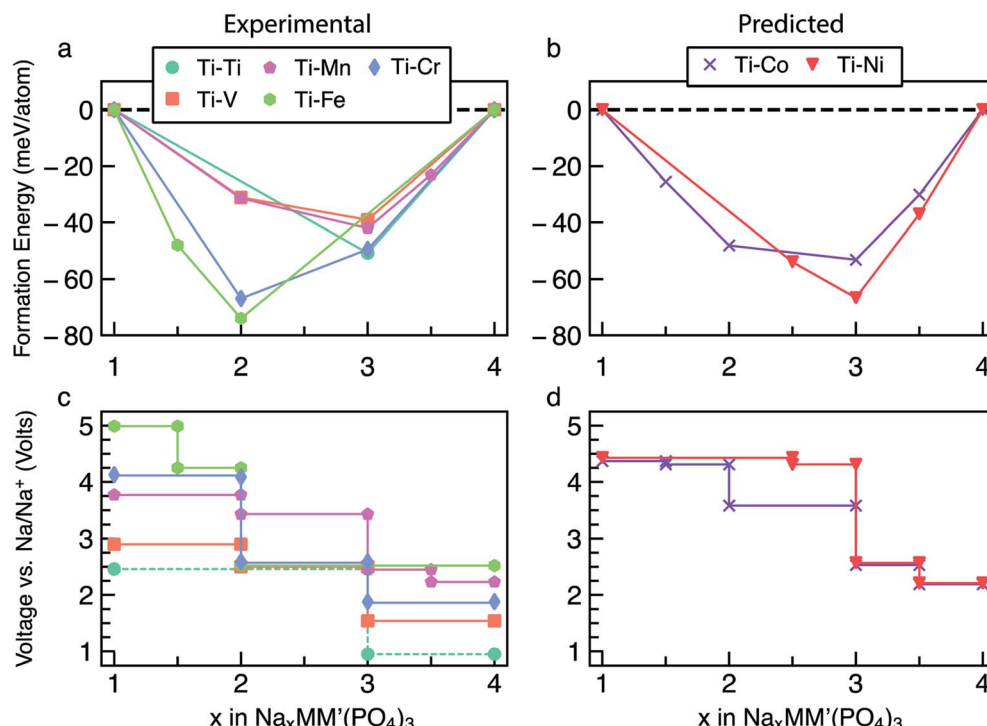


Fig. 4 Panels (a) and (b) show the computed convex hulls as a function of Na concentrations (x) for $\text{Na}_x\text{TiM}'(\text{PO}_4)_3$, where $\text{M}' = \text{Ti}, \text{V}, \text{Cr}, \text{Mn}, \text{Fe}$ in panel (a) and $\text{M}' = \text{Co}$ and Ni in panel (b). Panels (c) and (d) show the corresponding Na (de-)intercalation voltages over changes in the Na-content. The energies of unstable configurations for each convex hull, as well as complete voltage curves for each compound, are given in the ESI (Fig. S13–S33).† The symbols in panels (a) and (b) indicate stable ordered phases. To facilitate the visualization of the voltage curves near ~ 2.8 V vs. Na/Na^+ the $\text{Ti}-\text{Cr}$ curve in panel (c) has been slightly lifted, but it is expected to overlap the $\text{Ti}-\text{V}$ and $\text{Ti}-\text{Mn}$ voltage curves.

Section S5 of the ESI (Fig. S13–S33).[†] The main reason behind choosing Ti-based mixed TM NaSICONs is their maximum experimental electrochemical data availability as compared to other combinations. Fig. 4a and b show the calculated convex hulls for experimentally reported and theoretical $\text{Na}_x\text{TiM}'(\text{PO}_4)_3$ compounds, with Na contents in the range $1 \leq x \leq 4$. Fig. 4c displays the corresponding voltages. $\text{Na}_x\text{Ti}_2(\text{PO}_4)_3$ is also reported in Fig. 4a and c as a reference.

Among the $\text{Na}_x\text{TiM}'(\text{PO}_4)_3$ systems, only $\text{Na}_x\text{Ti}_2(\text{PO}_4)_3$, $\text{Na}_x\text{-TiV}(\text{PO}_4)_3$ and $\text{Na}_x\text{TiMn}(\text{PO}_4)_3$ have been experimentally investigated over the entire Na composition range ($1 \leq x \leq 4$),^{28,48–51} while $\text{Na}_x\text{TiCr}(\text{PO}_4)_3$ (ref. 52 and 64) and $\text{Na}_x\text{TiFe}(\text{PO}_4)_3$ (ref. 52) have been studied in limited ranges of $1 \leq x \leq 3$ and $2 \leq x \leq 4$, respectively. $\text{Na}_x\text{TiCo}(\text{PO}_4)_3$ and $\text{Na}_x\text{TiNi}(\text{PO}_4)_3$ are theoretical compounds and have not yet been reported experimentally.

In general, the end member compositions at $x = 1$ and 4 (Fig. 4a and b) of the Ti–M' NaSICON electrodes adopt rhombohedral symmetry ($R\bar{3}c$ or $R\bar{3}$, or $R\bar{3}2$) except for $\text{Na}_4\text{-Ti}^{\text{III}}\text{Cr}^{\text{II}}(\text{PO}_4)_3$ ($P\bar{1}$) and $\text{Na}_4\text{Ti}^{\text{IV}}\text{Fe}^{\text{IV}}(\text{PO}_4)_3$ ($P1$), which are theoretically derived. This could be due to Jahn–Teller effects caused by the high-spin d⁴ electronic configurations of Cr^{2+} and Fe^{4+} , respectively, as well as the low stability of Fe^{4+} . For $\text{Na}_x\text{-TiM}'(\text{PO}_4)_3$ with $M' = \text{V}, \text{Mn}, \text{Co}$ and Ni , a global minimum in the convex hull is located at $x = 3$, and the magnitudes of the formation energy follow the trend $\text{Ni} > \text{Co} > \text{Mn} > \text{V}$. On the other hand, the global minima for the M' = Ti, Cr and Fe NaSICONs are located at $x = 2$ (Fig. 4a), which is driven by the high stability of their stable oxidation states Ti^{4+} , Cr^{3+} and Fe^{3+} , respectively. Overall, the depth of the convex hulls (*i.e.*, maximum magnitude of formation energies) for mixed TM NaSICONs follows the trend $\text{Fe} > \text{Cr} \sim \text{Ni} > \text{Co} > \text{Ti} > \text{Mn} \sim \text{V}$.

Fig. 4c and d present the computed voltages for Na extraction from $\text{Na}_x\text{TiM}'(\text{PO}_4)_3$ in the composition range $1 \leq x \leq 4$. Expectedly, the compound exhibiting the lowest intercalation voltage (~ 0.96 V) is $\text{Na}_x\text{Ti}_2(\text{PO}_4)_3$ for $3 \leq x \leq 4$, which overestimates the experimental voltage (~ 0.4 V) reported by Senguttuvan *et al.*²⁸ The DFT data of Fig. 4a suggest that an unreported stable phase appears at $\text{Na}_{1.5}\text{TiFe}(\text{PO}_4)_3$, but with an oxidation state for Fe of 3.5 ($\text{Fe}^{\text{IV}} + \text{Fe}^{\text{III}}$). Although the highest Na intercalation voltage (~ 4.99 V) is computed for $\text{Na}_x\text{-TiFe}(\text{PO}_4)_3$ between $x = 1.5$ and $x = 1$, the oxidation state of Fe would have to be +4, which may not be experimentally accessible in a reversible manner. We find that $\text{Na}_1\text{Fe}^{\text{IV}}\text{Fe}^{\text{IV}}(\text{PO}_4)_3$, where iron is expected to be Fe^{4+} appears metallic from the DOS in Fig. S10.[†]

To assess the quality of our computed data, we analyzed in detail the experimentally reported data for $\text{Na}_x\text{TiV}(\text{PO}_4)_3$. At $x = 1, 2$ and 4 , $\text{Na}_x\text{TiV}(\text{PO}_4)_3$ has rhombohedral symmetry ($R\bar{3}c$), while the structure of $\text{Na}_3\text{TiV}(\text{PO}_4)_3$ is monoclinic ($C2/c$).^{48,49} Our calculations reproduce the rhombohedral symmetry ($R\bar{3}c$) at $x = 1$ and 4 and the monoclinic symmetry (Cc) at $x = 3$, whereas we find a triclinic structure ($P\bar{1}$) for $\text{Na}_2\text{TiV}(\text{PO}_4)_3$.⁴⁸ The $\text{Na}_x\text{-TiV}(\text{PO}_4)_3$ convex hull (Fig. 4a) displays a minimum at $x = 3$, analogous to the observed minima in the $\text{Na}_x\text{M}_2(\text{PO}_4)_3$ systems (Fig. 2a); this also provides the largest step in the corresponding voltage profile of Fig. 4c. In particular, the Na extraction from $\text{Na}_4\text{Ti}^{\text{III}}\text{V}^{\text{II}}(\text{PO}_4)_3$ takes place through the redox couples $\text{V}^{\text{III}}/\text{V}^{\text{II}}$

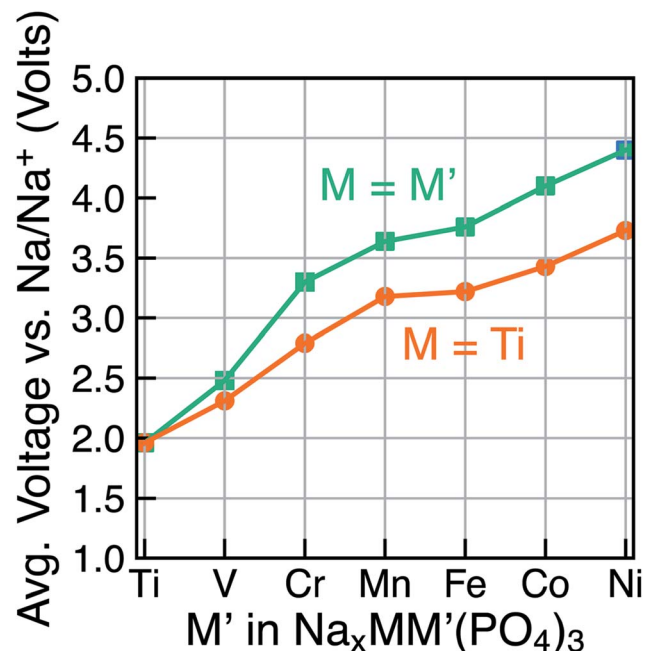


Fig. 5 The calculated average voltage per extracted Na^+ ion vs. Na/Na^+ over the x range^{1–4} in $\text{Na}_x\text{MM}'(\text{PO}_4)_3$ compounds, where $M = M'$ (green) or $M = \text{Ti}$ (orange) and $M' = \text{V}, \text{Cr}, \text{Mn}, \text{Fe}, \text{Co}$ and Ni .

1.54 V (experimentally ~ 1.6 V^{48,49}), $\text{Ti}^{\text{IV}}/\text{Ti}^{\text{III}}$ 2.50 V (~ 2.1 V), and $\text{V}^{\text{IV}}/\text{V}^{\text{III}}$ 2.90 V (~ 3.4 V) vs. Na/Na^+ , respectively. The mechanism of Na extraction from $\text{Na}_4\text{Ti}^{\text{III}}\text{V}^{\text{II}}(\text{PO}_4)_3$ has been shown to occur *via* a solid-solution mechanism for the $\text{V}^{\text{III}}/\text{V}^{\text{II}}$ redox couple, followed by a two-phase reaction for both the $\text{Ti}^{\text{IV}}/\text{Ti}^{\text{III}}$ and $\text{V}^{\text{IV}}/\text{V}^{\text{III}}$ redox couples.⁴⁸

Due to the existence of multiple voltage steps in $\text{Na}_x\text{-MM}'(\text{PO}_4)_3$ (where $M' = \text{Ti}, \text{V}, \text{Cr}, \text{Mn}, \text{Fe}, \text{Co}$ and $M = \text{Ti}$), we directly compare the computed average voltage per Na^+ exchanged over the entire composition range (*i.e.*, $1 \leq x \leq 4$), as shown in Fig. 5. Importantly, the overall average voltage monotonically increases from Ti to Ni in cases where $M = M'$ and $M = \text{Ti}$, which is consistent with trends in standard reduction potentials of the transition metals. We note that the M^{4+} ions, in particular, become more oxidizing as one crosses the transition series from Ti to Ni, with the lack of voltage increase from Mn to Fe reflecting the stability of their 3d⁵ configurations. Specifically, the calculated voltages increase from ~ 1.96 V (for Ti) to ~ 4.40 V vs. Na/Na^+ (for Ni) in $\text{Na}_x\text{M}_2(-\text{PO}_4)_3$ (green line in Fig. 5), while the maximum voltage is ~ 3.73 V for Ti–Ni in the case of $\text{Na}_x\text{MM}'(\text{PO}_4)_3$ ($M = \text{Ti}$) systems (orange line). Notably, the voltage values for $\text{Na}_x\text{-TiM}'(\text{PO}_4)_3$ are consistently lower than those for the corresponding $\text{Na}_x\text{M}'_2(-\text{PO}_4)_3$, indicating that replacing Ti with another 3d metal will always lead to an increased average voltage in both $M = M'$ and $\text{Ti}-\text{M}'$ systems.

2.4 Intercalation voltages of $\text{Na}_x\text{MM}'(\text{PO}_4)_3$

Fig. 6 consolidates the computed voltages of 28 plausible combinations of 3d TMs in $\text{Na}_x\text{MM}'(\text{PO}_4)_3$ with M and M' in a 1 : 1 ratio. In Fig. 6, the boxes outlined in red represent the

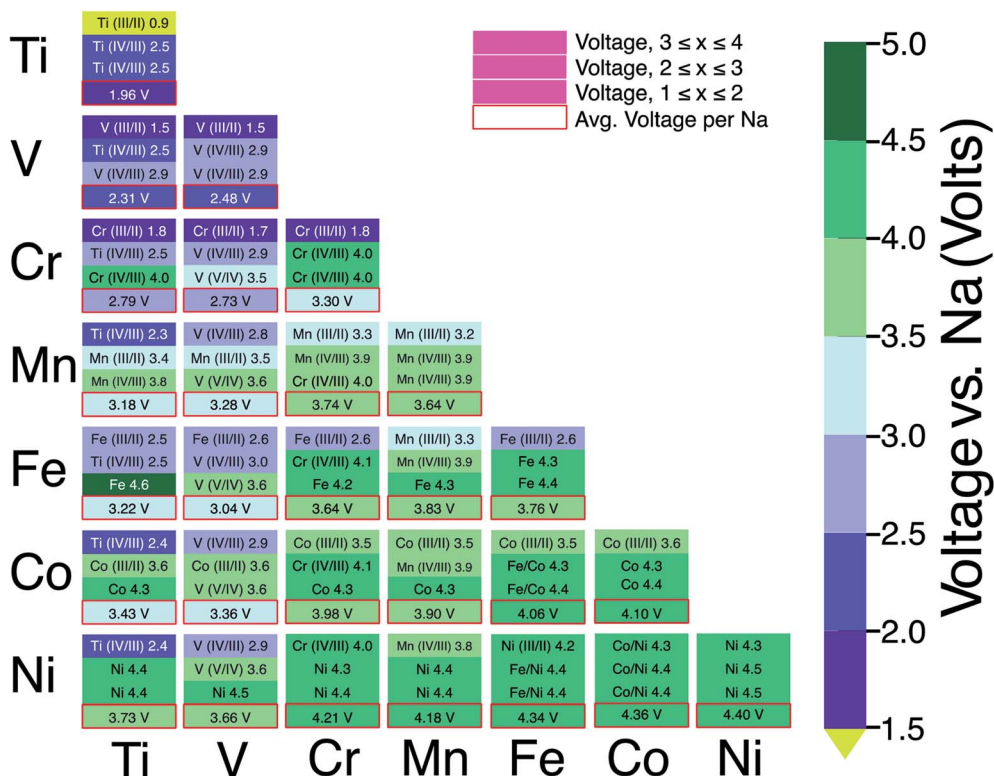


Fig. 6 A voltage map derived from our calculations of 3d NaSICON electrodes, $\text{Na}_x\text{MM}'(\text{PO}_4)_3$, where M and M' = Ti, V, Cr, Mn, Fe, Co and Ni. The text in each box represents the redox pair and the corresponding voltage vs. Na/Na^+ (given by the color bar). The color of the text in the sub-boxes (black or white) does not have any physical significance other than to enhance the visibility of the plot. The color fill in each sub-box represents the voltage from the scale given on the right. The red-outlined bottom sub-box reflects the average voltage per Na in the overall range of $1 \leq x \leq 4$.

average voltage per extracted Na in the entire $1 \leq x \leq 4$ concentration range for each combination of TM. The NaSICON systems investigated cover a range of average voltages from ~ 1.96 to ~ 4.4 V vs. Na/Na^+ . Redox couples are indicated in each box whenever we could identify the appropriate oxidation states as described in Section 2.2. The diagonal of Fig. 6 displays the

single-TM NaSICONs ($M = M'$), whose average voltages map directly to Fig. 5. Notably, the highest average voltages of ~ 4.3 to 4.4 V are attained by the theoretical $Na_xNi_2(PO_4)_3$, $Na_xCoNi(PO_4)_3$ and $Na_xFeNi(PO_4)_3$ compounds. In general, voltages in NaSICONs are set by the redox couples M^{III}/M^{II} and M^{IV}/M^{III} but notable exceptions to this trend are for V and Nb-based

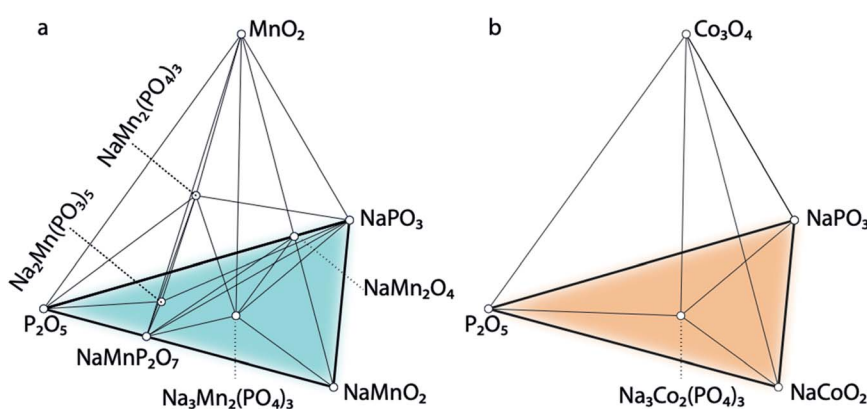


Fig. 7 Panels (a) and (b) show portions of the computed phase diagrams of Na–P–O–Mn and Na–P–O–Co at 0 K. Two stable NaSiCON structures, i.e., $\text{NaMn}_2(\text{PO}_4)_3$ and $\text{Na}_3\text{Mn}_2(\text{PO}_4)_3$, are observed in the phase diagram of Na–P–O–Mn, which are in equilibrium with the highly stable binary (P_2O_5 and MnO_2) and ternary (NaMnO_2 and NaPO_3) compounds. In panel (b), a stable NaSiCON structure, i.e., $\text{Na}_3\text{Co}_2(\text{PO}_4)_3$, is observed in the phase diagram of Na–P–O–Co, which is in equilibrium with the highly stable binary (P_2O_5 and Co_3O_4) and ternary (NaCoO_2 and NaPO_2) compounds.

NaSICONs, which can also operate on the V^V/V^{IV} couple (see the mixed Na_xVM'(PO₄)₃ systems in Fig. 6) and the Nb^V/Nb^{IV} couple in Na_xNbTi(PO₄)₃ not discussed here.⁶⁵

2.5 Thermodynamic stabilities of selected Na_xM₂(PO₄)₃ compounds

The calculated quaternary phase diagrams for the systems Na-P-O-Mn, Na-P-O-Co, and Na-P-O-Ni (Fig. 7 and S34 in the ESI†) reflect the stabilities of the unreported NaSICONs with these transition metals compared with the stable elemental, binary, ternary and quaternary phases. While it remains extremely challenging to characterize quaternary (and beyond) phase diagrams solely based on sparse experimental data, theory provides a viable alternative for investigating such complex systems. We calculated all the binary/ternary/quaternary compounds available in the inorganic crystal structure database (ICSD)⁶⁶ within the Na-P-O-Mn, -Co and -Ni quaternary systems.

Fig. 7a shows the computed phase diagram of the Na-P-O-Mn system, where open circles correspond to stable phases in the global phase diagrams and the black lines show the equilibria among various compounds. The computed phase diagram of Na-Mn-P-O shows that Na₃Mn^{III}Mn^{III}(PO₄)₃ and Na₁Mn^{IV}Mn^{IV}(PO₄)₃ are stable compounds. Na₃Mn^{III}Mn^{III}(PO₄)₃ has the structure of the monoclinic (*Cc*) polymorph, whereas Na₁Mn^{IV}Mn^{IV}(PO₄)₃ has a rhombohedral (*R*³) structure. From our computations, we observed a Jahn-Teller distortion driven by the Mn³⁺ 3d⁴ ions and highlighted by four longer equatorial bonds of ~2.10 Å and two shorter axial bonds of ~1.96 Å. No Ni-containing NaSICON phases appear stable in the Na-Ni-P-O system (Fig. S34†). In the Na-Co-P-O phase diagram (Fig. 7b), only Na₃Co^{III}Co^{III}(PO₄)₃ appears stable and exhibits rhombohedral symmetry (*R*³). From this analysis, it is predicted that Na₃Mn^{III}Mn^{III}(PO₄)₃, Na₁Mn^{IV}Mn^{IV}(PO₄)₃, and Na₃Co^{III}Co^{III}(PO₄)₃ have the potential for successful experimental syntheses, given their thermodynamic stabilities.

Table 1 Experimentally observed Na_xMM'(PO₄)₃ phases along with the corresponding Na concentrations, structures, Na⁺ reversible intercalation voltages, redox couples, mechanism of Na⁺ intercalation, and gravimetric capacities. The intercalation voltages (in V) and theoretical (Theo.) capacities (in mA h g⁻¹) are shown. Rev. and Irrev. indicate experimentally reversible and irreversible processes. ? is used whenever the space group of a specific phase is unknown or not reported. Intercalation voltages account for the number of Na⁺ ions exchanged. Whenever available, the space group of each phase is reported. For a transparent comparison between theoretical and experimentally reported capacities, the reported capacities are renormalized to the molecular weight of Na₄MM'(PO₃)₄. The theoretical capacities (Theo.) are also computed with respect to the Na₄MM'(PO₃)₄ compound

M = M'	x = 1	2	3	4	Reported capacity	Theo. capacity
Ti-Ti ²⁸	?		P ¹	R ³ c	142.7	170.1
V-V ^{37,39}	R ³ c	2.1 V, Ti ^{IV} /Ti ^{III} , Rev.	0.4 V, Ti ^{III} /Ti ^{II} , Irrev.	R ³ c	156.7	167.9
Cr-Cr ⁴⁵	R ³ c	3.4 V, V ^V /V ^{III} , Rev.	1.6 V, V ^{III} /V ^{II} , Irrev.	R ³ c	93.3	111.5
Fe-Fe ^{43,44}	?	4.5 V, Cr ^{IV} /Cr ^{III} , Rev.	C ² /c	R ³ c	85.8	164.6
		3.4 V, Fe ^{IV} /Fe ^{III} , Rev.	2.5 V, Fe ^{III} /Fe ^{II} , Rev.			
M-M'	x = 1	2	3	4	Reported capacity	Theo. capacity
Ti-V ^{48,49}	R ³ c	R ³ c	C ² /c	R ³ c	132.8	169.0
	3.4 V, V ^{IV} /V ^{III} , Rev.	2.1 V, Ti ^{IV} /Ti ^{III} , Rev.	1.6 V, V ^{III} /V ^{II} , Rev.			
Ti-Cr ⁵²	R ³ c	R ³ c	R ³ c		—	112.4
	4.5 V, Cr ^{IV} /Cr ^{III} , Rev.	2.1 V, Ti ^{IV} /Ti ^{III} , Rev.				
Ti-Mn ^{50,51}	R ³ c	R ³ c	R ³ c	?	152.3	167.6
	4. V, Mn ^{IV} /Mn ^{III} , Rev.	3.5 V, Mn ^{III} /Mn ^{II} , Rev.	2.1 V, Ti ^{IV} /Ti ^{III} , Rev.			
Ti-Fe ⁵²		R ³ c	R ³ c	R ³ c	—	111.5
		2.4 V, Fe ^{III} /Fe ^{II} , Rev.	2.1 V, Ti ^{IV} /Ti ^{III} , Rev.			
V-Cr ⁴⁷	?	?	R ³ c		85.7	111.7
	4.1 V, V ^V /V ^{IV} , Rev.	3.4 V, V ^{IV} /V ^{III} , Rev.				
V-Mn ^{34,54,56}	R ³ c	R ³ c	R ³ c	R ³ c	156.0	166.6
	3.9 V, V ^V /V ^{IV} , Irrev.	3.6 V, Mn ^{III} /Mn ^{II} , Rev.	3.4 V, V ^V /V ^{III} , Rev.			
V-Fe ^{29,35}		?	C ² /c	?	98.1	110.8
		3.3 V, V ^{IV} /V ^{III} , Rev.	2.5 V, Fe ^{III} /Fe ^{II} , Rev.			
V-Ni ³⁵		?	?	R ³ c	80.0	110.2
		3.9 V, V ^V /V ^{IV} : Ni ^{III} /Ni ^{II} , Rev.	3.5 V, V ^{IV} /V ^{III} , Rev.			
Cr-Mn ^{30,46}	R ³ c	R ³ c	R ³ c	R ³ c	160.5	166.2
	4.4 V, Cr ^{IV} /Cr ^{III} , Rev.	4.2 V, Mn ^{IV} /Mn ^{III} , Rev.	3.6 V, Mn ^{III} /Mn ^{II} , Rev.			

3. Discussion

Using first-principles calculations, we investigated the electrochemical properties of 28 transition-metal-based NaSICONs as cathode materials for NIBs. To guide our discussion, we summarize the reported experimental voltages and the experimental gravimetric and the theoretical gravimetric capacities of some $\text{Na}_x\text{MM}'(\text{PO}_4)_3$ systems in Table 1. For a transparent and fair comparison between the theoretical and experimentally reported capacities in Table 1, the reported capacities are renormalized from the reported composition (pristine) to the molecular weight of the $\text{Na}_4\text{MM}'(\text{PO}_4)_4$. The theoretical capacities are also computed with respect to the $\text{Na}_4\text{MM}'(\text{PO}_4)_4$ compounds.

Among the $\text{Na}_x\text{M}_2(\text{PO}_4)_3$ compounds, $\text{Na}_x\text{Cr}_2(\text{PO}_4)_3$ delivers the highest measured voltage of ~ 4.5 V (~ 4 V calculated theoretically) vs. Na/Na^+ ,⁴⁵ albeit with a limited capacity of just $\sim 98 \text{ mA h g}^{-1}$ and corresponding to the extraction of 2 Na from $\text{Na}_3\text{Cr}^{\text{III}}\text{Cr}^{\text{III}}(\text{PO}_4)_3$ to form $\text{Na}_1\text{Cr}^{\text{IV}}\text{Cr}^{\text{III}}(\text{PO}_4)_3$. $\text{Na}_4\text{Cr}_2(\text{PO}_4)_3$ has not yet been obtained by either a chemical or an electrochemical process. $\text{Na}_4\text{Cr}^{\text{III}}\text{Cr}^{\text{II}}(\text{PO}_4)_3$ would require Cr to exist in a mixed, $\text{Cr}^{\text{III}}/\text{Cr}^{\text{II}}$ oxidation state, with Cr^{2+} (high-spin d⁴) typically being an unstable oxidation state for Cr and easily prone to Jahn–Teller distortions in octahedral environments, *e.g.*, NaSICON.⁶⁷

$\text{Na}_x\text{V}_2(\text{PO}_4)_3$ exhibits the 2nd highest measured voltage of the single TM NaSICONs, with a computed average voltage of ~ 2.48 V vs. Na/Na^+ (Fig. 5). With the same number of maximum electrons exchanged in $\text{Na}_x\text{M}_2(\text{PO}_4)_3$ (where M = Ti or V), and Ti being lighter than V, $\text{Na}_x\text{Ti}_2(\text{PO}_4)_3$ is expected to show the largest gravimetric capacity. $\text{Na}_x\text{Ti}_2(\text{PO}_4)_3$ and NVP provide the largest reported theoretical gravimetric capacities ($\sim 170.1 \text{ mA h g}^{-1}$ and $\sim 167.9 \text{ mA h g}^{-1}$ for $\text{Na}_4\text{M}_2(\text{PO}_4)_3$) in single TM NaSICONs. In theory, additional capacity and an increased voltage could be achieved by exploiting the $\text{V}^{\text{V}}/\text{V}^{\text{IV}}$ redox couple in the reaction $\text{Na}_1\text{V}^{\text{IV}}\text{V}^{\text{IV}}(\text{PO}_4)_3 \rightarrow \text{Na}^+ + 1\text{e}^- \text{V}^{\text{V}}\text{V}^{\text{IV}}(\text{PO}_4)_3$. While the seminal report by Gopalakrishnan *et al.* suggested the possibility of chemically extracting the last Na^+ ion to form $\text{V}^{\text{V}}\text{V}^{\text{IV}}(\text{PO}_4)_3$,⁶⁸ subsequent attempts to do so have proven unsuccessful. Note that $\text{V}^{\text{V}}\text{V}^{\text{IV}}(\text{PO}_4)_3$ is not a thermodynamically stable compound⁶⁹ and is predicted to decompose into $\text{VPO}_5 + \text{VP}_2\text{O}_7$.

We assessed the existence of uncharted single-TM NaSICONs, which are Ni, Co and Mn. Except for $\text{Na}_1\text{Mn}^{\text{IV}}\text{Mn}^{\text{IV}}(\text{PO}_4)_3$, $\text{Na}_3\text{Mn}^{\text{III}}\text{Mn}^{\text{III}}(\text{PO}_4)_3$ and $\text{Na}_3\text{Co}^{\text{III}}\text{Co}^{\text{III}}(\text{PO}_4)_3$ that appear stable according to our convex hulls but have not been reported experimentally, our analysis of the phase diagrams indicates that Ni- and Co-NaSICONs are generally unstable. However, Mn has been mixed effectively with Ti, V and Cr, while Ni–V mixed NaSICONs have also been made (Table 1).³⁴ In particular, Zhou *et al.*³⁵ and later Chen and collaborators³⁴ synthesized Mn^{II} -containing $\text{Na}_4\text{Mn}^{\text{IV}}\text{V}^{\text{III}}(\text{PO}_4)_3$, which upon Na extraction exploits the $\text{Mn}^{\text{III}}/\text{Mn}^{\text{II}}$ redox couple and Mn^{3+} 3d⁴ is Jahn–Teller active.

In the case of mixed $\text{Na}_4\text{MM}'(\text{PO}_4)_3$ NaSICONs, we kept the M : M' ratio to 1 : 1. From an extensive assessment of polyanion

electrodes, Masquelier and Crouguennec¹⁷ observed that the redox potentials of specific TMs remain nearly independent⁷⁰ of those of other TMs that may be present. This general rule is also well supported by the simulations that are summarized in Fig. 6. Based on this general principle, one can envision selected combinations of TMs delivering reversible high voltages vs. Na/Na^+ . For example, the $\text{Ti}^{\text{IV}}/\text{Ti}^{\text{III}}$ redox couple showed a similar voltage¹⁷ (~ 2.1 V vs. Na/Na^+) in three related NaSICON systems: $\text{Na}_x\text{Ti}_2(\text{PO}_4)_3$, $\text{Na}_x\text{TiNb}(\text{PO}_4)_3$ and $\text{Na}_x\text{TiFe}(\text{PO}_4)_3$. Notably, in experiments, there is a consistent shift of ~ 0.3 V between the voltages measured vs. Na/Na^+ compared to those measured vs. Li/Li^+ .

The $\text{Na}_x\text{TiV}(\text{PO}_4)_3$ system has been shown to provide the largest gravimetric capacity ($\sim 187.1 \text{ mA h g}^{-1}$, Table 1) among NaSICONs as a result of the accessibility of several $\text{V}^{\text{IV}}/\text{V}^{\text{III}}/\text{V}^{\text{II}}$ and $\text{Ti}^{\text{IV}}/\text{Ti}^{\text{III}}$ redox couples. Nevertheless, the computed average voltage (~ 2.3 V, Fig. 6) of $\text{Na}_x\text{TiV}(\text{PO}_4)_3$ highlights the low energy density of the system.^{48,49} More promising in terms of overall capacities and voltages, and thus energy density, are $\text{Na}_x\text{TiCr}(\text{PO}_4)_3$,^{52,64} $\text{Na}_x\text{TiMn}(\text{PO}_4)_3$,^{50,51} $\text{Na}_x\text{CrMn}(\text{PO}_4)_3$,^{30,46} $\text{Na}_x\text{VCr}(\text{PO}_4)_3$,⁴⁷ and $\text{Na}_x\text{VMn}(\text{PO}_4)_3$,^{34,54} but the reversible extraction/insertion of Na from some of these systems remains to be verified. Excluding some specific exceptions, especially Fe, Co and Ni based NaSICONs since they appear metallic, our simulations are also able to capture the mechanism of Na intercalation in mixed NaSICON electrodes. For example, $\text{Na}_3\text{VFe}(\text{PO}_4)_3$ has been reported to reversibly insert Na with the activation of the $\text{Fe}^{\text{III}}/\text{Fe}^{\text{II}}$ and $\text{V}^{\text{III}}/\text{V}^{\text{II}}$ redox couples (see Table 1),³⁵ and this behavior is reproduced by our calculations (Fig. 6 and S21 of the ESI†). Similar conclusions can be advanced for mixed TiV, TiCr, VCr and CrMn NaSICON materials.

From our analysis (Fig. 6), specific unexplored combinations of TMs appear to be worthy of future study. Our calculations suggest promising NaSICON compositions in terms of average voltages, such as TiCo, VCo, CrFe and CrCo NaSICONs as reported in Fig. 5 and Table 1. Both CrFe and CrCo NaSICONs are predicted to exploit the high voltage $\text{Cr}^{\text{IV}}/\text{Cr}^{\text{III}}$ redox couple, which has been proven effective in other mixed NaSICONs, *e.g.*, TiCr, VCr and MnCr.^{47,64} Although the addition of Co into Ti, V and Cr appears interesting, our analysis of the $\text{Na}_x\text{Co}_2(\text{PO}_4)_3$ system suggests that only $\text{Na}_3\text{Co}^{\text{III}}\text{Co}^{\text{III}}(\text{PO}_4)_3$ with Co^{3+} 3d⁶ (low spin) is thermodynamically stable, but this compound has not yet been synthesized. While one would target compounds with Co^{2+} to ensure high voltages, it appears possible to introduce Co in smaller proportions⁷¹ than a 1 : 1 ratio, but more experimental and theoretical work is required.

We do not anticipate Ni to be of importance in mixed NaSICON systems due to the high instability of quaternary $\text{Na}_x\text{Ni}_2(\text{PO}_4)_3$. Manoun *et al.*⁷² briefly reported the synthesis of $\text{Na}_4\text{Cr}^{\text{III}}\text{Ni}^{\text{II}}(\text{PO}_4)_3$. A recent report by Zhou *et al.*³⁵ claimed the extraction of Na from $\text{Na}_x\text{VNi}(\text{PO}_4)_3$ (Table 1) involving the redox couples $\text{V}^{\text{V}}/\text{V}^{\text{III}}$, $\text{V}^{\text{V}}/\text{V}^{\text{IV}}$, and $\text{Ni}^{\text{III}}/\text{Ni}^{\text{II}}$. Nevertheless, we speculate that the Ni content of the materials is not in a 1 : 1 ratio but appears to be significantly lower. Furthermore, the highest voltage accessed (< 4.3 V vs. Na/Na^+) during the electrochemical cycling is lower than that of the expected Ni redox couple. While our DFT calculations seem to verify the activity of the $\text{V}^{\text{V}}/\text{V}^{\text{III}}$ and $\text{V}^{\text{V}}/\text{V}^{\text{IV}}$ redox couples in $\text{Na}_x\text{VNi}(\text{PO}_4)_3$ (Fig. 6), we are unable to verify the oxidation states involved in the

$\text{Ni}^{\text{III}}/\text{Ni}^{\text{II}}$ reaction from the computed magnetic moments as the material becomes metallic in our simulations (Fig. S12†). Our findings also cast doubt on the activity of Ni in this compound as reflected by the limited gravimetric capacity reported experimentally ($\sim 80 \text{ mA h g}^{-1}$).³⁵

4. Conclusions

Using *ab initio* density functional theory and thermodynamics, we explored the full chemical map of 3d TM-based NaSICON phosphate $\text{Na}_x\text{MM}'(\text{PO}_4)_3$ (M, M' = Ti, V, Cr, Mn, Fe, Co and Ni) cathode materials for high-energy density and safe sodium-ion batteries. We identified the ground state structures at various Na contents as well as the corresponding Na-intercalation voltages and redox processes for 28 distinct NaSICON compositions of which only 13 have been reported experimentally.

Further, we investigated the Na-intercalation properties of previously unreported $\text{Na}_x\text{Mn}_2(\text{PO}_4)_3$ and $\text{Na}_x\text{VCo}(\text{PO}_4)_3$ ($1 \leq x \leq 4$), among others. The calculated quaternary phase diagrams of the Na-P-O-M (M = Mn, Co and Ni) chemical systems indicate the instability of Ni and most Co-based NaSICONs, though the $\text{Na}_1\text{Mn}^{\text{IV}}\text{Mn}^{\text{IV}}(\text{PO}_4)_3$, $\text{Na}_3\text{Mn}^{\text{III}}\text{Mn}^{\text{III}}(\text{PO}_4)_3$ and $\text{Na}_3\text{-Co}^{\text{III}}\text{Co}^{\text{III}}(\text{PO}_4)_3$ compounds are identified as stable compositions. We performed a complete analysis of the wide-ranging chemical space of NaSICON phosphate cathode materials for Na-ion batteries, and our work can be used to guide further experimental synthesis of the new and promising compositions identified here. We plan to synthesize the promising electrode compositions identified in this work.

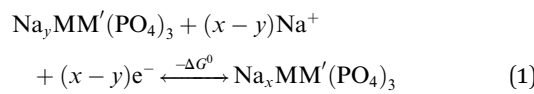
5. Methodology

We used the Vienna *ab initio* simulation package (VASP)^{73,74} for *ab initio* density functional theory (DFT) total energy calculations. The projector augmented wave (PAW) potentials were used for the core wave-functions. The Perdew–Burke–Ernzerhof (PBE) parameterized spin-polarized generalized gradient approximation (GGA) was used for the exchange and correlation energy.⁷⁵ The strong on-site coulomb correlation of 3d electrons of the TM (Ti, V, Cr, Mn, Fe, Co and Ni) is addressed with Hubbard's *U* correction⁷⁶ according to the Dudarev method.⁷⁷ The effective *U* parameters used were 4.0 eV for Ti,²⁸ 3.1 for V, 3.5 for Cr, 3.9 for Mn, 4.0 for Fe, 3.4 for Co, and 6.0 for Ni,⁷⁸ and they were fitted to match the experimental formation energies of binary oxides. We also introduced an empirical correction of 1.36 eV per O_2 (ref. 79) to remedy the spurious error originating from the well-known over-binding of O while using GGA.

The periodic wave functions were expanded in terms of plane waves up to a kinetic energy cut-off of 520 eV. The PAW potentials used to describe the core electrons of the following atomic species were: Na 08Apr2002 3s¹, P 17Jan2003 2s²3p³, O 08Apr2002 2s²2p⁴, Ti 08Apr2002 3d³4s¹, V_pv 07Sep2000 3p⁶3d⁴4s¹, Cr 06Sep2000 3d⁵4s¹, Mn 06Sep2000 3d⁶4s¹, Fe 06Sep2000 3d⁷4s¹, Co 06Sep2000 3d⁸4s¹, and Ni 06Sep2000 3d⁹4s¹. Additionally, a Γ -centered Monkhorst–Pack⁸⁰ *k*-point mesh with 25 subdivisions along each reciprocal lattice vector was applied to all structures. Using these settings, the total

energy of each structure was converged to within 10^{-5} eV per cell, atomic forces within 10^{-2} eV per Å and the stress within 0.29 GPa.

An intercalation battery based on the NaSICON cathode electrodes implies the reversible insertion/extraction of Na^+ -ions into/from the $\text{Na}_y\text{MM}'(\text{PO}_4)_3$ framework according to the redox reaction of eqn (1).



where y and x are the initial and final Na concentration in the NaSICON framework and ΔG^0 is the change of Gibbs energy at 0 K for the reaction of eqn (1). Here, we approximated the Gibbs energy of each component by the DFT total energies (*i.e.*, $G \approx E$), thus neglecting the pV and entropic contributions. The average voltage across an intercalation extent ($x - y$) can be calculated from the ΔG^0 , as in eqn (2).

$$\begin{aligned} V &= -\frac{\Delta G^0}{(x-y)F} \\ &= -\frac{E(\text{Na}_x\text{MM}'(\text{PO}_4)_3) - [E(\text{Na}_y\text{MM}'(\text{PO}_4)_3) + (x-y)\mu_{\text{Na}}]}{(x-y)F} \end{aligned} \quad (2)$$

where μ_{Na} is the Na chemical potential (set to bulk Na metal) and F is the Faraday constant.

To establish the general phase behavior of Na (de)intercalation into the $\text{Na}_y\text{MM}'(\text{PO}_4)_3$ structure, we monitored, using eqn (3), the formation energies ($E_f(x)$) of various Na/vacancy orderings at different Na concentrations, x ($1 \leq x \leq 4$), with respect to the DFT energies of the fully discharged (*i.e.*, $E[\text{Na}_4\text{-MM}'(\text{PO}_4)_3]$) and fully charged ($E[\text{NaMM}'(\text{PO}_4)_3]$) configurations.

$$\begin{aligned} E_f(x) &= E[\text{Na}_x\text{MM}'(\text{PO}_4)_3] - \left(\frac{4-x}{3}\right)E[\text{Na}_1\text{MM}'(\text{PO}_4)_3] \\ &\quad - \left(\frac{x-1}{3}\right)E[\text{Na}_4\text{MM}'(\text{PO}_4)_3]. \end{aligned} \quad (3)$$

Different NaSICON structures were studied according to specific Na concentrations in $\text{Na}_x\text{MM}'(\text{PO}_4)_3$ with M and M' = Ti, V, Cr, Mn, Fe, Co, and Ni. In choosing the amount of mixing of TM in these NaSICON structures, we have considered only two distinct situations: (i) M = M', which leads to $\text{Na}_x\text{M}_2(\text{PO}_4)_3$, and (ii) M and M' in the ratio 1 : 1.

When fully sodiated, the fully ordered rhombohedral symmetry ($R\bar{3}c$) of the high temperature NaSICON structure is typically observed (*e.g.*, $\text{Na}_4\text{Fe}^{\text{III}}\text{Fe}^{\text{II}}(\text{PO}_4)_3$ (ref. 59)) and is therefore our starting model to study Na removal and TM mixing. Na vacancies are created in the fully sodiated structure $\text{Na}_4\text{MM}'(\text{PO}_4)_3$, resulting in $\text{Na}_x\text{MM}'(\text{PO}_4)_3$, where the Na content varies in the range of $1 \leq x \leq 4$ in steps of $\Delta x = 0.5$. The possible configurations originating from the various orderings of Na and vacancies (Va) in the NaSICON are obtained using the pymatgen library.⁸¹ A ranking according to the classical Ewald energy⁸² based on integer charges (*i.e.*, Na = +1, P = +5, O = −2)

and the variable charge on the TM (+2, +3 and +4) is applied to limit the number of possible structures to a computationally tractable level. For mixed TM NaSICONs, the ordering of M and M' is simultaneously performed with that of Na and Va. DFT calculations are performed on the primitive cell and supercells ($2 \times 1 \times 1$) of these orderings. A formula unit of the fully discharged NaSICON ($\text{Na}_4\text{MM}'(\text{PO}_4)_3$) contains 21 atoms.

Conflicts of interest

There are no conflicts to declare.

Acknowledgements

P. C., C. M., A. K. C., and J.-N. C. are grateful to the ANR-NRF NRF2019-NRF-ANR073 Na-MASTER. P. C. and B. S. acknowledge funding from the National Research Foundation under the NRF Fellowship NRFF12-2020-0012. L. C., D. C. and C. M. acknowledge the ANRT and TIAMAT for the funding of S. P.'s PhD thesis as well as the financial support from the Région Nouvelle Aquitaine and from the French National Research Agency (STORE-EX Labex Project ANR-10-LABX-76-01). The computational work was performed using resources of the National Supercomputing Centre, Singapore (<https://www.nscc.sg>).

References

- 1 E. A. Olivetti, G. Ceder, G. G. Gaustad and X. Fu, *Joule*, 2017, **1**, 229.
- 2 J. M. Tarascon, *Nat. Chem.*, 2010, **2**, 510.
- 3 D. Larcher and J. M. Tarascon, *Nat. Chem.*, 2015, **7**, 19.
- 4 S. W. Kim, D. H. Seo, X. Ma, G. Ceder and K. Kang, *Adv. Energy Mater.*, 2012, **2**, 710.
- 5 V. Palomares, P. Serras, I. Villaluenga, K. B. Hueso, J. Carretero-González and T. Rojo, *Energy Environ. Sci.*, 2012, **5**, 5884.
- 6 J. L. Kaufman, J. Vinckevičiūtė, S. K. Kolli, J. G. Goiri and A. Van Der Ven, *Philos. Trans. R. Soc., A*, 2019, **377**, 20190020.
- 7 Q. Bai, L. Yang, H. Chen and Y. Mo, *Adv. Energy Mater.*, 2018, **8**, 1.
- 8 A. Mukherjee, T. Sharabani, R. Sharma, S. Okashy and M. Noked, *Batteries Supercaps*, 2020, **3**, 510.
- 9 N. Yabuuchi, K. Kubota, M. Dahbi and S. Komaba, *Chem. Rev.*, 2014, **114**, 11636.
- 10 I. Hasa, S. Mariyappan, D. Saurel, P. Adelhelm, A. Y. Koposov, C. Masquelier, L. Croguennec and M. Casas-Cabanas, *J. Power Sources*, 2021, **482**, 228872.
- 11 S. H. Bo, X. Li, A. J. Toumar and G. Ceder, *Chem. Mater.*, 2016, **28**, 1419.
- 12 J.-M. Tarascon, *Joule*, 2020, **4**, 1613–1620.
- 13 K. Kubota, T. Asari, H. Yoshida, N. Yaabuuchi, H. Shiiba, M. Nakayama and S. Komaba, *Adv. Funct. Mater.*, 2016, **26**, 6047.
- 14 P. F. Wang, Y. You, Y. X. Yin and Y. G. Guo, *Adv. Energy Mater.*, 2018, **8**, 1701912.
- 15 J. L. Kaufman and A. Van der Ven, *Phys. Rev. Mater.*, 2019, **3**, 015402.
- 16 T. Jin, H. Li, K. Zhu, P. F. Wang, P. Liu and L. Jiao, *Chem. Soc. Rev.*, 2020, **49**, 2342.
- 17 C. Masquelier and L. Croguennec, *Chem. Rev.*, 2013, **113**, 6552.
- 18 S. C. Chung, J. Ming, L. Lander, J. Lu and A. Yamada, *J. Mater. Chem. A*, 2018, **6**, 3919.
- 19 P. Barpanda, G. Oyama, S. Nishimura, S.-C. Chung and A. Yamada, *Nat. Commun.*, 2014, **5**, 4358.
- 20 H. Y. P. Hong, *Mater. Res. Bull.*, 1976, **11**, 173.
- 21 J. B. Goodenough, H. Y. P. Hong and J. A. Kafalas, *Mater. Res. Bull.*, 1976, **11**, 203.
- 22 Q. Ma, C. L. Tsai, X. K. Wei, M. Heggen, F. Tietz and J. T. S. Irvine, *J. Mater. Chem. A*, 2019, **7**, 7766.
- 23 Z. Jian, Y. S. Hu, X. Ji and W. Chen, *Adv. Mater.*, 2017, **29**, DOI: 10.1002/adma.201601925.
- 24 R. V. Panin, O. A. Drozhzhin, S. S. Fedotov, N. R. Khasanova and E. V. Antipov, *Electrochim. Acta*, 2018, **289**, 168.
- 25 C. Delmas, F. Cherkaoui, A. Nadiri and P. Hagenmuller, *Mater. Res. Bull.*, 1987, **22**, 631.
- 26 C. Delmas, A. Nadiri and J. L. Soubeyroux, *Solid State Ionics*, 1988, **28–30**, 419.
- 27 X. Zhang, X. Rui, D. Chen, H. Tan, D. Yang, S. Huang and Y. Yu, *Nanoscale*, 2019, **11**, 2556.
- 28 P. Senguttuvan, G. Rousse, M. E. Arroyo y de Dompablo, H. Vezin, J.-M. Tarascon and M. R. Palacín, *J. Am. Chem. Soc.*, 2013, **135**, 3897.
- 29 B. M. de Boisse, J. Ming, S. Nishimura and A. Yamada, *J. Electrochem. Soc.*, 2016, **163**, A1469.
- 30 J. Wang, Y. Wang, D. Seo, T. Shi, S. Chen, Y. Tian, H. Kim and G. Ceder, *Adv. Energy Mater.*, 2020, **10**, 1903968.
- 31 D. A. Stevens and J. R. Dahn, *J. Electrochem. Soc.*, 2000, **147**, 1271.
- 32 M. Dahbi, M. Kiso, K. Kubota, T. Horiba, T. Chafik, K. Hida, T. Matsuyama and S. Komaba, *J. Mater. Chem. A*, 2017, **5**, 9917.
- 33 H. Kim, J. Hong, G. Yoon, H. Kim, K.-Y. Park, M.-S. Park, W.-S. Yoon and K. Kang, *Energy Environ. Sci.*, 2015, **8**, 2963.
- 34 F. Chen, V. M. Kovrugin, R. David, O. Mentré, F. Fauth, J. Chotard and C. Masquelier, *Small Methods*, 2019, **3**, 1800218.
- 35 W. Zhou, L. Xue, X. Lü, H. Gao, Y. Li, S. Xin, G. Fu, Z. Cui, Y. Zhu and J. B. Goodenough, *Nano Lett.*, 2016, **16**, 7836.
- 36 X. Yao, Z. Zhu, Q. Li, X. Wang, X. Xu, J. Meng, W. Ren, X. Zhang, Y. Huang and L. Mai, *ACS Appl. Mater. Interfaces*, 2018, **10**, 10022.
- 37 K. Saravanan, C. W. Mason, A. Rudola, K. H. Wong and P. Balaya, *Adv. Energy Mater.*, 2013, **3**, 444.
- 38 Y. Uebou, T. KiyabuI, S. Okada and J. Yamaki, *Rep. Inst. Adv. Mater. Study, Kyushu Univ.*, 2002, **16**, 1.
- 39 F. Lalère, J. B. Leriche, M. Courty, S. Boulineau, V. Viallet, C. Masquelier and V. Seznec, *J. Power Sources*, 2014, **247**, 975.
- 40 Y. Noguchi, E. Kobayashi, L. S. Plashnitsa, S. Okada and J. I. Yamaki, *Electrochim. Acta*, 2013, **101**, 59.

- 41 Z. Deng, G. Sai Gautam, S. K. Kolli, J.-N. Chotard, A. K. Cheetham, C. Masquelier and P. Canepa, *Chem. Mater.*, 2020, **32**, 7908.
- 42 J. Kang, S. Baek, V. Mathew, J. Gim, J. Song, H. Park, E. Chae, A. K. Rai and J. Kim, *J. Mater. Chem.*, 2012, **22**, 20857.
- 43 Y. Liu, Y. Zhou, J. Zhang, Y. Xia, T. Chen and S. Zhang, *ACS Sustainable Chem. Eng.*, 2017, **5**, 1306.
- 44 R. Rajagopalan, B. Chen, Z. Zhang, X.-L. Wu, Y. Du, Y. Huang, B. Li, Y. Zong, J. Wang, G.-H. Nam, M. Sindoro, S. X. Dou, H. K. Liu and H. Zhang, *Adv. Mater.*, 2017, **29**, 1605694.
- 45 K. Kawai, W. Zhao, S. Nishimura and A. Yamada, *ACS Appl. Energy Mater.*, 2018, **1**, 928.
- 46 W. Zhang, H. Li, Z. Zhang, M. Xu, Y. Lai and S. L. Chou, *Small*, 2020, **16**, 2001524.
- 47 R. Liu, G. Xu, Q. Li, S. Zheng, G. Zheng, Z. Gong, Y. Li, E. Kruskop, R. Fu, Z. Chen, K. Amine and Y. Yang, *ACS Appl. Mater. Interfaces*, 2017, **9**, 43632.
- 48 F. Lalère, V. Seznec, M. Courty, J. N. Chotard and C. Masquelier, *J. Mater. Chem. A*, 2018, **6**, 6654.
- 49 D. Wang, X. Bie, Q. Fu, D. Dixon, N. Bramnik, Y. S. Hu, F. Fauth, Y. Wei, H. Ehrenberg, G. Chen and F. Du, *Nat. Commun.*, 2017, **8**, 1.
- 50 T. Zhu, P. Hu, X. Wang, Z. Liu, W. Luo, K. A. Owusu, W. Cao, C. Shi, J. Li, L. Zhou and L. Mai, *Adv. Energy Mater.*, 2019, **9**, 2.
- 51 H. Gao, Y. Li, K. Park and J. B. Goodenough, *Chem. Mater.*, 2016, **28**, 6553.
- 52 S. Patoux, G. Rousse, J. B. Leriche and C. Masquelier, *Chem. Mater.*, 2003, **15**, 2084.
- 53 H. Li, T. Jin, X. Chen, Y. Lai, Z. Zhang, W. Bao and L. Jiao, *Adv. Energy Mater.*, 2018, **8**, 1801418.
- 54 S. Ghosh, N. Barman, M. Mazumder, S. K. Pati, G. Rousse and P. Senguttuvan, *Adv. Energy Mater.*, 2020, **10**, 1902918.
- 55 M. V. Zakharkin, O. A. Drozhzhin, I. V. Tereshchenko, D. Chernyshov, A. M. Abakumov, E. V. Antipov and K. J. Stevenson, *ACS Appl. Energy Mater.*, 2018, **1**, 5842.
- 56 M. V. Zakharkin, O. A. Drozhzhin, S. V. Ryazantsev, D. Chernyshov, M. A. Kirsanova, I. V. Mikheev, E. M. Pazhetnov, E. V. Antipov and K. J. Stevenson, *J. Power Sources*, 2020, **470**, 228231.
- 57 J. N. Chotard, G. Rousse, R. David, O. Mentré, M. Courty and C. Masquelier, *Chem. Mater.*, 2015, **27**, 5982.
- 58 H. Kabour, D. Coillot, M. Colmont, C. Masquelier and O. Mentré, *J. Am. Chem. Soc.*, 2011, **133**, 11900.
- 59 F. Hatert, *Acta Crystallogr., Sect. E: Struct. Rep. Online*, 2009, **65**, i30.
- 60 F. Lalère, V. Seznec, M. Courty, R. David, J. N. Chotard and C. Masquelier, *J. Mater. Chem. A*, 2015, **3**, 16198.
- 61 Z. Jian, C. Yuan, W. Han, X. Lu, L. Gu, X. Xi, Y. S. Hu, H. Li, W. Chen, D. Chen, Y. Ikuhara and L. Chen, *Adv. Funct. Mater.*, 2014, **24**, 4265.
- 62 D. Gryaznov, S. K. Stauffer, E. A. Kotomin and L. Vilčiauskas, *Phys. Chem. Chem. Phys.*, 2020, **22**, 11861.
- 63 M. K. Y. Chan and G. Ceder, *Phys. Rev. Lett.*, 2010, **105**, 196403.
- 64 J. Zhang, G. Liang, C. Wang, C. Lin, J. Chen, Z. Zhang and X. S. Zhao, *ACS Appl. Mater. Interfaces*, 2020, **12**(25), 28313–28319.
- 65 O. Tillement, J. C. Couturier, J. Angenault and M. Quarton, *Solid State Ionics*, 1991, **48**, 249.
- 66 G. Bergerhoff, R. Hundt, R. Sievers and I. D. Brown, *J. Chem. Inf. Comput. Sci.*, 1983, **23**, 66.
- 67 P. A. Cox, *Transition Metal Oxides: An Introduction to Their Electronic Structure and Properties*, Oxford University Press, Oxford, UK, 2010.
- 68 J. Gopalakrishnan and K. K. Rangan, *Chem. Mater.*, 1992, **4**, 745.
- 69 A. Jain, S. P. Ong, G. Hautier, W. Chen, W. D. Richards, S. Dacek, S. Cholia, D. Gunter, D. Skinner, G. Ceder and K. A. Persson, *APL Mater.*, 2013, **1**, 011002.
- 70 A. K. Padhi, K. S. Nanjundaswamy, C. Masquelier and J. B. Goodenough, *J. Electrochem. Soc.*, 1997, **144**, 2581.
- 71 H. Wang, C. Chen, C. Qian, C. Liang and Z. Lin, *RSC Adv.*, 2017, **7**, 33273.
- 72 B. Manoun, A. El Jazouli, S. Krimi and A. Lachgar, *Powder Diffr.*, 2004, **19**, 162.
- 73 G. Kresse and J. Furthmüller, *Phys. Rev. B: Condens. Matter Phys.*, 1996, **54**, 11169.
- 74 G. Kresse and J. Furthmüller, *Comput. Mater. Sci.*, 1996, **6**, 15.
- 75 J. P. Perdew, K. Burke and M. Ernzerhof, *Phys. Rev. Lett.*, 1996, **77**, 3865.
- 76 M. Cococcioni and S. De Gironcoli, *Phys. Rev. B: Condens. Matter Mater. Phys.*, 2005, **71**, 035105.
- 77 S. Dudarev and G. Botton, *Phys. Rev. B: Condens. Matter Phys.*, 1998, **57**, 1505.
- 78 A. Jain, G. Hautier, C. J. Moore, S. Ping Ong, C. C. Fischer, T. Mueller, K. A. Persson and G. Ceder, *Comput. Mater. Sci.*, 2011, **50**, 2295.
- 79 L. Wang, T. Maxisch and G. Ceder, *Phys. Rev. B: Condens. Matter Mater. Phys.*, 2006, **73**, 195107.
- 80 J. D. Pack and H. J. Monkhorst, *Phys. Rev. B: Solid State*, 1977, **16**, 1748.
- 81 S. P. Ong, W. D. Richards, A. Jain, G. Hautier, M. Kocher, S. Cholia, D. Gunter, V. L. Chevrier, K. A. Persson and G. Ceder, *Comput. Mater. Sci.*, 2013, **68**, 314.
- 82 P. P. Ewald, *Ann. Phys.*, 1921, **369**, 253.